Estudio de la Influencia del Campo Geomagnético Terrestre Sobre el Fondo de Electrones Cósmicos

Memoria presentada por:

Marcos López Moya

como trabajo de Tercer Ciclo en Ciencias Físicas

y dirigida por:

Victoria Fonseca González

Dpto. Física Atómica, Molecular y Nuclear
Facultad de Ciencias Físicas
Universidad Complutense de Madrid
Septiembre de 2001

Contents

Introduction

Astronomical exploration is driven by curiosity and proceeds in two directions. Firstly, towards the most distant and weakest sources which require an ever-increasing sensitivity. Secondly, towards sources of electromagnetic radiation at all frequencies. Technical developments have so far allowed to observe the Universe from radio waves to γ-rays up to about 10 GeV and from about 300 GeV up to 100 TeV. A gap has remained between 10 and 300 GeV which we intend to investigate for first time with the MAGIC Telescope.

The MAGIC (Major Atmospheric Gamma Imaging Cherenkov) Telescope, currently under construction, has the main goal of covering this gap in the electromagnetic spectrum and to make high sensitivity measurements in the very high energy range from 10 GeV to 100 TeV. The first goal implies a challenging design for the IACT telescope, pushing the affordable technology in terms of mirror size, stability and low optical imperfections, and specially in the development of the camera. With this innovations MAGIC will have the best collection area that has been attempted so far.

Opening an unexplored band in the electromagnetic spectrum with the MAGIC Telescope promises to turn into a fascinating and rich era of discovery, touching fundamental problems in astrophysics, cosmology, and particle physics. As often in the history of astronomy, this may involve new types of sources. Besides, there are also many well-defined issues which can be addresed with the IACT technique. Of special interest are γ-ray pulsars, since only seven have been detected so far and all them by the EGRET instrument aboard the CGRO satellite. The MAGIC telescope with its low energy threshold and high sensitivity is the only IACT telescope under construction which will have, for the first time, the capability to observe the EGRET pulsars in the energy region of some GeV, where their spectra is expected to cut off. This will help to test pulsar models in detail.

In this work our goals are two. On one hand we will discuss the power of the MAGIC Telescope for the observation of γ-ray pulsars. For that we will obtain the observation times required for the detection of the EGRET pulsars. And on the other hand we are interested in knowing the effect of the cosmic electron background at the low energies (some tens of GeV) where MAGIC will operate for the pulsar observations. In this context we will study the influence that the Earth's magnetic field can play at these low energies with the hope that it can reduce the trigger background rate due to cosmic electrons.

To achieve our goals, we carry out Monte Carlo simulation of the performance of the MAGIC telescope at energies of some tens of GeV, that is, at the detection threshold of the telescope. The realization of Monte Carlo simulation involve the knowledge of the underlaying physics of the atmospheric showers produced when γ-rays coming from the cosmic source plunge into the Earth's atmosphere, and of the working of Cherenkov telescopes which detect the Cherenkov light emitted in these showers. To start with, we need to study in detail the performance of the MAGIC Telescope for both γ-rays and background events, obtaining the efective collection areas and expected rates for γs, protons and electrons. Once that we have all these parameters we evaluate the expected pulsar rates and then we calculate the required observation times. In addition, we study the skymap around the position of these pulsars with the aim of predicting the expected pulse profiles observed by MAGIC. Lately, we study a possible reduction on the electron background rate by the effect of the Earth's magnetic field.

This document is organized as follows. Chapter 1 outlines the actual state of the γ-ray Astronomy and the physics program to be explored with MAGIC, with special attention in Cherenkov telescopes and γ-ray pulsars. In chapter 2 the evolution of γ and hadron showers in the atmosphere and the emission of Cherenkov light are described. In chapter 3 the technical characteristics of the MAGIC Telescope are described briefly with some emphasis on the camera design. In chapter 4 we will carry out Monte Carlo simulation of the atmospheric showers and the telescope in order to evaluate the parameters that define the performance of the MAGIC Telescope. With these parameters we will obtain in chapter 5 the observation time required by MAGIC for the observation of the EGRET pulsars. Finally in chapter 6 we study how the Earth's magnetic field can affect the cosmic electron background rate for MAGIC.

Chapter 1

Gamma-Ray Astronomy and Pulsars

The cosmos and its evolution are studied using all radiations, in particular electromagnetic waves. The γ-ray astronomy is the study of the Universe in the extensive band of the electromagnetic spectrum corresponding to energies above some MeV. From an astrophysical point of view we could define this field as the study of the non-thermal Universe, since the high energies involved rule out the thermal origin of this radiation. As photons cannot be accelerated in a direct way, since they don't have electric charge, the observation of γ radiation implicates the presence in the source of some kind of mechanism for the acceleration of charge particles. For our understanding of the Universe we need to investigate the processes that generate and accelerate these energetic particles. The quest for the even today uncertain origin of the cosmic rays, discovered by Victor Hess in 1912, has in the γ astronomy its best tool.

The γ-ray astronomy is usually divided into three energetic ranges: high energy (HE) up to 10 GeV; very high energy (VHE) from 10 GeV to 100 TeV; and ultra-high energy (UHE) above 100 TeV. Below 10 GeV, observations are carried out by satellite detectors. Due to the steeply falling fluxes of γ-rays from cosmic sources with incresing energy and the limited surface area of the satellites, their sensitivity to energies above 10 GeV is finally limited by very low count statistics. Conversely, current ground-based detectors provide an effective collection area some orders of magnitude larger, but they only can operate at energies above ~ 300 GeV.

Observations at visible wavelengths have a history of centuries, whereas γ astronomy by satellites and ground-based telescopes are end-of-20th century newcomers. In the last decade the VHE γ astronomy has experimented a big development thanks to the Imaging Atmospheric Cherenkov Telescopes (IACTs). They are ground-based telescopes based on the detection of the secundary particles and Cherenkov photons of the atmospheric shower formed when γ-rays plung into the Earth's atmosphere. But still, compared to astronomy at other wavelengths, VHE γ-ray astronomy is at the starting point and it is believed that it will open a door to new fields, probably full of new physics.

The energy range 10-300 GeV in cosmic γ-rays has not yet been investigated due to the lack of detectors in this domain. The main motivations for covering this gap are:

- To overlap satellite and ground-based observation for making cross calibrations (for example for multi-wavelength observations).
- To catalog the unidentified γ-ray sources detected by EGRET.
- To perform studies on shell-type supernova remnants as it is claimed that γ-ray emission from them may still be observable in the 10-100 GeV domain. On top of that, pulsed γ-ray emission from pulsars is expected to extend at most up to 40 GeV.
- To search for γ-ray bursts in the new energy window.

The MAGIC Telescope will cover this gap in the electromagnetic spectrum, exploring the energy regime above 10 GeV where important astrophysics, cosmology, and particle physics questions can be addressed. It will do so with unprecedented sensitivity such that, precision measurements of already known sources and first detections of a large number of weak sources above 10 GeV can be expected. For achive that, MAGIC will push the affordable technology in terms of mirror size, stability and low optical imperfections.

1.1 Experimental techniques of Gamma-Ray Astronomy

Having no electric charge, γ-rays are no affected by magnetic fields and can therefore act as messengers of distant cosmic events, allowing straight extrapolation to the source. But these photons, as we are going to see below, are very difficult to detect, which has represented a serious handicap for the development of the γ-ray astronomy.

The techniques of γ-ray Astronomy are governed by three important facts.

- The Earth's atmosphere is opaque to high-energy photons. At sea level, the atmosphere is $1030\, g/cm^2$ thick, which corresponds to 28 radiation lengths. This implies that the probabity that a high-energy photon incident from the zenith will reach the ground level without interacting electromagnetically is only $\sim 3 \cdot 10^{-10}$. And even, at mountain altitudes this probability is also negligibly small. Thus only a detector placed above the Earth's atmosphere, in a balloon or a satellite, can detect directly primary cosmic rays.

- The fluxes of high-energy γ-rays from astrophysical sources are quite low and decrease rapidly with increasing energy. For example, Vela, the strongest γ-ray source in the sky, has a flux above 100 MeV of $1.3 \cdot 10^{-5}$ photons cm^{-2} s^{-1} and a diffential flux that falls as $E^{-1.89}$. This implies that satellites only could observe below a certain energy, due to their small areas. By example, a satellite with a area of $\sim 1000\, cm^2$ will detect about one photon/minute above 100 MeV from Vela, and only one photon every two hours above 10 GeV. Then, for doing γ-ray astronomy at VHE and UHE energies is necessary to use detectors placed on Earth with areas much larger than current satellites areas.

- A very important incovenient in high-energy γ-ray astronomy is that at high-energies the flux of cosmic rays is much larger than the γ-ray flux. These charged particles have been bent in the interstellar magnetic fields so that they form an essentially isotropic background. The cosmic-ray proton flux has been measured from 100 GeV to $\sim$ 400 TeV to be:
$$\frac{dN}{dE} = (9.2 \pm 2.4) \cdot 10^{-2} \quad \mathrm{E}^{-2.76}\mathrm{m}^{-2}\mathrm{s}^{-1}\mathrm{sr}^{-1}\mathrm{TeV}^{-1} \tag{1.1}$$
where E is expressed in units of TeV. This makes essential the development of rejection techniques of the large cosmic-ray background in high-energy γ-ray astronomy.

1.1.1 Satellite-based detectors

As we have seen, the only way to detect primary γ-rays is using detectors setting in satellites. These detectors are based on the techniques used in particle physics. When the photon come to the detector, it produces a electron-positron pair. The photon direction is determined with tracking detectors, and its energy is usually measured with total-absortion calorimeters. The lager background rejection is achieved surrounding the detector by a thin "shield" of a scentillator material working in autocoincidence with the rest of the detector, to assure that only neutral particles triggered the instrument. A good angular resolution is important for identifying point sources and for minimizing the effect of diffuse background, and a good energy resolution is needed to determine the energy spectrum of the source. An important parameter of a satellite-based detector is its efective area, defined as:
$$A_{eff}(E) = \frac{N}{\phi(E)T} \tag{1.2}$$
where $\phi(E)$ is the photon flux to what the detector is exposed in units of ph/m^{-2}s^{-1}, T is the observation time and N is the number of events recorded. At low energies, the effective area rises with increasing energy because the photon conversion probability rises. Also angular and energy resolution generally improve with increasing energy.

It was not until the launch of the OSO-3 satellite on 1963, that the γ-ray astronomy with satellites started to obtain the first results. This satellite detected emission of 100 MeV from the galactic plane, whose flux was aproximately the expected from the interaction of cosmic rays with the galaxy interstellar gas. During the 70's decade the field suffered a big advance with the launch of two satellites: the SAS-2 in 1972 and COS-B in 1975. The COS-B gamma detector covered a energy range between 70 MeV and 1 GeV, with an effective collection area around 50 cm^2 depending on the incident photon energy. Among the goals achieved by these satellites point up the realization of precise observations of the difuse flux coming from the galactic plane and the detection of pulsed γ radiation from the Vela and Crab pulsars. COS-B also elaborated a catalog of 25 discrete sources, and among them, the first extragalactic one, the AGN 3C 273.

The most sensitive γ-ray telescope to date is the EGRET (Energetic Gamma Ray Experimet Telescope) instrument aboard the Compton Gamma Ray Observatory (CGRO), which was launched on 1991 and was operative until June 2000. This instrument is similar to the earlier COS-B but much larger, with an effective area 25 times greater than the COS-B area. EGRET covered a energy range from 30 MeV up to 30 GeV, with a angular resolution from 5.5^0 for the lower energies, up to 0.4° for the threshold energy. EGRET has made a detailed map of the sky and observed several point sources (see Fig. 1.2). Among its highlights are: the detection of radiation coming from 7 pulsars and more than 50 AGN's (all them of blazar type[1]), and the discovery of a lot of unidentified sources, to which it has not been able to associate any known object at other wavelength.

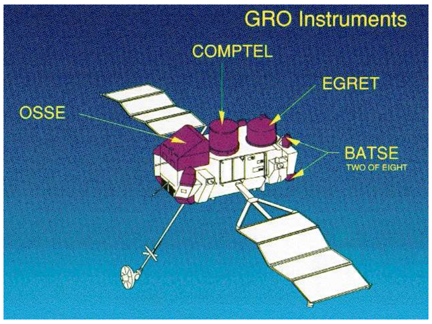

Figure 1.1: *The EGRET instrument aboard the CGRO satellite.*

Up to date the space γ astronomy has been restricted to energies below 30 GeV, because of the problems of the low photon flux at high energies, and the small satellite areas. Several space detectors have been planned to overcome these limitations. Among then are: the AMS detector that will be set in the Internacional Space Station, which will cover an energy range between 300 MeV to 300 GeV with a sensitivity similar to EGRET. In the range of lower γ-rays, ESA plans to launch on 2002 the INTEGRAL satellite, which will work betwen 15 KeV and 10 MeV. Finally, around 2005 will be launched the GLAST satellite, which sensitivity for point sources will be from 50 to 100 times better than the EGRET one, covering an energy range from 10 MeV up to 200 GeV.

[1]As we will see in §1.4.1, blazars are galaxies with mainly non-thermical emission, and which seem to have jets pointing to us.

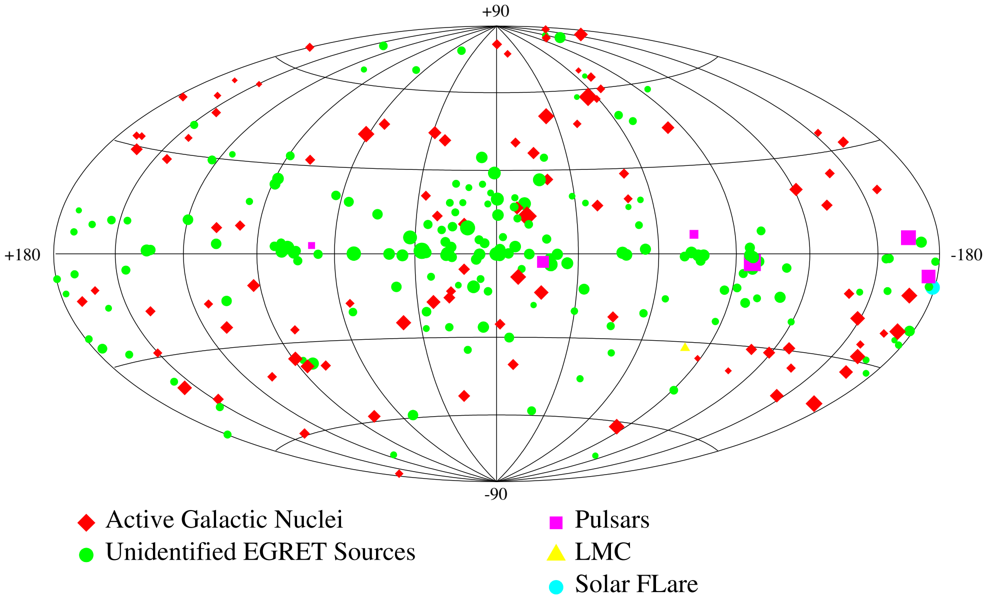

Figure 1.2: *The third EGRET catalog* $(E > 100 MeV)$

1.1.2 Earth-based detectors

At energies above 200 GeV, observations are conducted with ground-based γ-ray telescopes. Although high-energy γ photons get absorbed in the atmosphere, they can be observed indirectly. γ-rays coming to the Earth from outer space interact with air molecules high in the atmotphere, giving rise to a shower of secundary particles called *Extensive Air Showers* or EAS. Earth-based γ-ray astronomy detect the product of these interactions.

The main limitation of these class of detectors is the rejection of the high cosmic rays background of showers initiated by charged cosmics rays. But on the other hand, they have the advantage of their big effective collection areas due to the big extension of an EAS. In addition, their energy thresholds are very high, because low energy photons produce showers which extinguish before they reach the ground. This last can be overcome installing the detectors on mountain tops and by using the Cherenkov light emitted by the shower, although this method is affected by the night sky background. We will see in chapter 3 how EAS develop in the atmosphere and how the emission of Cherenkov light is produced.

An extensive air shower can be detected by observing either the shower of particles which reach the ground (as in the *extensive air-shower particles detector arrays*) or the Cherenkov radiation produced in the shower (as it is done in the *air Cherenkov detectors*). In both cases one uses the propierties of the EAS to infer information about the primary particle that initiated it, like its energy and direction. There are different types of ground-based detectors, but among them point out the Chrerenkov telescopes which will be studied in the next section.

1.2 Cherenkov Telescopes

The Cherenkov radiation generated in EAS is an important source of information that can be easily exploited with the appropriate experimental device. The Cherenkov method uses the fact that, the charged secondary particles of a atmospheric shower radiate low-energy (visible to ultraviolet) photons at a characteristic angle, the Cherenkov radiation. These Cherenkov photons travel through the atmosphere and can be observed on the Earth surface by sufficiently sensitive instruments. These detectors are simple, inexpensive and well-understood. So, by observing the Cherenkov light from EAS induced by γ-rays, it is possible to detect discrete γ-rays sources with great sensitivity.

A Cherenkov telescope (CT) consists of a parabolic reflector and a camera placed on its focal plane. Usually, for economic reasons, the reflector surface is a tessellated mirror made out of smaller mirrors. And typically they are glass mirrors with a quartz coating on the polished surface. The gross mirror profile follows a parabola for minimal time spread while individual mirrors elements are spherical with a radius that gives the best image quality. The reflector of an imaging telescope must provide an optical resolution of better than $0.1°$ - $0.2°$ within a field of view of $2°$ - $3°$ in diameter[2]. The camera is the most important element of the telescope and is decisive for the improvement of a good γ sensitivity.

The camera is made out of photomultipliers tubes and is accompanied by fast signal processing electronics. The number of pixels in a camera and in particular the angular size of each pixel is very important because it determines the minimum angular resolution that the telescope can achieve. Through the years cameras have develop from a single photomultiplier, usually called pixel, to a few hundreds in the "second generation" of CTs, the named *Imaging Atmospheric Cherenkov Telescopes* (IACTs). In this way, a crude image of the Cerenkov light pool is recorded. These images are very useful, because as we will see, in base of them, it has been development a very efficient technique to reject the large comic-rays background, named the Atmospheric Cherenkov Imaging Technique.

In Fig. 1.2 we can see a Cherenkov telescope. The Cerenkov light is reflected on the mirrors and then detected in the focal plane by one or many photomultipliers which convert the optical signal into an electronic signal. Once the light has been detected in a phototube, fast electronics are used to record the γ-ray event. The Cherenkov light produced in an EAS is very faint and can only be detected cleanly on dark, moonless nights. Even so, it helps that the total pool passes through the detector in only a few nanoseconds. This allows further separation of the faint signal from the ambient night sky.

Although externally the Cherenkov and optical telescopes are similar, the

[2] This is the characteristic difference in size between the images of γs- and hadrons-initiated showers


Figure 1.3: *The pictures show one of the HEGRA telescopes (right), and its camera (left) made out of 271 PMTs. The 30 glass mirrors focus the Cherenkov light on a camera in about 5 m distance. Each of the individual mirrors has a reflectivity* $> 84\%$ *at wavelenghts between 300 and 600 nm and angular resolution of 20"-40".The light collecting surface in front of the camera can be seen, specifically developed to ensure optimal entrance angles for all incoming photons (so-called Winston cones).*

recording of images in a Cherenkov telescope has quite different constraints from what optical telescopes require. On the one hand, the phenomenon to be studied, the electromagnetic shower, is comparatively large, which requires a large field of view. Therefore the extraordinary resolution of CCDs is not required. Instead, high sensitivity to single photons and the best possible time resolution are important, because the signal is weak and marginally detectable, and the discrimination against showers induced by cosmic-rays is helped by determining precise arrival times. Therefore, highest-quality photomultipliers have to be used. On the other hand, the mirrors used can be of reduced quality as compared to optical telescopes since they are reflecting the light of this large local pool rather than directly imaging an astronomical source.

The first experiments developed for the detection of Cherenkov radiation were carried out in the early 50's by a group of the British Atomic Energy Research Establishment in Harwell. The idea was very simple, since each shower produces a vast spray of electrons over a very short time, then Cherenkov light might accompany each shower. This lead them to construct a very simple device, a garbage can with a 30 cm parabolic mirror inside and a photomultiplier tube placed on its focal plane. On the very first night this assembly provided rewards; large pulses were detected at a rate of about one every two minutes. Here was a promising ground-based technique for searching for point γ-rays sources. And around thirty years ago, in 1968, the first Cherenkov telescope was built, the Whipple telescope placed in Arizona, that with a diameter of 10 meters, has been so far the bigger Cherenkov telescope. Since then, the Cherenkov technique has being improving steadily.

Telescope	Location (Alt. in m)	Mirror diameter (m)	Number of pixels	Pixel size (^{o})	Field of view (^{o})	Energy threshold (GeV)
Whipple	Mt. Hopkins, Arizona (2300)	10	151	0.25	3	250
CAT-imager	Thémis, France (1650)	5	546+54	0.12	3	250
HEGRA-CT system	La Palma, Spain (2220)	5	271	0.25	3.25	500
HEGRA-CT1	La Palma, Spain (2200)	5	271	0.25	3	700
CANGAROO	Woomera, Australia (0)	3.8	256	0.18	3	1000

Table 1.1: *Some Cherenkov Telescopes working currently.*

In the past decade, ground-based γ-ray astronomy has become a viable discipline and an important complement to observations from orbiting γ-ray telescopes. Today, the Imaging Atmospheric Cherenkov Telescopes (IACTs) have become the most sensitive technique for the observation of TeV γ-rays. This is due to the large effective collection area, which is about 10000 times that of current satellite experiments, and to the development of the atmospheric Cherenkov imaging technique, which has led to significant advances in γ-ray detection sensitivity in the energy range from 200 GeV to 50 TeV. The technique is also sensitive for time-variation (burst and pulsar) searches.

Nowdyays, there are more than ten "second-generation" ground-based γ-ray observatories in operation or under construction. In table 1.1 some characteristic parameters of some Cherenkov telescopes existing at the moment are summarized. There is one collaboration active in the United States and there are major groups in Germany, Spain, France, the U.K., the former U.S.S.R., India, Japan, South Africa, and Australia. The HEGRA IACT system, in which participates the *Grupo de Altas Energias* of the *Universidad Complutense de Madrid*, is unique in terms of the stereoscopic technique used. It is formed by 5 IACT telescopes separated by a distance between 50 and 100 m. The technique of observing atmospheric showers (initiated by cosmic rays or γ-rays traversing the atmosphere) simultanously with several telescopes yields an improved resolution of the angular and spectral reconstruction of the primary particle. Based on the extraordinary background suppression available due to the stereoscopic technique, a sensitivity to very weak γ-ray sources (at the level of few percent of the Crab Nebula flux) as well as the ability of limited sky surveys is obtained.

The first source in the VHE regime were detected by the Whipple Observatory in 1989: the Crab Nebula, which has been established as the standard candle for ground-based γ-ray astronomy. Presently, there are now at least five well-established TeV γ-ray sources. The three pulsar/plerions: Crab, PSR 1706-44 and Vela and the two highly variable AGNs Markarian 421 and Markarian 501. And there are evidences of other four posible sources: SN 1006, RJX1713.7-3946, Cas-A and the blazar 1ES 2344+514.

Given that this technique is just at the edge of becoming a so-called well established technique, the small number of 5 to 10 TeV γ-ray sources detected so far is no surprise. Ground-based telescopes improve continuously in small increments: there is no technical barrier to further increases in both flux sensitivity and reduced energy threshold. In principle, a telescope can be built with an energy threshold as low as 10 GeV. A new generation of telescopes with improved sensitivity has the promise of interesting measurements of fundamental phenomena in physics and astrophysics. HESS is one such next generation system. It is an array of large atmospheric Cherenkov telescopes planned for a site in Namibia. In addition, the Milagro instrument is coming on-line. It is an underwater Cherenkov telescope that has the distinct feature of a large field-of-view in the TeV range. But among the future projects point out the MAGIC Telescope.

The MAGIC telescope project is a continuation of the work that has been started before 1987 with the HEGRA detectors, both experiments targeting the observation of highly energetic photons from sources within and outside our galaxy. The aim of the MAGIC Telescope is to exploit all presently avaliable technologies in order to obtain a Cherenkov telescope with an energy threshold close to 10 GeV, a sensitivity orders of magnitude larger ($> 10^3$) compared with EGRET sensitivity in the overlapping energy range and, last but not least, to have it ready in January next year; which signifies that MAGIC will be the only detector around the world capable of measuring in the above mentionated energy domain. For reach a so low energy threshold MAGIC will have a parabolic mirror of 17 m diameter an a camera formed by 577 high efficiency photodetectors, and it will innovates in several key aspects as the active mirror control. In chapter 3 we will describe the innovative techonological developments allowing the MAGIC Telescope to reach such a low energy threshold and high sensitivity.

1.2.1 The Problem of the Background in the Cherenkov Telescopes

Cherenkov telescopes have the advantage of their big effective collection areas ($> 40000\ m^2$ compared with $< 1\ m^2$ of the satellites). However they have to deal against two serious problems: the light of the night sky and the large isotropic background from showers initiated by cosmic rays.

The Light of the Night Sky

The light of the night-sky background (also named LONS) is the diffuse integrated light arriving at the detector from the night sky, over the typical time measurement gate of the arrival of an EAS. The LONS has several components and depends on an specific place and a given detector, as well as the zenith angle. It sums up the light coming from several sources: the air fluorescence, the starlight of faint stars (m$\geq$ 10), the light due to the air glow, and also eventually, man-made artificial light. The LONS has a very importante role in Cherenkov telescopes. For example, in full moon nights measurementes become unable. In addition, the light of the night sky background is one of the most important factors in limiting energy threshold of atmospheric Cherenkov telescopes. In fact, the amplitude fluctuations of detected LONS determine the threshold of a detector[3].

In terms of the LONS fluctuations we can define the energy threshold as the shower energy which provides a minimum given signal/noise ratio during the given measuring time. Therefore, the energy threshold will depend on the LONS flux Φ, the mirror surface area A, the solid angle Ω on the sky viewed by the mirrors, the camera integration time τ (which must be fit to the typical duration of a Cherenkov pulse) and the light collection efficiency LCE of the photons:

$$E_{thr} \propto \sqrt{\frac{\Phi\,\Omega\,\tau}{A \cdot LCE}} \tag{1.3}$$

This is due to the fact that, at a given primary energy, the Cherenkov signal S is almost proportional to the mirror area A, while the LONS fluctuations are $\propto \sqrt{A\Phi\tau\Omega}$, and therefore, for a simple telescope: $S/\sqrt{B} \propto \sqrt{A/\Phi\tau\Omega}$. Thus, the effect of the night sky background can be reduced by incresing the mirror area, decresing the integration time (to the limit of the cherenkov pulse length), and decreasing the acceptance solid angle.

For reducing the night-sky background rate, Cherenkov telescopes implement a trigger logic, requiring a fast coincidence (within 3-10 ns) of at least several pixel over threshold.

The Cosmic-ray Background Rejection: The Imaging Technique

The rejection of cosmic-ray background is the main difficulty of the γ-ray Astronomy based on Earth, since more than 99% of the atmospheric air showers are caused by the isotropic flux of hadronic cosmic rays. To overcome this problen is needed an efficient technique for recognizing and rejecting the hadronic showers, in order to accept only those showers started by a γ-ray. On the using of Cherenkov Telescopes, a very efficient technique for the cosmic background rejection was

[3]The threshold of a cherenkov telescope is determined by the number of photons needed to observe a signal above the level of the night-sky background.

developed in 1977 at the Whipple Observatory. This technique recieve the name of *Atmospheric Cherenkov Imaging Technique* (AICT) or just *imaging technique.* As its name states, the imaging technique consists on obtaining an image of the atmospheric shower an then to exploit the geometrical differences that exist between the images formed on the camera by γ-ray and hadronic-initiated showers. In the imaging technique, we understand by images the geometrical projections of the showers on the camera, and not images of the source. In IACT telescope the light comming from different heights is focus for the reflector in different points of the focal plane, obtaining on the camera a projection or "image", nearly elliptical in shape, of the longitudinal and lateral development of the shower.

The differences on the images left on the camera by both kind of showers are differences in the orientation and shape of the images. Related to the orientation, this is the result of a geometrical effect. If the telescope is pointing to a γ source, the axis of showers initiated by γ-rays coming from the source will be parallel to the optic axis, and then the images will be point to the source position (the center of the camera) through the effect of perspective. Conversely, hadronic showers arrive isotropically distributed within the field of view of the camera, with random shower axis orientation relative to the optic axis of the telescope. Regarding with the shape, the differences arise for physical reasons. As we will see in next chapter, γ-ray initiated showers start higher up in the atmosphere and spread out less than hadronic showers, due to the smaller transverse momentum in electromagnetic interactions compared with hadronic interactions. These two effects produce that the images formed by γ-rays are characterized by narrow and compact images and tends to have an ellipsoidal shape which aligns itself with the direction of the incoming photon. Conversely, cosmic-ray induced air showers produce Cherenkov light images which are much broader and diffuse and less well aligned with the arrival direction.

The way in which the differences in the images are exploited in the imaging tecnique is by means of a suitable parametrization of the shower images. The parameters that are usually used are the Hillas parameters [1], which are based on a second moments analysis of the recorded pixel signal amplitudes. (The Hillas paramters are discuss in Appendix A). Once that the images have ben recorded by the camera, by selecting only those events which are γ-ray-like in appearance (by means of using suitable discrimination algorithms based on Monte Carlo simulations), nearly all the cosmic ray contamination can be removed and fairly clean γ signals can be obtained, resulting in a much improved ability to detect an excess number of counts from the source direction.

Next, we address the major physics targets of the γ-ray Astronomy, and specifilly of the MAGIC Telescope, emphasizing the importance of achieving a very low γ-ray energy threshold. Firstly, we will discuss about γ-ray pulsars, of main importance for our work, and then we will study other sources of γ-rays.

1.3 Pulsars

Pulsars are strongly magnetized and very fast rotating neutron stars, with periods from about 1.6 ms to some seconds. Intense radiation is beamed along the magnetic poles, and as the magnetic axis is not aligned with the rotation axis, the emitted beam sweeps lighthouse-like through the sky, causing the observation of a periodic signal if the beam passes across the earth.

Pulsars provide astrophysical laboratories for exploring the extremes of physical conditions. These objects provide the strongest gravity, the largest magnetic fields (of the order of 10^{12} G), and some of the highest energy particle accelerators in the observable universe. Pulsars are formed in supernova explosions (such as the one that formed the Crab Nebula, shown in Fig. 1.11) after the collapse of a massive star ($M \geq 8M_{\odot}$) or from a accreting white dwarf in a binary system. During the evolution of a massive star (see Fig. 1.4), its core becomes increasingly massive, and at some point the core surpass the Chandrasekhar mass limit of 1.4 M$\odot$, moment in what degenerate electron pressure can no longer support the core, and then it collapse from a size of about 8.000 Km to one of about 20 Km. The presure at the center grows large enough that the electrons fuse with the protons in the iron nuclei, via β-decay process $e^{-} + p \rightarrow n + \nu^{-}$. The star's collapse continues until the neutrons become degenerate and the contraction is halted by repulsive forces between neutrons. In this process an enormous amount of neutrinos is produced which leave the core carrying an enormous amount of energy of the order of 10^{46} W (equivalent to the energy produced by 100 stars like the Sun during their entire lifetimes). The pressure of these released neutrinos produces that the outer layers of the star collapsing inward rebound off the neutron core. Thus, the collapse reverses and a rapidly traveling shock wave is sent outwards, which explodingly dispersed the remaining stellar envelope within seconds, producing a supernova explosion. The aftermath of a supernova is an

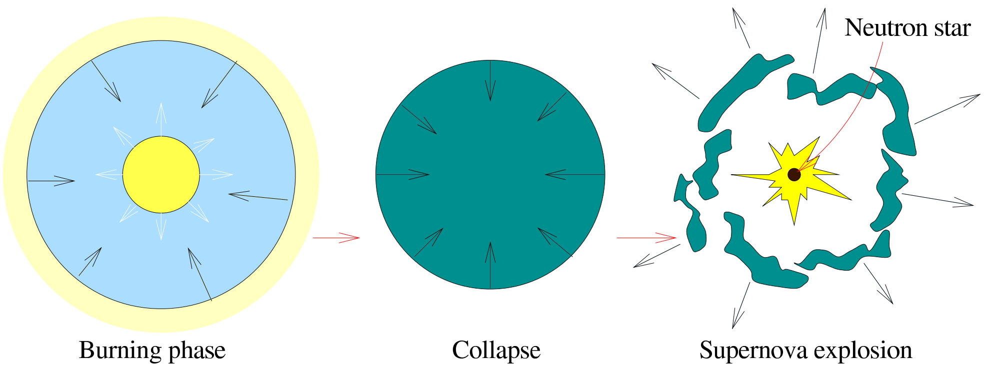

Figure 1.4: *Formation of a pulsar. After a stable equilibrium during the burning phase, the star collapses. If its mass is large enough, a supernova explosion occurs, possibly leaving the stars core as a rotating neutron star.*

expanding shell of cooling ejecta surrounding a very compact remnant. After the supernova explosion the core of the star, which consists nearly exclusively of neutron, can remains. A pulsar is thus a collapsed, ultracompact star supported only by neutron degeneracy pressure. Near the edge of this stellar remnant the pressure is not high enough to cause the nuclei to disolve, and a rigid crystalline crust of nuclei remains once the surface temperature drops sufficiently. The mass of a pulsar is about 1.4 solar masses, and it radius is typically of 10 Km, what yields to extreme densities. Between the outer crust and the centre, the density covers about a range of nine orders of magnitude, from 10^6 g/cm^3 to 10^{15} g/cm^3.

While more than 1000 radio pulsars are known, only seven pulsars have been so far detected in the γ-ray range by EGRET [2]. Inspecting the seven EGRET pulsars (see Fig. 1.5), the main impresion is that they all differ from each other in various respects. No two show the same miltiwavelength behaviour and the pulse profiles in the GeV region are also different. Different models have been proposed to explain the mechanisms of production of γ-rays in pulsars. They make different assumptions about the location of particle acceleration, and therefore make distinct predictions for the shape of the pulse profile and on the sample of radio pulsars that will be seen in γ-rays.

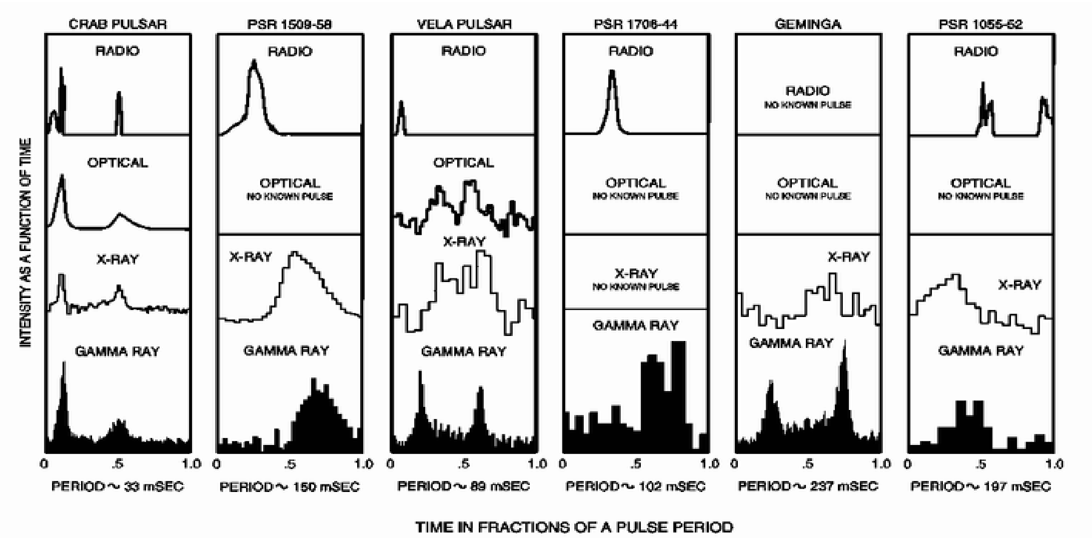

Figure 1.5: *Mutiwavelength live curves of the seven pulsars detected by EGRET. A flat line in radio, optical or X-ray means that no such pulsation has been detected.*

There are currently two popular classes of models to explain the mechanism of production of high-energy γ-rays in pulsars. In both of them the pulsed emission originates from radiation by charged particles accelerated in differents regions of the pulsar magnetopshere. In the *Polar Cap* model [3, 4] charged particles are accelerated along the magnetic field lines by the gaps formed just above the magnetic poles. And in the *Outer Gap* model [5, 6] γ-rays are produced as the result of the aceleration of charged particles in vacuum gaps formed in the outer regios of the pulsar magnetosphere. The starting point of both models is the model proposed by Goldreich & Julian in 1969 [7], which describes the basic physics of a neutron star magnetosphere. According with it, the huge rotating magnetic field of the neutron star induces an electric field, strong enough to pull particles out from the star's surface. This causes that the space sourronding the neutron star get filled with a charged separated plasma, creating a magnetosphere which co-rotates which the star. The co-rotation implicates that the plasma particles must be confined inside a cylinder of radius $R_L \equiv c/\Omega$, called "*light cylinder*", since past this radius particles would co-rotate at a speed greater than the speed of light. The light cylinder divides the magnetic field lines into two types: "closed" field lines, which close within the light cylinder, and "open" field lines which pass through the light cylinder. The regions on the stellar surface from which the open field emerge lines define the *polar caps*[4]. In Fig. 1.6 the basic structure of a pulsar magnetosphere is shown.

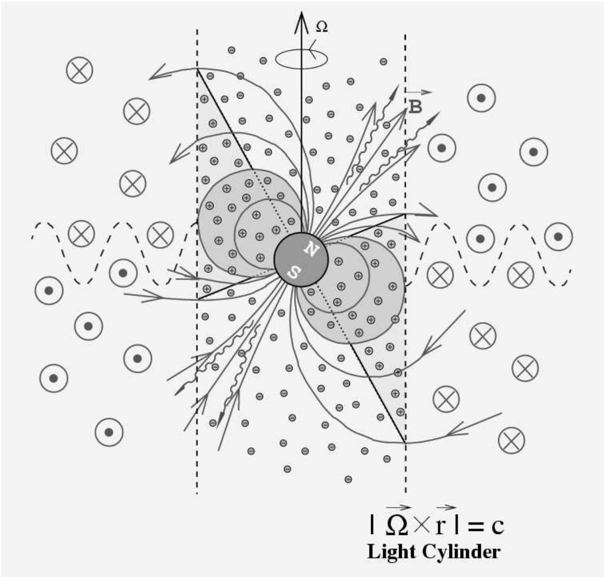

Figure 1.6: *Schematic representation of a pulsar magnetosphere. The magnetic field line which touch the light cylinder define the edge of the polar cap regions. Radiation escapes along the open field lines outside of the shaded regions.*

- **Polar Cap Model.** In the polar cap model the γ emission from the pulsar comes from its polar caps according to the following mechanism. The huge induced electric field pull charged particles out from the stellar surface and accelerate them along the strong magnetic field lines, radiating *curvature*

[4]As an example, for the Crab pulsar the size of the polar cap is $\simeq 4.6°$.

or *synchroton* radiation in their instantaneous direction of motion[5]. Since the charged particles are so energetic, the radiation may be in the GeV to TeV energy range (γ rays). As these γ photons move through the strong magnetic field of the pulsar, they tend to interact with the background field producing electron-positron pairs via $\gamma + B \to e^+ + e^-$. These pairs are born at a non-zero pitch angle with respect to field lines, so they emit synchrotron radiation. These synchrotron photons can also be γ-rays, so they can generate more pairs which create more photons, and so on. This result in a cascade of pair production which terminate when the photons have lost enough energy that they can no longer produce pairs. As the magnetic poles and field lines rotate with the star, the accederated charged particles radiate in a sweeeping beam, and is seen as a a train of pulses if the beam happens to sweep across our line of sight during the star's rotation, in the same manner as does light from a lighthouse.

- **Outer Gap Model.** Apart from the widely favoured polar cap, a number of alternative regions in the magnetosphere have been proposed for the origin of the pulsar emission, but mainly for the high energy radiation. Among these, the presently most favoured one is the outer gap emission. Cheng, Ho and Ruderman [5, 6] proposed a mechanism for producing the observed emission from the Crab and Vela pulsars in γ-ray to optical wavelengths, in which high-energy pulsar emission is generated in vacuum gaps existing in the outer regions of the magnetosphere. This gap is formed between the $\vec{\Omega} \cdot \vec{B} = 0$ surface (which defines the charge-separated regions) and the light cylinder, along the last closed field line (see Figure 1.7). In this model there are three important regions which contribute to the emission mechanism in a bootstrap manner. Inside the gap (region I of Fig. 1.7), $\vec{E} \cdot \vec{B} \neq 0$, and electrons and positrons are accelerated along the curved magnetic field lines by the large potential difference across the gap, radiating curvature γ-rays and/or boosting soft photons via inverse Compton scattering. Unlike the case in polar cap models, the magnetic fields in the outer gap are too weak for one-photon pair production to play a significant role in the cascade. Instead, the these primary γ-rays move away from the closed-field-line region and collide with ambient photons[6] to produce secondary $e^{\pm}$ pairs in region II, just above the vacuum gap boundary[7], via $\gamma + \gamma \to e^+e^-$. These secondary electrons and positrons will typically have a substantial component of their momenta perpendicular to the local magnetic field and will emit synchrotron radiation (and/or boost photons by inverse Compton scatter-

[5] Curvature radiation dominates the synchrotron radiation if the Lorentz's factor γ is $\gamma > 10^6$. Otherwise synchroton radiation dominates.

[6] This ambient photons can be thermal X-rays from the polar caps (as in the case of Vela or Geminga) or non-thermal X-rays produced by the cascade (as in the Crab).

[7] Where these pairs are created will, in fact, define the gap boundary.

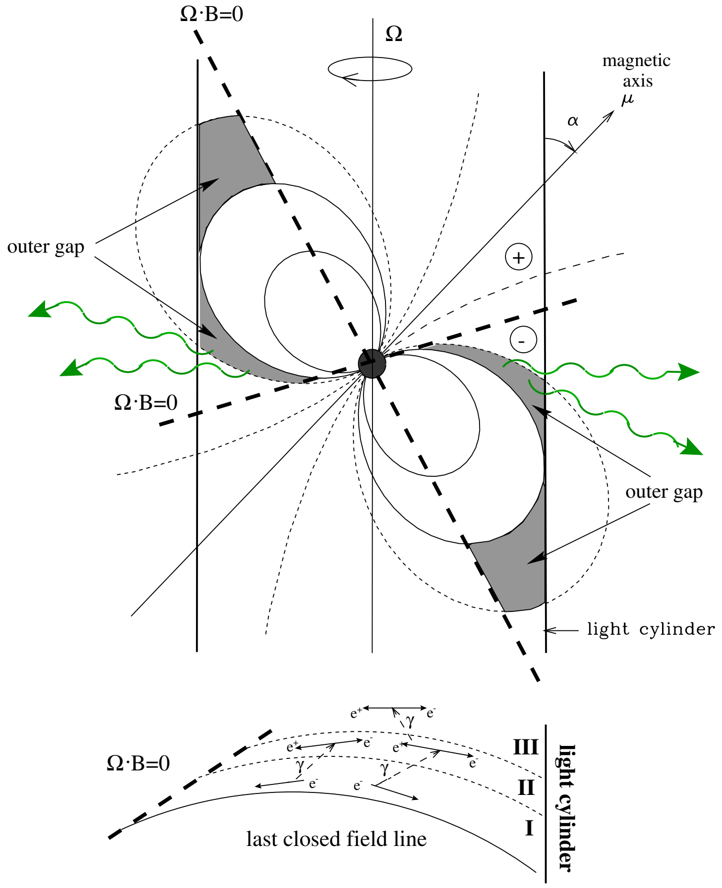

Figure 1.7: *Pulsar magnetosphere according to the outer gap model. The four outer gaps, drawn in bold, form along the last closed field lines between the null surface defined by* $\rho_c \propto \Omega \cdot B = 0$ *(indicated by dashed lines), and the light cylinder. Beams from one hemisphere are mirrored in the opposite hemisphere.*

ing), covering energies from optical to γ-rays. The secondary photons move beyond region II to form tertiary pairs in region III. These pairs have insufficient energy for formation of X-ray or γ-rays, but provide a sea of infrared and optical photons which illuminate the entire open magnetosphere, refuelling the gap so that the mechanism in region I can continue. Also, since some of the secondary radiation will be directed into the primary acceleration region, those photons can also be inverse-Compton scattered by the primary particles and be promoted to "primary radiation". In this manner, the radiative processes in the primary region are bootstrapped by the radiation produced in the secondary regions. One immediate consequence of this model is that γ-rays produced in the outer magnetosphere will not be as severely attenuated by the magnetic field as γ-rays produced near the polar cap surface.

In both pulsar models it is predicted a cutoff in the γ-ray pulsed emisison, above which not γ rays are emitted from the pulsar. The most recent theoretical model calculations [8] suggest that pulsed emission from isolated pulsars is not to be expected beyond 6-50 GeV if the γ-radiation originates in the vicinity of the pulsars polar region (polar cap model), but may extend to 100 GeV if the γ-radiation is produced according to the outer gap model. In polar cap models, the high energy spectrum is cut off by the magnetic pair production above an energy that is dependent on the local magnetic field strength. While most young pulsars with surface fields in the range $B = 10^{12} - 10^{13}$ G are expected to have high energy cutoffs around several GeV, the γ-ray spectra of old pulsars having lower surface fields may extends to 50 GeV. Although the γ-ray emission of older pulsars is weaker, detecting pulsed emission at high energies from nearby sources would be an important confirmation of polar cap models. Outer gap models predict more gradual high-energy turnovers, but also predict an inverse Compton component extending to TeV energies. Detection of pulsed TeV emission, which would not survive attenuation at the polar-caps, is thus an important test of outer gap models.

Due to the presence of the cutoff in the pulsar spectra, current ground-based telescopes are not able to observe them, since the pulsar γ emission disappears below the energy thereshold of current IACTs ($\sim$ 300 GeV). So, for carrying out pulsar studies with ground-based detectors it is firstly neccesary to push the energy threshold of the telescope as low as possible, at least to the 10-30 GeV region. In addition, as we have seen, the pulsar cutoff predicted by the models happens in the unexplored region of the γ-ray astronomy. Thereby, it hasn't been possible so far to find out which of the pulsar models really takes place in γ-ray pulsars, since the large models uncertainties make it absolutely necessary to measure with high statistics in the 5 GeV to 100 GeV energy domain, in order to gain further insights into the mechanism for high energy γ-ray production in pulsar systems. Therefore, a new generation of γ-ray telescopes sensitive to GeV-TeV emission are needed, which will provide critical tests of pulsar acceleration and emission mechanisms.

The MAGIC telescope with its big mirror area and high sensitivity is the only IACT telescope under construction which will have for first time the capability to detect the known seven EGRET γ-ray pulsars and test the pulsar models in detail. In addition, due to its very high sensitivity, the MAGIC Telescope will not only be an unique instrument for the study of the known γ-ray pulsars, but it will probably be able to discover several additional radio-pulsars at GeV energies, on time scales as short as few hours. In this context, only one radio-quiet pulsar has so far been detected at high energies: the Geminga pulsar. Assuming, that the Gemimga is the closest object of its type, one can estimate the number of such objects in our galaxy to be $\simeq 1600$ [9]. By its high sensitivity, the MAGIC Telescope will be able to look for fainter Geminga-like objects which could not be detected by EGRET. Candidates for Geminga-like pulsars are also the faint unidentified EGRET-sources which have in the EGRET-data too low signal-to-noise for periodicity analysis. Furthermore, many of the brightest unidentified EGRET sources are coincident with high-mass stars or supernove remnants and are also likely to be associated with pulsars. Thus pulsars could be a dominant constituent of the Galactic γ-ray sources. The huge mirror area also could make the MAGIC Telescope an optical telescope with a very large aperture. The optical emission of the observed pulsar could therefore (according to our calculations) be monitored by measuring the light intensity variation of teh central camera pixel with high precision. This will offer the possibility to correlate a possible γ-flux modelation with the pulsar's optical period and phase. We note that the Whipple collaboration has recently succeeded to measure the optical period of the Crab pulsar with their Cherenkov telescope.

With the help of the MAGIC Telescope, we expect that in the coming decade, this unexplored region above 10 GeV may hold the key to a question on which theorists have disagreed for at least two decades, that of how and where high energy emission emerges from the pulsar and how it relates to the radio emission.

1.4 Other Sources of VHE γ-rays

1.4.1 Active Galactic Nuclei

Recent results indicate that about 1% of all galaxies (including our own milky way) have an active center, in which a supermassive black hole is building up. Whereas for "normal" galaxies we can think of the total energy they emit as the sum of the emission from each of the stars found in the galaxy, for the "active" galaxies, this is not true. There is a great deal more emitted energy than there should be, coming from the center of the galaxy. Active galaxy nuclei (AGNs) are those galaxies whose radiation are mainly produced in their nuclei. They are defined by the presence of highly luminious and variable, non-thermal emission from the galaxy's core.

The problem encountered in the study of active galaxies has been the diversity of observational features that they present, both optical and radio, what has given rised to the proliferation of a lot of classes and subclasses of AGNs: Seyfert galaxies (types I and II), quasi-stellar radio objects (quasars), radio galaxies, blazars, BL Lacertae objects (BL Lac objects), etc. But the principal division is between radio-loud and radio-quiet AGNs, depending on the relative intensity of their radio emission[8]. Fortunaly, in the last two decades a unified theory has emerged that enjoys wide acceptance. We shall briefly study this unified model of AGN and, mainly those propierties that are relevant to VHE γ-ray astronomy.

[8]It has been also suggested a correlation between the radio emission and the galaxy shape: the radio-loud AGSs are usually asociated with elliptical galaxies and the radio-quiet with spiral galaxies.

In the unified AGN model, the central engine of the AGN contains a supermassive black hole $M \sim 10^7 - 10^{10} M_\odot$, powered by accretion. This is a very efficent process which may convert 10% of the rest mass of acreted matter into radiation, explaining the big amount of enegy releases in very small regions (the Schwarzschild radius of a $10^{10} M_\odot$ black hole is 0.001 pc). Figure 1.4.1 illustrated this model. There is a thin acretion disk rotating around the black hole, and this disk, in turn, is surrounded by a thick torus lying in the equatorial plane of the black hole. Inside the torus, there are clouds orbiting around the black hole, which are responsible for the observed emission lines. The broad emission lines are emitted by the clouds moving close to the black hole at high velocities ($\geq 10^4$ Km/s) by the Doppler broadening, and the more distant clouds, moving slower, are the resposible for the emission of the narrow lines. In addition, radio-loud AGNs have well-colimated jets perpendicular to the accretion disk, which can extend hundreds of Kpc.

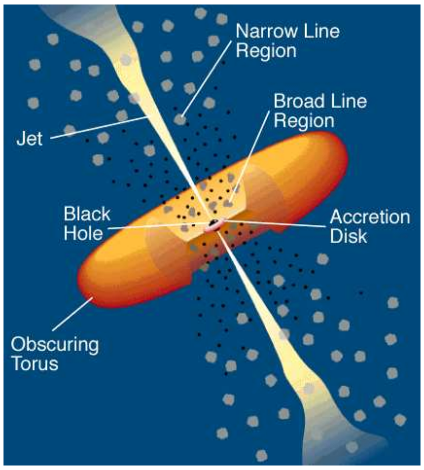

Figure 1.8: *Artist conception of the model of a radio-loud AGN.*

Active galaxies emit radiation over the entire electromagnetic spectrum, from radio waves to TeV γ-rays. In the unified model, differents parts of the nucleus are responsible of the continous emission at the differents wavelengths. The thermal emission (from infrared to x rays) emanates from the torus and accretion disk. And the non-thermal emission (radio and γ-rays) comes from the jets.

Starting with this model, is possible to understand most of the different AGN types as consequences of different viewing angles with respect to the rotation axis and of the presence or absence of jets. There are two effects of the viewing angle on the observations: simple shadowing effects of the torus (since at large viewing angles the torus obscures certain emission regions from view), and the Doppler boosting of a relativistic jet viewed at small angles[9] These consideration lead to relationships between viewing angle with respect to the jet direction and observed properties of radio-loud and radio-quite AGNs, as summarized in Fig. 1.9.

In radio-loud AGN viewed at large angle, the torus obscures the clouds that are close to the black hole. Only the distant clouds (which are moving slowly) are unobscured, so narrow emission lines are observed. The Doppler factor is small, so no TeV emission is observed. At smaller angles, the Doppler factor becomes large and TeV emission is observed. The time scale of the variability of

[9] This allows high energy photons to escape from regions with high radiation fields, producing an increase in the apparent luminosity of the source in the direction of the jet.

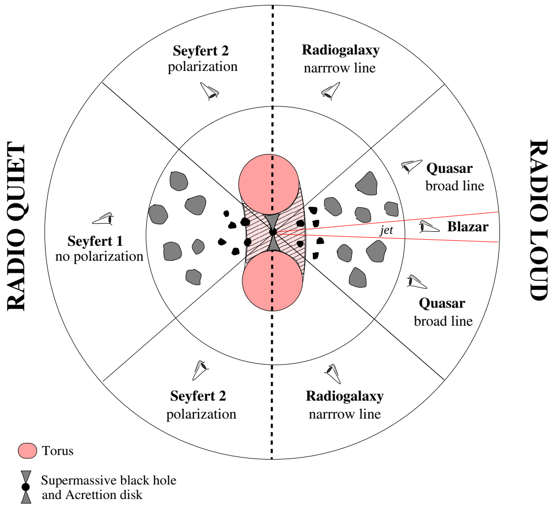

Figure 1.9: *Schematic diagram of the unified model of AGNs. The right hand side represents a radio-loud AGN with its jet. The left hand side represents a radio-quiet AGN (Seyfert galaxy). Note that no jet is present; however there is still a preferred direction defined by the rotation axis. Possible obserser positions are on the outer ring.*

emission also depends upon the viewing angle. As the line o sight gets closer to the jets axis, the relativistic beaming becomes greater and the apparent size of the emission region becomes smaller. Therefore the variability time scale decreases as the viewing angle decreases.

AGN viewed at small angles should be identified with blazars. While fewer than $\sim 1\%$ of all AGN are blazars, these objects are the most interesting for the high-energy γ-ray astronomy, since all of the 60 MeV-GeV extragalactic sources detected by EGRET and both of the extragaleactic TeV sources observed by ground-based telescopes are blazars. The visible and γ-ray emission from blazars is variable on timescales from minutes to days. Although theories exist as to the causes of this variability, the sparse data do not yet allow any ideas to be tested. The blazar class includes the BL Lacs and optically violent variables. The much more numerous radio-quie AGNs ($\sim$ 85% of all AGNs) are known as Seyfert galaxies and show no evidence of high-energy γ radiation. When the angle between the observer and the roatation axis is greater than $\sim 45°$ one is viewing a larger fraction of the light reflected from the surrounding torus and the reflected light tends to be polarized. This account for the apparent difference betwwen Seyfert 1 and Swyfert 2 galaxies.

BL Lacs deserve special mention. The distinguishing of their emission spectrum is the faintness or absence of emission lines. At the BL Lac class belong all the AGNs that have been observed in the range of VHE: the two extragalactic objects Mkn 421 and Mkn 501 ($>$ 1 TeV) and the 25% of the AGNs detected by EGRET[10]. The two AGNs Mkn 421 and Mkn 501 have been observed by WHIPPLLE (see [10]) and HEGRA (see [11, 12]) showing occasional outbreaks and even with periodic fluctuations. In Figure 1.10 we can see the light curve of the blazar Mkn 501 as measured by the HEGRA telescopes CT1 and CT2 during 1997 observation campaign (see [13] for a detailed description). The short-term flashes point toward very compact sources, i.e., regions in the vicinity of the supermassive ($\sim 10^8 M_\odot$) black hole powering the very strong non-thermal emission of the AGN.

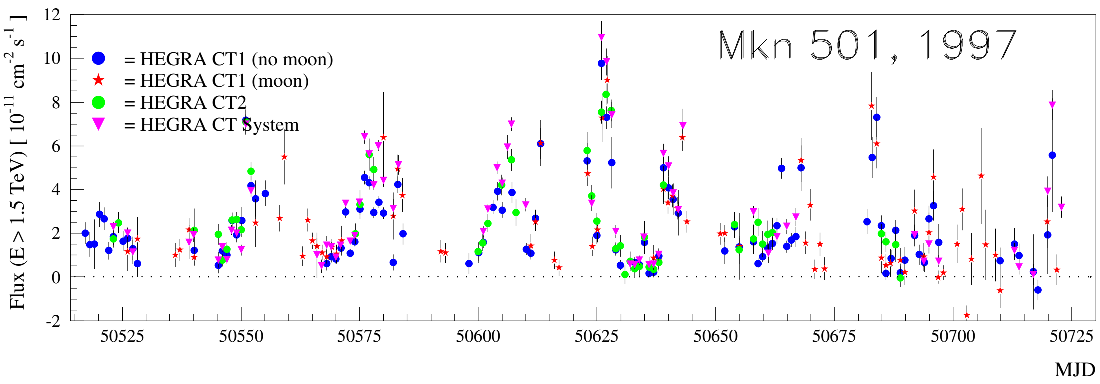

Figure 1.10: *Light curve of the blazar Mkn 501 as measured by the HEGRA telescopes CT1 and CT2 during the 1997 campaign.*

The physics of the AGN is not fully understood, and there are still some open questions. The fact that up to now above 300 GeV only 3 blazars have been detected (the third only by Whipple and only in a short flare), and that only one of these (Mkn 421) has been detected by EGRET shows two thigs: in the unexplored gap between 10 and a few hundred GeV, most of the EGRET detected AGN must cutoff; and there is a probably a whole class of AGN which has its second spectral energy distribution peak in the range above 10 GeV (the first peak for blazars is normally in the UV to X-ray regime). These sources would be difficult to detect by γ-ray satellite experiments, but the MAGIC Telescope would be an ideal tool for their exploration. In addition, the mechanisms which lead to the strong temporal variability of AGN signals in VHE regime remains being a mistery.

1.4.2 Supernova Remnants

Supernova remnants are the expanding shells of hot gas produced as the outer material of the star is ejected at very high speeds (up to 30000 km/s) in the supernova explosion, pushing a strong shock wave ahead of it through the material that surrounded the star when it exploded.

[10]In the GeV regime the majority of observed blazars are optically violent variables. Whether this is a result of the poor statistics or something fundamental is not known.

Supernova remnants may be VHE gamma sources of two different types:

- In the wake of a certain class of supernova explosions, the supernovae of type II and Ia, expanding gas clouds and a very dense core (a neutron star or black hole) develop. These SNRs with a pulsar in their inside are called *plerion type* SNRs. In them, the γ-rays are expected to be radiated from the core.

- Around 90% of the known supernova remnants belong to the *shell-type* class. These remnants look like hollow shells since the do not have a pulsar inside. In these SNRs, the radiation came from the expanding cloud. According to the standard model of cosmic ray origin, the shells of these types of SNRs are sites where the cosmic ray nuclei are accelerated to very high energies (up to $\sim$ 1 PeV). If so, they should also copiously produce γ-rays. Presently, the theoretically favored production mechanisms for γ-radiation are inverse Compton scattering of synchroton or background field photons by VHE electrons and π^o decay into γs after the interaction accelerated hadron with the interestellar medium.

So far, only three SNRs (Crab Nebula, Vela and SN 1006) have been detected at very high energies. The strongest is the Crab Nebula, showed in Fig. 1.11, a unique SNR of the plerion type used as a calibration source in IACTs. But still a systematic high-sensitivity scan of candidates, most of them lying in our own galaxy, has to be done.

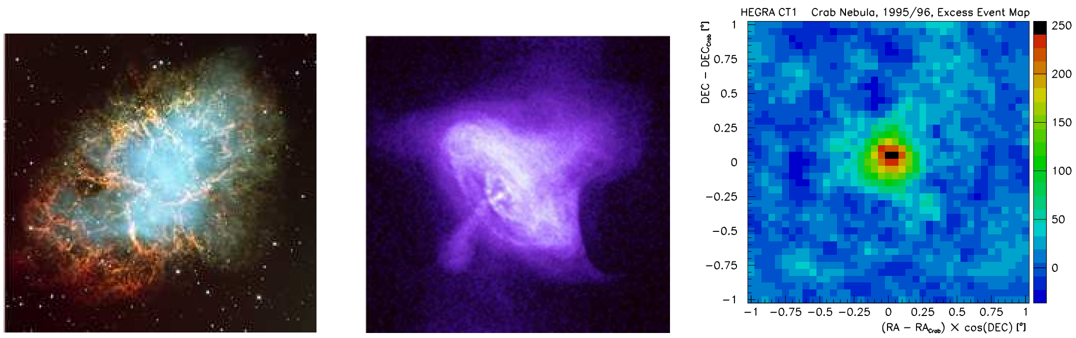

Figure 1.11: *The Crab Nebula is the remnant of a supernova which occurred in 1054 a.D. In the center of the remnant there is a pulsar with a period of 33.4 ms. On the left, image in the optic range taken by the NOT telescope; on the center, image in X-rays taken by the Chandra telescope in the 1-10 KeV band; and on the right, image above 1.5 TeV obatained with the HEGRA Cherenkov telescope CT1 (the absolute pointing accuracy is 0.02°, which is about two times worse than what we expect for MAGIC.*

Presently 215 SNRs are catalogued in our galaxy and approximately 50% of these could be observable with ground-based telescopes at energies above 10 GeV. The characterization of each of these SNRs in the region above 10 GeV is a clear-cut task which can be made by the MAGIC Telescope within a few years. The identification of GeV to TeV γ-rays from radio supernovae would introduce a new and potentially large class of astrophysical γ-ray sources. Such detection would offer deep tests of the theories for particle accelertion in radio supernovae and the models for the radio emission. Furthermore, a positive result would provide direct evidence that supernovae are sources of energetic cosmic ray ions, as have been believed for many years.

1.4.3 Stellar accretion-driven system

Compact stellar objects (white dwarfs, neutron stars and black holes) can very probably produce HE and maybe even VHE γ-rays if they have the chance to accrete matter. This is typically possible if they are part of a close binary system with a non-degenerate star from which matter can be extracted and fall onto the compact object. The transferred matter tipically forms an accretion disk. In our context, the following systems are interesting: the X-ray binaries (composed of a neutron star an a main-sequence star), the microquasars (with relativistic jets similar to the radio-loud AGNs) and the cataclysmic variables (made up of a white dwarf and a cool M-type star)

In the early 1980s there were many reports of TeV-PeV γ-ray signals from X-ray binary system like Cygnus X-3, Her X-1, Vela X-1, etc. The detected emission was some times continous and other times pulsed (with the rotation period of the system), but always sporadic and have not been confirmed by more modern detectors. In the last years, only the Durham Group claims have observed emission from two of these objects: Cen X-3 [14], which is the only X-ray binary detected by EGRET, and Vela X-1.

1.4.4 Gamma-Ray Bursts

Gamma-ray bursts (GRBs) are perhaps the outstanding puzzle of modern astrophysics. Discovered in the 1960s by scientists searching for nuclear tests over the Soviet Union, these gamma-ray bursts have been objects for research and speculation ever since. Observationally, GRBs are short duration (1 ms to tens of seconds) powerful bursts of γ-rays which appear about once per day, coming from apparentley random location in the sky and disappearing without a trace. Often, these burst outshines all other sources of γ-rays in the sky combined.

Before the launch of the BATSE detector on board the CGRO satellite in 1991 it was thought that GRBs were caused by some events on galactic neutron stars. If galactic neutron stars were the sources of GRBs, the distributions of GRBs should be similar to the distribution of galactic matter (a thin disk). But after the detection of over 1000 bursts by BATSE in the energy band from 30 KeV to 300 Kev, it was showed that the distribution of GRBs is clearly isotropic, as seen in Fig. 1.12.

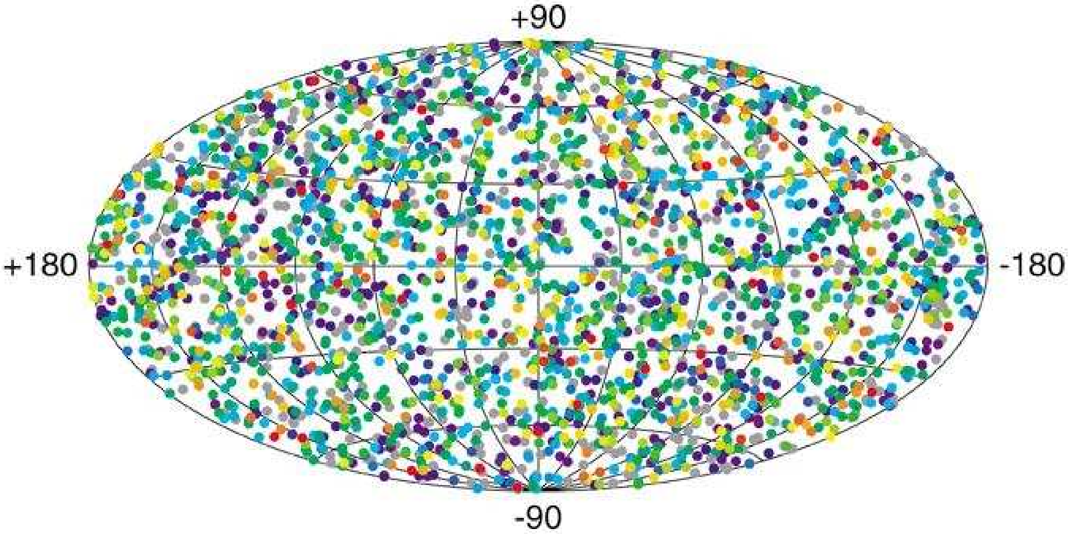

Figure 1.12: *Location in galactic coordinates of 2704 GRBs observed by BATSE during eight years of operation. Showen are the GRBs with sufficient data to calculate the energy received at the Earth, integrated over the duration of each burst. This fluence is measured by BATSE in the medium energy γ-ray band of 50 to 300 KeV.*

The isotropy of GRBs was and important clue about the cosmological origin of GRBs. Nowdays, the favored cosmological model is a relativistically expanding fireball, called the *fireball* model. This model posits that they are indicative of extremely violent explosions (perhaps the aftermath of the merger of a binary neutron star system), releasing in excess of 10^{51} ergs, and creating violent shockwaves as the materials flowing out from the explosion at different velocities collide.

Recently, the launch of the Beppo-Sax detector has supposed and important improved in the determination of the position of the GRBs, which had led to the discovery of a soft X-ray afterglow that may last for days after the initial burst. The precise localization of the burst has also enabled powerful X-ray, optical, and radio telescopes to search for emission from GRBs. Lately, several optical and radio counterparts to GRBs have been observed. The optical counterparts have a visual magnitude of < 20 an a decay time of ~ 1 day. The radio counterparts have a similar decay time. These optical and radio observations are consitent with the fireball model pointing to the cosmological origin of GRBs.

It has been also observed GRBs at higher energies (up to some GeV) by EGRET. These observations indicate that the GRB phenomena may extend up to energies even higher, falling into the MAGIC energy range. And since EGRET bursts lasted approximately 10-100 s, there would be a fair chance of detecting a burst with MAGIC since MAGIC will be able to reach any position in the sky in less than 60 s. For an energy spectrum of E^{-2} the sensitivity of MAGIC will be

75 times better than that of EGRET at 100 MeV.

Clearly the detection of only one GRBs by the MAGIC Telescope and the measurement of its energy spectrum would have very important consequences for our understanding of the nature of this enigma, especially if cut-off features are detected which point to IR absorption and thus to and extragalactic origin.

1.4.5 Unidentified EGRET Sources

The (third) 1999 EGRET catalogue lists (green spots in the Fig. 1.2) 170 unidentified sources for which it was not possible to relate them to known sources observed at different wavelengths due to the limited angular resolution of these detectors. Many of the unidentified populate the galactic equator, hence can be expected to be in our own galaxy. The nature of the large number of unidentified sources discoverd by the EGRET experiment, can maybe be partially uncovered by a more accurate determination of their position.

About 40% of these sources have hard power law spectra which seem to extend beyond 10 GeV. With the high sensitivity of the MAGIC Telescope, these objects can be located with accuracies of $\approx 0.02°$ while the best accuracy reached by EGRET is $0.1°$. Furthermore, the spectral measurements beyond 10 GeV will, together with the results from EGRET, help to classify the sources and identify possible classes of counterparts from satatistical arguments.

1.4.6 Other Contributions to Cosmology and Fundamental Physics

Observations of VHE γs, if done systematically, will also allow to formulate constraints on stellar formation in the early universe, by measuring the extragalactic infrared radiation field. MAGIC could also prove novel astrophysical phenomena which could arise as a result of new physics beyond the current Standard Model of particle interactions. They will further allow searches for the stable lightest supersymmetric particle, the neutralino χ. It is expected (if it exists) to annihilate with its own self-conjugate antiparticle into photons in areas of high gravitational field, e.g. in the vicinity of the black holes of galactic centers (including our own). Direct searches in accelerator experiments place lower limits on its mass $m_\chi \geq 10 - 20$ GeV, whereas, its upper limit mass in most of the supersimetric extensions of the standard model is about 150 GeV. It means that the MAGIC Telescope could be able to detect the annihilation of two neutralinos. Such finding would have a major impact on thinking in both the particle physics and astrophysics communities.

Furthermore, quantum gravity effects might become apparent if subtle time differences can be detected in the arrival of γ-rayss from a given source, at different wavelengths. If they occur in nature, the MAGIC detector has the capability to record such phenomena.

Chapter 2

Extensive Air Showers

2.1 Cosmic Rays

It was not until the experiments carried out by Victor Hess between the years 1911 and 1913, when it was discovered that the Earth is constantly bombarded by a radiation coming from the outer space, the initially called *cosmic radiation*. During the following years, a intense research were maded to try to understand the nature and origin of this radiation, but only starting from 1948, the nature of the cosmic radiation become to be clear. Now we know that the cosmic radiation are basically formed by atomic nuclei (96% H, 3% He, and 1% of heavier nuclei like C, N, O, Fe), electrons, positrons, neutrinos, γ-rays and other types of elementary particles. But the question of their origin is still a matter of discussion. Nowdays, only the charged particles of the cosmic radiation are called *cosmic rays*.

The distribution of the incidence directions of the cosmic rays is nearly isotropic, and their energy espectrum (see figure 2.1) cover a wide range of energies, extending at least up to 10^{20} eV, following a power law given by $d\phi/dE \propto E^{-\gamma}$ with $\gamma \simeq 2.7$.

2.2 Extensive Air showers

Cosmic rays travel from the emission source through the space until them reach the Earth[1]. As they reach the earth's atmosphere and penetrate in it, they interact with the atmosphere molecules, given rise to complicated processes which will produce secondary particles. Likewise, these secondary particles experiment more interaction in their way through the atmospehere, turning into a shower of particles what is called Extensive Air Shower or EAS. The kind of these in-

[1] On their way throughout the outer space, they can suffer interaction with the interstellar medium, as for example fragmentation of the nuclei, ionization, particle producction and many more. This sub-products of the original cosmical particles are the ones that reaches the Earh's atmosphere.

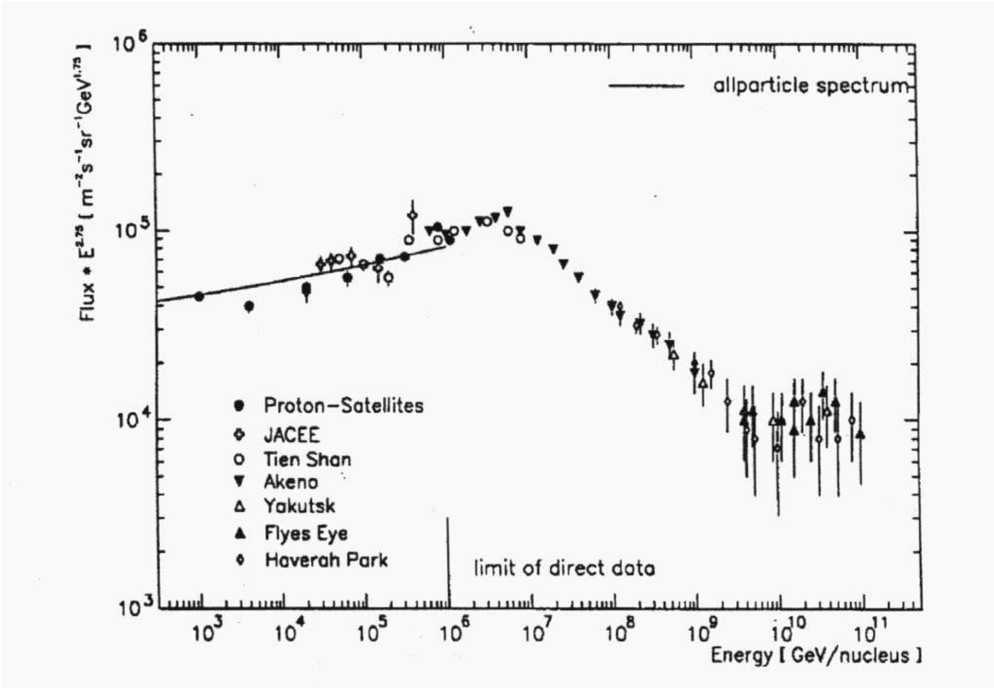

Figure 2.1: *Energy spectrum of cosmic rays.*

teraction, and therefore the kind of shower, depend on the kind of the primary particle.

When a high energy charged particle pass through the atmosphere, apart from the typical electromagnetic processes of ionization energy-loss (as a result of the inelastic collisions with the atmospheric atomic electrons) and the deflection of the particle from its incident direction (due to Coulomb scattering with the atmospheric atomic nuclei), other processes like the emission of radition and, specially a these high energies, nuclear interaction with the atmospheric nuclei and decays come into play. There are two possibles mechanisms by means of what charged particles can release radiation as they cross through the atmosphere: the Bremsstrahlung and Chrerenkov mechanisms. The Cherenkov radiation will be study later in a dedicated section. The Bremsstrahlung radiation is the electromagnetic radiation emitted by a charged particles, mainly electrons and positrons, when they are accelerated by the electric field of a nucleus. At energies of a few MeV or less, this process is still a relatively small factor. But as the energy is increased, the probabillity of bremsstrahlung quickly shoots up so that a few 10's of MeV, loss of energy by radiation is comparable to or greater than the collision-ionization loss. At energies above this *critical energy*, bremsstrahlung dominates completely.

The behavior of photons in the atmosphere is dramatically different from that of charged particles due to lack of an electrical charge. The main process what γ-rays undergo in the atmosphere is the *pair production*, which involves the transformation of a photon into an electron-positron pair. In order to converve momentum, this only can occur in the presence of a third body, usualy a nucleus, and to create the pair the photon must have at least an energy of 1.022 MeV. The pair production begins to be important at energies higher than 1 MeV and it is the dominant effect at energies higher than 25 MeV. Other kinds of interactions can take place at other energies, like the *Compton scattering*, dominant at energies around 1 TeV, and the *photoelectric effect* only relevant at energies below 100 KeV.

The different physical processes that take place when a atmospheric shower is inititated by a γ-ray or by an hadron, lead to observational diffents between both kinds of showers. Next, lets go to study the development and propierties of γ-ray- and hadronic-initiated showers.

2.2.1 Electromagnetic showers

A electromagnetic shower is the result of the combined effect of pair production and bremsstrahlung emission. When a γ photon plunges into the atmosphere, the dominat process at the γ-ray energies is the pair production. Thus, the development of a γ-ray initiated shower starts with the production of a electron-positron pair in the electric field of a atmospheric nuclei or electron. If the energy is sufficient, the resulting electron-pair does not quickly lose its energy by ionizating interactions. Instead they can emit secondary γ-rays via bremmstrahlung in the field of a nucleus. And in turn, these γ-rays can produce another electron-pair which can undergo further bremsstrahlung interactions and so on. The result is a cascade of photons, electrons and positrons (as shown in Fig. 2.2 (left)), which travels in the original direction of the primary γ-ray. Due to multiple dispersion of $e^{\pm}$, the shower particles separate from the direction of the incident photon, forming a disk of some meters thick perpendicular to the incident photon direction that moves to the ground at a velocity close to c. The number of $e^{\pm}$, and γ (less and less energetically) continues increasing progressively in the shower, nearly exponentialy, until the energy of the electrons and positrons drop below the critical energy ($\simeq 100$ MeV in the air). At this point, electrons and positrons will preferentially lose their energy via atomic collisions and ionitation rather than by bremsstrahlung emission, halting the cascade and reaching the shower its maximum development. In this way energy is lost from the shower and the number of particles decreasses as the shower continues to propagate.

We can use a simple model proposed by Heitler (1944) [15] to obtain an estimation of some important characteristics of the electromagnetic showers, such as the height at what the shower reaches its maximum development and the number of particles that the shower contains at that moment. This model is based on the fact that, at these high energies, the radiation length ξ_0 (is the

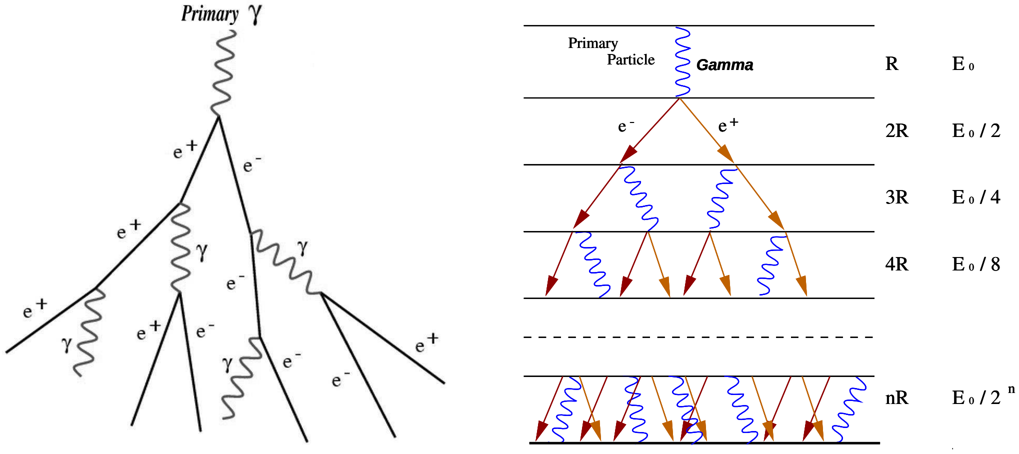

Figure 2.2: *Left: Diagram of an γ-ray initiated shower. Right: Simple model of an electromagnetic shower.*

mean distance over which a high energy electron loses all but $1/e$ of its energy by Bremsstrahlung) for ultrarelativistic electron is approximately equals to the photon mean free path (this is the distance a beam of γ photons must traverse so that all but $1/e$ of them have produced an $e^{\pm}$ pair), since this last is $\sim 9/7\xi_0$. For the atmosphere this quantity equals $\xi_0 \simeq 36.7$ g/cm^2. Then, if we define $R = \xi_0 \ln 2$, the probability that a photon or electron of the shower interacts along a distance R will be: $exp(-R/\xi_0) = 1/2$. Starting from these considerations, in this model it is supposed that both electrons and photons behave like a same particle in the branching process of the shower. That is, a particle (it does not matter whether it is a electron or a photon) travels a distance R in average before it interacts, and after the interaction two new particles emerge. In the model, it is assumed that in each interaction the energy is equally divided between the two new particles formed. This situation is showed in Fig. 2.2 (right). After n branchings, the shower has traversed a depth $X = nR$ in the atmosphere (measured from the top of the atmosphere downward along the direction of the incident cascading particle), and the number of secondary particles in the n^{th} generation is $N = 2^n$. That is, at a deep X we have:

$$N(X) = 2^{X/R} \tag{2.1}$$

and the average energy per particle is $E_0/2^n$, that is:

$$E(X) = \frac{E_0}{N(X)} \tag{2.2}$$

The splitting process continues until the average energy of the cascade particles equals the critical energy, $E(X) = E_c$. After this, the particles are absobed reaching the shower its maximum development. The number of particles ($e^{\pm}$ and photons) at shower maximum in this model is:

$$N(X_{max}) = \frac{E_0}{E_c} \tag{2.3}$$

and the position of the maximum (if we assume that the shower stops abruptly at the critical energy E_c) is:

$$X_{max} = R\frac{\ln(E_0/E_c)}{\ln 2} \tag{2.4}$$

A better approximation for the number of particles produced in a shower as a function of the primary energy and atmospheric depth, is given by the Greisen equation 2.5 [16]. In figure Fig. 2.3 is represented the number of shower particles ($e^{\pm}$) in terms of the atmospheric depth (measured in radiation lengths) with the aid of:

$$N_e(t) = \frac{0.31}{\sqrt{[ln(E_0/E_c)]}} \cdot \exp\left[t \cdot (1 - 1.5 \cdot \ln s)\right] \tag{2.5}$$

where $s = \frac{3 \cdot t}{t + 2ln(E_0/E_c)}$ is known as the age parameter that indicates the degree of development of the shower, and t is the atmospheric depth in terms of radiation length. A value of s = 0 indicates the first interaction point, s = 1 indicates the maximum development of the shower and s = 2 the point in which the shower begins to extinguish.

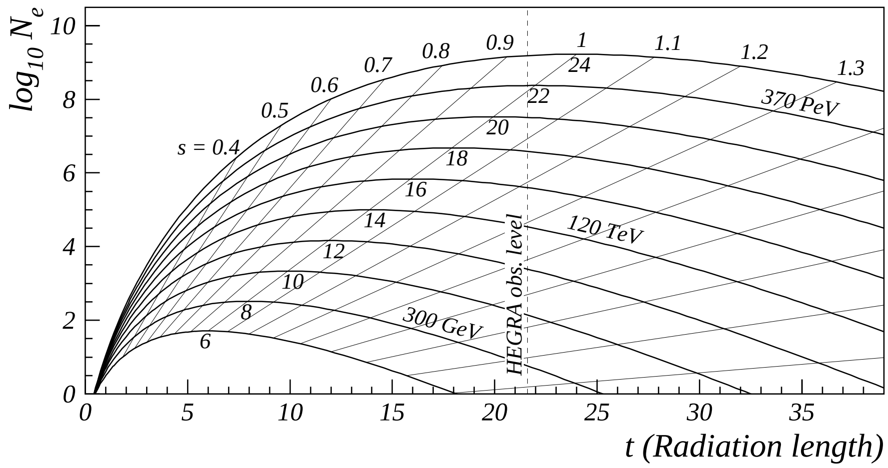

Figure 2.3: *Longitudinal development of an atmospheric shower in terms of atmospheric depth according to the Greisen approximation. Different curves represent different energies of primary photons E_0. The value $ln(E_0/E_c)$ are shown under the curves. At sea level the atmospheric depth is around 27 radiation lengths.*

This model, of course, only gives a rough qualitative picture of the shower. In reality, the number of particles in an electromagnetic shower rises exponentially to a broad maximum after which it declines gradually. In general, a precise calculation cannot be made analytically and recourse must be made to such techniques as Monte Carlo simulations.

2.2.2 Hadronic showers

Vast majority of the EASs are initiated by hadrons, most of which are protons. The shower starts when the primary nucleus collides with an atmospheric nucleus (N or O) producing a nuclear reaction in which part of the energy is converted into matter, being created mainly pions (π^o, π^+, π^-), kaons (K^+, K^-) and nucleons. The fragments of the incident nucleus and the new particles formed, go on travelling through the atmosphere at a great velocity, untill a new nuclear reaction takes place in which more particles are created and so on. As the shower develop in the atmosphere, the number of particles increase up to a depth in which the shower reachs the maximum development, moment in what, particles start to be absorbed by the atmosphere. By example, a EAS initiated by a primary proton of 10^{15} eV produce a shower that reachs it maximum development at ~ 6 Km above the sea level with roughly a million of particles, of which a third can reach the sea level. This produce a shower like the one showed in figure 2.4.

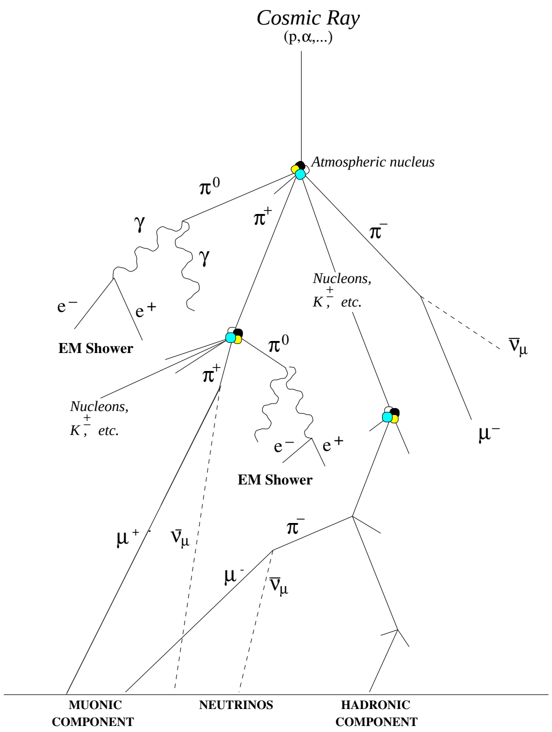

Figure 2.4: *Diagram of an hadronic initiated Extensive Air Shower.*

The fragments of the incident nucleus and the new nucleons formed, form what is named the *hadronic core* of the shower, which go on suffering nuclear interaction as the first one until the energy per nucleon drop under the thereshold energy of pions productions ($\simeq 1$ Gev). The neutral pions π^0 desintagrate almost inmediatly in two γ-rays: $\pi^o \rightarrow 2\gamma$ (with life time in the rest frame of $\tau \simeq 1.8 \cdot 10^{-8}$ s), which suffers the same process that a primary γ-ray described in the previous section, giving place what is called the electromagnetic component of the shower[2]. The charged pions and kaons, either can collide with another atmospheric nuclei producing new particles or desintegrate in one muon and one neutrino: $\pi^{\pm} \rightarrow \mu^{\pm} + \nu_\mu(\overline{\nu_\mu})$ ($\tau \simeq 2.6 \cdot 10^{-8}$ s). The mouns, in their turn, can desintagrate in one electron and two neutrinos: $\mu^{\pm} \rightarrow e^{\pm} + \nu_e(\nu_e) + \nu_\mu(\overline{\nu_\mu})$ in a time of $2.2 \cdot 10^{-6}$ s in their rest frame. In spite of the shorter of their life time, muons can reach the ground without desintegrate. Since their velocities are nearly to the light velocity, they are affected by the dilatation of the time, what produces that in our frame their life time was much larger. Hence, in most of the atmospheric showers a big fraction of the muons produced can reach the ground, and even penetrate hundred of meters underground. In fact, the 75% of all the secondary particles that reach the ground at sea level are muons[3], with an average energy of 2 GeV. The neutrinos produced in the desintegration of pions and muons have a very small probability of interact with the matter in spite of the large number of them (in fact they can go through the Earth).

The simplest model for a hadronic shower is the *superposition model*, in which is supposed that a nucleus of mass A and total energy E_0 is equivalent to A independent nucleons of energy E_0/A. Then, using ξ_N as the nuclear interaction length for nucleons in the air (83 g/cm^2 for a 1 TeV proton), it can be obtain a formula analogous to 2.4:

$$X_{max} \propto \ln \frac{E_0}{AE_c} \cdot \xi_N \tag{2.6}$$

Therefore, for primary hadrons of the same energy, the showers produced for those of larger mass develop higher in the atmosphere.

2.3 Cherenkov Radiation

The Cherenkov radiation is the electromagnetic radiation emitted when a charged particle moves in a dielectric transparent medium at a speed v higher that the speed of light in that medium, namely, c/n where n is the refractive index. This radiation is not emitted by the particle itself, as in the case of bremsstrahlung radiation, but for the medium as a result of the reorientation of the instant elec-

[2]In each hadronic shower about a third of the hadron energy is transferred to the electromagnetic part of the shower.

[3]The reason why much more muons than $e^{\pm}$ and $\gamma's$ reach the ground is because EM showers initiated by photons of $E \leq 500$ GeV are extinguish completaly before reach the sea level.

trical dipoles induced by the charged particle moving in it[4]. We can understand the reason why this radiation is only emitted when the velocity of the particle is high enough. Always that a charged particle goes across a dielectric medium, it induces instant electric dipoles in the medium. If the velocity of the particle is small, the induced dipoles arrange themselves simetrically around the instantaneous position of the particle (as shown in figure 2.5 (a)). This is because the electric field of the particle reach all the molecules around the instantaneous position of the charge at almost the same time, since $v \ll c/n$. Therefore there is not a net polarization of the medium at large distances, and then no radiation is emitted. But if the velocity of the particle is higher than the velocity of the light in the medium no instant dipoles are set in the region ahead of the moving particle, because the particle travels faster than its own electromagnetic field (see figure 2.5 (b)). Thus, along the particle's path is produced a net polarization of the medium, which consecuently radiate brief electromagnetic pulses. These pulses will be only coherent and combine to form a wave front in those points where they get with the same phase. It can be shown with a simple geometrical interpretation of this emission mechanism (Fig. 2.5 (c)), that Cherenkov radiation is only observed at a particular angle Θ, called Cherenkov angle, with respect to the track of the particle. Coherence takes place when the particle travels from A

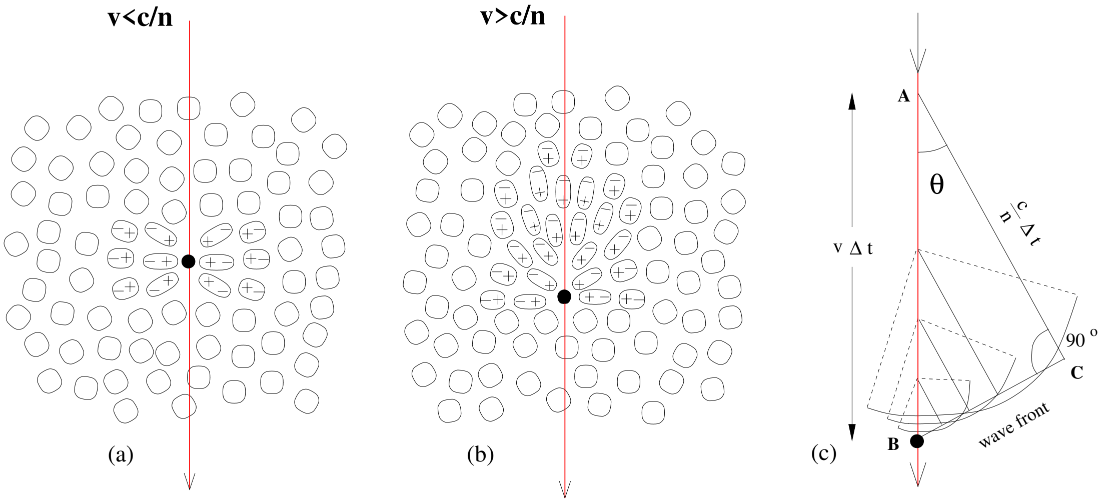

Figure 2.5: *The polarization set up in a dielectric when a charged particle passes through. (a) Low velocity. (b) High velocity. (c) Huygens construction to ilustrate coherence and to obtain the Cherenkov angle Θ.*

[4]The distinction between the two types of radiation appears with particular clarity when the particle has a very large mass: bremsstrahlung disappears, but the Cherenkov radiation is unaffected. In addition, bremsstrahlung is produced by the acceleration of the particle, whereas, the Cherenkov radiation requires that the velocity of the charged particle that disturbe the medium was constant.

to B in the same time that the light travels from A to C. If $\beta = v \cdot c$ and $c/n(\lambda)$ is the velocity of the Cherenkov light in the medium with $n(\lambda)$ the refractive index, then, from geometrical considerations the Cherenkov angle is:

$$\cos\Theta = \frac{1}{\beta \cdot n(\lambda)} \tag{2.7}$$

The more important features of the Cherenkov radiation are:

- From equation 2.8 we can take out the following implications. For a medium of refractive index n, there is in fact a threshold velocity $\beta_{min} = 1/n$, below wich no radiation takes place. For this critical velocity, the direction of the radiation coincides with that of the particle. And the maximum emission angle is $\cos\Theta = 1/n$, which corresponds a ultra-relativistic particles ($\beta = 1$).

- *Spectrum of Cherenkov light.* In a medium with a refractive index n, the number of Cherenkov photons emitted per unit path length and per unit energy interval (or equivalently to λ) when a charged particule of charge ze and velocity β pass through it, is

$$\frac{dN^2}{dx d\lambda} = \frac{2\pi\alpha z^2}{\lambda^2} \cdot \left(1 - \frac{1}{\beta^2 \cdot n^2(\lambda)}\right) \tag{2.8}$$

  where α is the structure constant. This means that most of Cherenkov light is emitted in the ultraviolet region of the spectrum, since $dN^2/dxd\lambda \propto 1/\lambda^2$.

2.3.1 Cherenkov Radiation in EAS

Already in 1948 Blackett suggested that the charged particles of the atmospheric shower produce Cherenkov light and he estimated that its contribution to the light of night sky background is about 10^{-4}. The emission of this Cherenkov light by the EAS is of great important in γ-ray astronomy based on Earth. For instance, whereas for primary particles which energies less than 20 TeV the cascades die out in the upper atmosphere, the Cherenkov radiation produced in the shower penetrates to ground level where it might be collected. Although subject to fluctuations in the point of origin of the cascade and in its subsequent development, the Cherenkov light carries with information pertaining to the exact point of the origin of the primary γ-ray on the celestial sphere, and also of the energy of the primary particle.

Vast most of this Cherenkov radiation is produced by the electrons and positrons. But as we have seen, so that Cherenkov radiation was emitted the velocity or energy of the charged particle has to exceed a minimum threshold energy E_{min}. This critical energy, as well as the Cherenkov angle, varies with height since the Cherenkov threshold velocity depend on the refractive index of the atmosphere. At see level ($n \simeq 1.00029$) this energy threshold is 21 MeV and the maximum Cherenkov angle is 1.4° (remind that the average energy of $e^{\pm}$ at the shower maximum is about 100 MeV) and increases to 35 MeV at 7.5 Km above sea level.

We can make an estimation of E_{min} and Θ_{max} for differents heights in the atmosphere, by means of using a simplified model of it. We will suppose that the density of the atmosphere change exponentially with height:

$$\rho(h) = \rho_0 \cdot e^{-\frac{h}{h_0}} \tag{2.9}$$

where $h_0 = 7.1\,Km$. Starting from this law, we can calculate the refractive index at the height h as:

$$n(h) = 1 + \delta_h = 1 + \eta_0 \cdot e^{-\frac{h}{h_0}} \tag{2.10}$$

where $\eta_0 = 2.9 \cdot 10^{-4}$. Since electrons and positrons have to move at least at the velocity of the light in the atmosphere to radiate Cherenkov photons, then, their minimum energy E_{min} will be that which correspond to a relativistic particle moving at a velocity $v = c/n(h)$

$$E_{min} = \frac{m_e\,c^2}{\sqrt{1 - \frac{v_{min}^2}{c^2}}} = \frac{m_e\,c^2}{\sqrt{1 - \frac{1}{n(h)^2}}} \approx \frac{0.511\,MeV}{\sqrt{2\,\delta_h}} \tag{2.11}$$

where we have simplified using the fact that $\delta_h \ll 1$. The maximum Cherenkov angle θ_{max} (which correspond to $\beta = 1$) at which the Cherenkov light is emitted varies with height, according to the expresion:

$$\cos\theta_{max} = \frac{1}{n} = \frac{1}{1 + \delta_h} \simeq 1 - \delta_h \tag{2.12}$$

that can be approximated as:

$$\theta_{max}(rad) = \sqrt{2\,\delta} \tag{2.13}$$

For a single relativistic particle moving high in the atmosphere, the Cherenkov angle is less than a degree, but opens to about 1 degree at 8 km altitude, and due to the greater air density, opens to about 1.4 degrees at see level. Because all of the emitting particles are ultra-relativistic the Cherenkov angle is satured.

Lateral Distriubution of the Cherenkov Light

The variation of Cherenkov angle with height conbined with the fact that the charge particles move to the ground give rise to a geometrical effect, the formation of the so-called *Cherenkov ring*. To see it, let us go to obtain the distance R_{core}

of the emitted Cherenkov photons to the particle trajectory, which depends on the height at a certain observation level h_0:

$$R_{core}(h) \equiv (h - h_{obs}) \cdot \tan\theta_{max} \tag{2.14}$$

In figure 2.6 (left) the dependence of E_{min} and R_{core} with height above sea level is presented. The values for R_{core} were obtained for an ultrarrelativistic electron of vertical incidence and for two observation levels, the one corresponding to the HEGRA experiment, h_{obs}=2200 m, and for sea level. We can see that R_{core} has a maximum between 10 and 20 km. This makes all the Cherenkov light emitted by the particle between this two heights to reach the observation level in a narrow ring of about 10 m width and with a radius of around 120 m. (for sea level), the called *Cherenkov ring*. In the same figure (right) we see and sketch of how the light emitted at differents heights reachs the ground at roughly the same distance frome the incident particle, giving rise to the characteristic ring of Cherenkov light around the particle impact point.

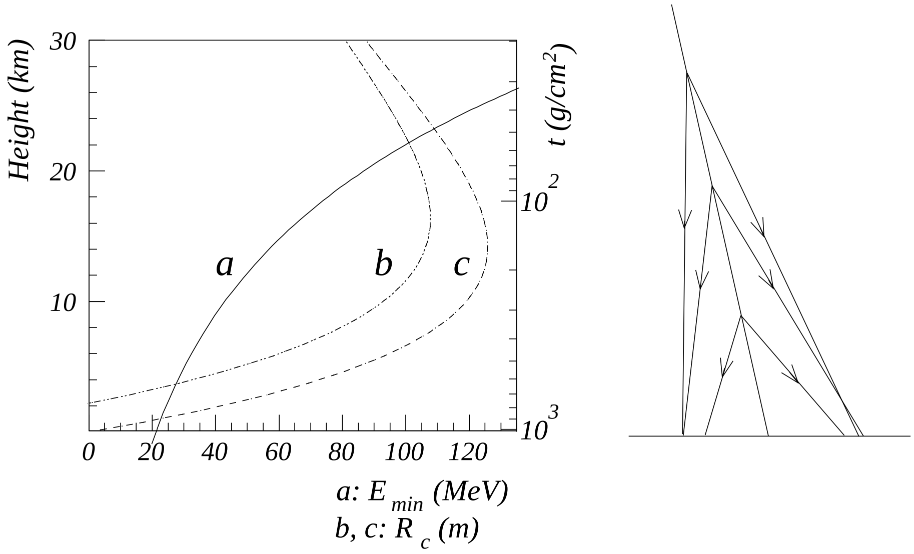

Figure 2.6: *Left: Dependence of E_{min} (curve (a)) and R_{core} (curves (b) for and observation level at 2200 m, and (c) at sea level) with height for an ultrarrelativistic electron of vertical incidence. Right: Origin of the Cherenkov ring.*

The above discussion was only for a single particle moving through the atmosphere. In a EAS, if all charged particles move along the shower axis with no lateral displacement, all the light produce in the shower would be still focus into a narrow anular strip. As an approximation, for a 1 TeV γ-shower light generated from heights between 6 to 10 Km above sea level would fall on ground within a ring of 110 to 145 m in radius from the shower impact point, if electrons did not multiple scatter. But what actually happens is that the direction of the emissors diverge from the primary particle due to the multiple Coulomb scattering that they suffers in their way. This produces that this structure was blur, broadens the Cherenkov ring. Although it does not disappear completaly for low energy showers, giving rise to a *hump* in the lateral distribution of the Cherenkov light. In Fig. 2.7 (right) it is shown the formation of the hump. 50% of the light is generated between 6 to 10 km and falls in the so-called the hump of the Cherenkov pool. The other 50% is split equally between both higher and lower altitudes. As it can be seen, every radial distance on ground from the core, represents a different atmospheric height: the main bulk of particles, near shower maximum, produces the light seen at 100-130 m from the shower axis. Close to the shower axis (within 40 m) one sees the light from local particles, the tail of the shower.

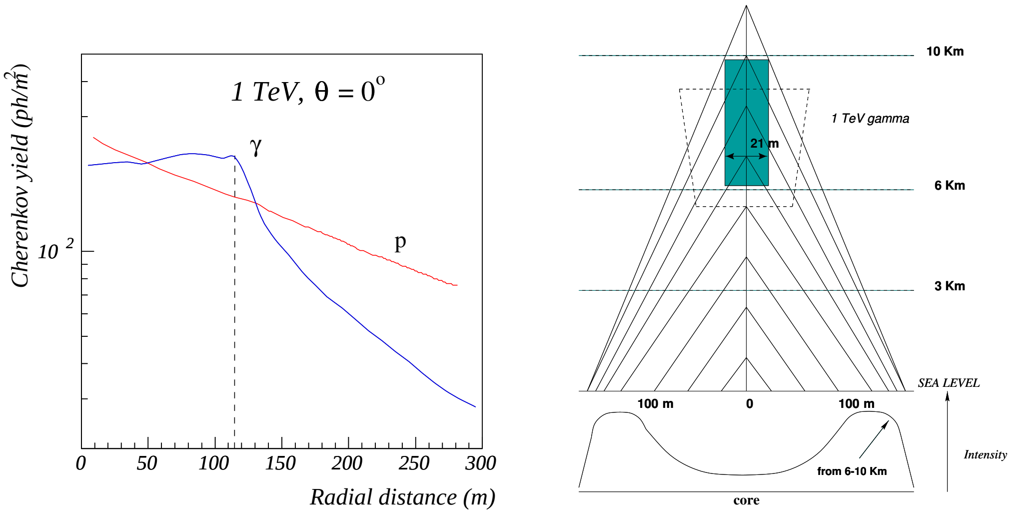

Figure 2.7: *Left: Lateral distribution of Cherenkov light yield on the ground for typical γ-ray and hadron showers. The γ-ray induced shower shows a relatively flat lateral distribution of light out to about 125m radial distance from the center. Right: Geometric model of emission of Cherenkov radiation for γ-ray and hadron showers. The stippled region encloses the main emission region for production of Cherenkov light from γ-ray showers. The intensity profiles on the ground reflect the peaking in the Cherenkov lateral distribution for γ-ray showers at distances to about 125 m from the center of the light pool. For a proton cascade of the same primary energy the same column is represented in dashed line.*

The Cherenkov ring is most prominent when the shower dies out far above the observtion level, as in low enegy γ showers. This effect also depend on the kind of primary particle, as can bee seen in Fig. 2.7 (left). In the figure we see the lateral distribution of Cherenkov light at 2200 over the sea level originated by a 1 TeV photon and proton of vertical incidence (with its maximum at 8.2 Km) obtained by means of a Monte Carlo simulations. It can be seen clearly the hump for the γ shower. But in the shower initiated by the hadron this structure is not so pronounced due to the contribution of the large transverse momemtum of the products of the nuclear interactions. In addition, the interaction length for a primary proton in the atmosphere is about 80 gm cm^{-2} compared to about 38 gm cm^{-2} for γ-rays, therefore proton showers will develop further into the atmosphere. By propagating much further into the atmosphere, the proton induced shower carries a Cherenkov component much closer to the ground level than γ induced showers, and this is reflected in a more intense pool of Cherenkov light close to the shower axis not presenting the ring shown in γ-initiated showers. With greater particle transverse momentum spread and a more ragged penetration into the atmosphere, hadronic showers fail to exhibit any discernible focused ring.

One interesting feature of the Cherenkov pool left by γs is the regularity of it in contrast to the hadron one that shows more irregularities. This is because when a cosmic ray enters the atmosphere, among other particles, three types of π-mesons can appeared. Only the π° can decay to produce γ-ray pairs, thus sustaining electromagnetic processes within the cascade. In first order we could say that 1/3 of the energy of the primary particle goes to the electromagnetic component of the shower. So in principle for the same primary energy hadronic showers will show a Cherenkov pool on ground less intense. On the other hand, in hadronic showers there is other sources of Cherenkov emission other than electrons and positrons that contribute to the Cherenkov pool as can be the muons. This muons do penetrate to the ground over a wide area and an intense local peak of Cherenkov light is seen around each muon impact point. The Cherenkov photon distribution on ground shows more irregularities for the proton initiated showers due to the different components of emission, being the pattern more chaotic. Thereby, γ-ray showers are more compact and this is one of the basis of the shape and compactness of Cherenkov images recorded by suitable focusing instrument, and plays an important role for the γ/hadron separation process.

Another important fact of the Cherenkov radiation is the pulse shape. The Cherenkov pulse shape seen at a distance R_c from the core depends on the shower geometry and shower development, as well as on the variation of the refractive index with altitude. Simulation shows that at small core distances Cherenkov light produced low in the atmosphere reaches the ground first. We can assume that light reaching ground at a given time t comes from a particular atmospheric height.

Atenuation of the Cherenkov Light in the Atmosphere

At the Cherenkov light goes through the atmosphere downward, it undergoes an attenuation due to different processes:

- Absorption by ozone: almost all Cherenkov photons with a wavelength below 290 nm are absorbed in the reaction $O_3 + \gamma \rightarrow O_2 + O$.

- Absorption by H_2O and CO_2 molecules of photons with wavelength above 800 nm.
- Scattering by air molecules (Rayleigh scattering). It depends on the wavelength as λ^{-4}.
- Mie scattering.

The dependence of the attenuation with λ causes that the Cherenkov photon spectrum has a peak at around 330 nm. On the other hand, the night sky background increases as λ increases. Thereby, the optimal spectral range for the detection of Cherenkov light produced in atmospheric showers is around 300-600 nm.

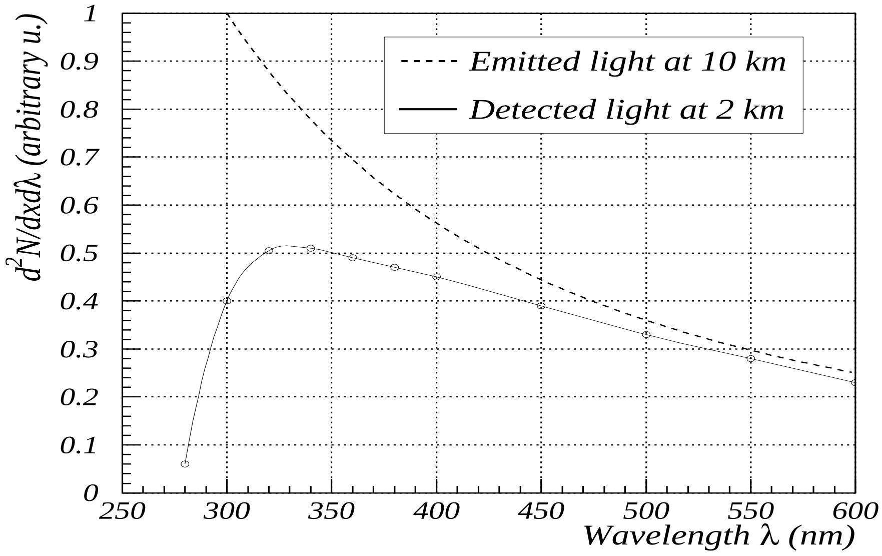

Figure 2.8: *Differential Cherenkov photon spectrum. Continous line includes absorption by ozone and Rayleigh and Mie scattering. The spectrum has a peak at around 350 nm.*

Chapter 3

The MAGIC Telescope

MAGIC is a 17 m Ø diameter IACT telescope currently under construction which will be installed at the Canary island of la Palma (28.8° N, 17.9° W) at the beginning of 2002. The main goal of the experiment in its first phase is to reach an energy threshold as low as $\sim$ 30 GeV with a sensitivity higher than any other detector currently working. This will allow for very first time close the gap existing between satellite γ-ray detectors and ground-based telescopes. The low γ-energy threshold of the MAGIC Telescope will be an important tool for studying a number of fundamental problems in Astrophysics, Cosmology and Particle Physics, as summarized in §1.3 and §1.4.

As we already mentioned, the energy threshold of an imaging Cherenkov telescope relates inversely to the mirror area and to the light collection efficiency:

$$E_{thr} \propto \frac{1}{\sqrt{A_{mirror} \cdot LCE}} \tag{3.1}$$

where the light collection efficiency is given by the product of several terms $LCE = R \times LG$ (if used)$\times QE \times CE$ where R is the reflectivity of the mirrors, LG denotes the light guides efficiency, QE is the quantum efficiency and CE is the collection efficiency of the photosensors used. As a matter of fact, in order to lower the energy threshold, the mirror area and the LCE of the photosensors have to be enlarged. For designing a big telescope, one option will be to build a relatively light weight telescope, allowing for small deformations monitored and corrected for by application of the active mirror control. This also would provide a low inertia, which is important for the fast positioning of the telescope. Besides, the LCE can be improved by using high reflectivity mirrors, light concentrators such as Wiston cones (see below), and high quantum efficiency photosensors. All these consideration have be implemented in the design of the MAGIC Telescope.

3.1 Physical Consideretion on the Design

In determining the main design parameter of a telescope operating in the sub-100 GeV energy domain, the characteristic development of air showers initiated by incident particles at this low energy has to be considered. As we already pointed out in the previous chapter, whereas an energy of a few GeV is sufficient to produce air showers that contain many electrons above the Cherenkov threshold, a large fraction of the Cherenkov photons is lost due to Rayleigh and/or Mie scattering and ozone absorption in the atmosphere. This effect is most pronounced in hadron showers due to the higher Cherenkov threshold of hadrons and muons compared to electrons. As hadron induced air showers produce less Cherenkov light than γ induced ones, a natural γ/h separation at the threshold is implemented in all IACT applications. This inherent hadron suppression factor increases at lower energy. A telescope sensitive at $\sim$ 10 GeV will therefore have excellent intrinsic hadron rejection capabilities already at the threshold. The constraints on hadron rejection efficiency based on image analysis can thus be less demanding in this energy domain. On the other hand, the low absolute photon density within the light pool for γ-ray induced air showers leads to the main requirement for the MAGIC telescope to have a large light collector.

3.2 The Telescope

In Fig. 3.1 it is shown a computer generated image of the telescope. The main mirror support dish consists of a three layer space frame made from carbon fiber-epoxy tubes, which are both lightweight and rigid. One essential requirement

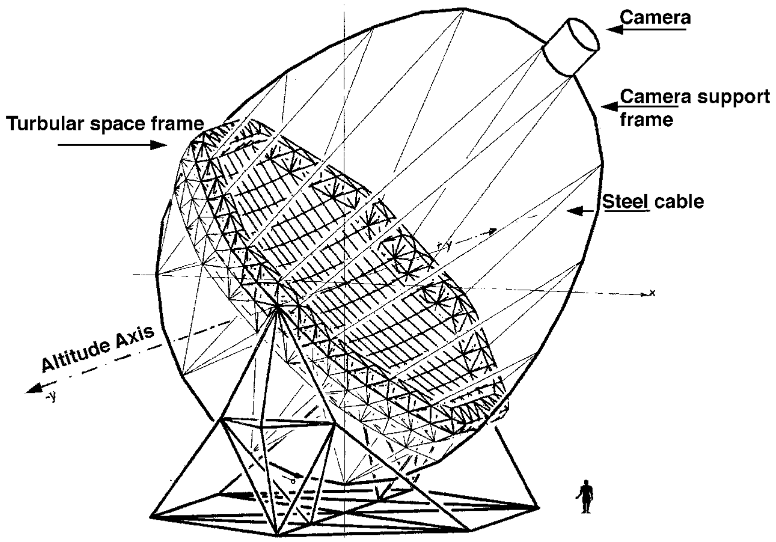

Figure 3.1: *A model of the 17 m Ø MAGIC Telescope*

is that the inertia of the telescope must be low so that it can be repositioned for GRB searches within 30-60 s at any position in the sky. A finite element analysis of the frame has shown that de deformation can be held below 3.5 mm with respect to the nominal curvature at any position for a combined frame and mirror weight of less than 9 tons. It also guarantees wind resistance up to more than 165 km/h and stability for complete ice cover up to 3 cm thickness.

MAGIC will have a 17 m Ø octogonal shape tessellated 1/1 reflector. It will consist of 976 mirror tiles, 936 of them measuring 49.5x49.5 cm^2 each, and the rest 40 tiles will have a triangular shape with the half area of the square mirror ones. The general curvature of the reflector, providing a mirror surface area of ~ 236 m^2, will be parabolic, whereas the curvature of the mirror tiles will be spherical. In order to approximate the parabolic shape of the reflector by using the mirror tiles, the reflector zone will be divided into 8 concentric zones with different radius of curvature, between 34 and 36 m depending on its distance from the reflector's optical axis. Within any given zone the tiles will have the same radius of curvature. The basic mirror elements are lightweight sandwich aluminum panels (see Fig. 3.2), equipped with internal heating to prevent dew and ice deposits. A high quality reflecting surface, with asurface roughness of < 10 nm, is achived by diamond turning. A preproduction series showed high optical quality with a typical focal spot diameter of 6 mm.

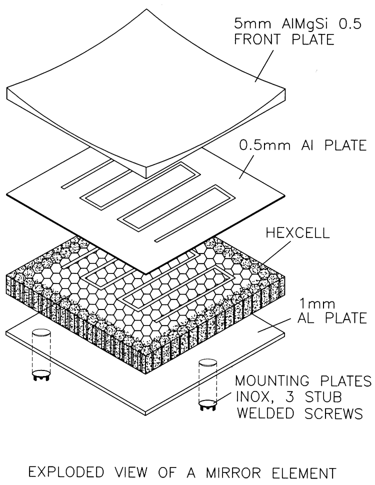

Figure 3.2: *Exploded view of a mirror element.*

Although the mount is very rigid in itself, it is planned to use a novel technique of active mirror control for making mirror adustments and small corrections during telescope turning, in order to counteract small residual deformations of the frame. It works on lightweight panels of 4 preajusted mirror elements which are ajusted by two steeping motors. A laser pointer attached to the panel sends light in the direction of the panel itself, and a videocamera will record the position of the light spot on the casing of the camera. From comparison of the actual spot with the nominal one, the steering commands will be derived.

The light from the γ-shower is reflectd by the mirrors and projected onto a 0.85 m^2 camera where the conversion light signal to electric signal takes place by means of photosensors. Nevertheless, the electric signal is not digitized there. In order to minimize the camera weight, size and heat dissipation, most ot the trigger and readout electronic is not located in the camera of the telescope, but on the ground; in the counting house. It is planned to use low-weight optical fibres for the transmision of the PMT signals to the counting house, instead of heavier coaxial cables, in order to provide noise immnunity and to minimize the time dispersion of the signals.

The timing information from the camera is important to reduce the LONS and improve γ/hadron separation by explotng the isgnal arriving and the signal time sturcture in the individual camera cells. For that, a 300 MHx. 8-bit Flash ADCs (FADC) system will be used which will be replaced by ≥ 1 GHz system in future to make full use of the potential of the new PMTs and the analog transfer scheme.

3.3 The Camera

The camera is the decesive element for improving the gamma sensitivity, the γ/hadron separation power and to reduce the energy threshold. Historically, IACT cameras underwent a development for a single PMT version to cameras with a few hundred pixels. The progress of the last years can mainly be attributed to finer pixelized cameras allowing the subtle differences between hadron and γ showers to be revealed[1]. Hand in hand with finer pixels there has been an improvement in the trigger efficiencies for γs, in the γ/hadron separation, in the angular resolutions, and also a slightly improvement in the energy resolution due to the better determination of the shower maximum location in images, particularly of low energy events.

For the design of the camera one has to take into account that images from low energy showers ($<$ 100 GeV) will be rather compressed and rather close to the camera center, demanding fine pixelization of the camera in the central region. On the other hand, high energy showers will be more extended (up to $1.5° - 2°$) because they reach further down in the atmosphere, hence requiring the camera to be large enough to contain the whole image of the γ shower. Therefore, the diameter of the camera is, in addition to the pixel size, a critical issue, since the information about the shower tail is extermely valuable for γ/hadron separation, energy resolution, and for solving the head/tail ambiguity of images.

These requirements on the pixel size and camera diameter influence the configuration and size of the camera.

3.3.1 Camera Layout

A schematic view of the layout of the geometrical pixel pattern of the MAGIC's camera is shown in Fig. 3.3. The camera will have a field-of-view of $3.6°\,\varnothing$ ($4-5°\,\varnothing$ in a later stage) and will be composed of two regions. The inner part of the camera, from the center up to a radius of $1.25°$, will be equiped with 397 high QE pixels $0.1°$ in size. Whereas the outer part will be composed of 180 pixels $0.2°$ in size. This part extends from $1.25°$ up to a radius of $1.8°$ and is sufficient

[1]According to measurements principles, the pixels size should be $\leq 1/2$ of the quantity to be measured, that is $\leq 0.1°$.

for the observation of the tails of high-energy showers where plenty of light is generated anyhow. The specific design requirements are:

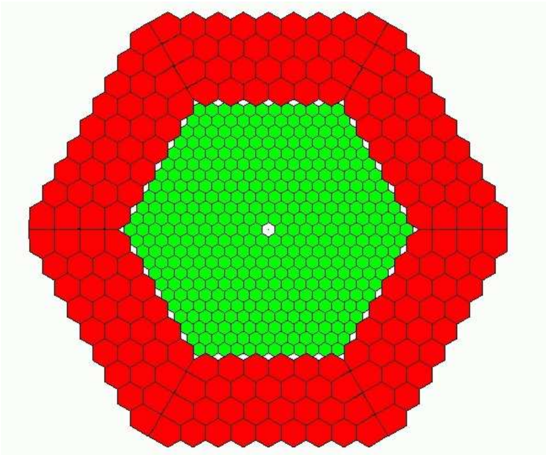

Figure 3.3: *Geometrical pixel pattern of the design of the MAGIC Telescope's camera*

- Fine granularity. The chosen fine pixel granularity of the inner camera section allows to achive a better than 0.01° precision in point source location on the sky, eventually making it possible to observe extended sources and two close point sources separated by $> 0.2^{\circ}$. The small pixel size also helps in the reduction of night sky background in individual images allowing to reduce the trigger threshold preset on the discrimintor level. In addition, a fine granularity is crucial for the image analysis needed for efficient γ/hadron separation.

- Large field of view. The 3.6° camera field of view ensures a full containment of the shower images, hence a good energy resolution and γ/hadron separation.

- No dead space between pixels. For constructing reasons, PMT have a sensitive area significantly smaller than their outer dimensions. Therefore, even in a physically very dense package a sizable fraction (about 50%) of the light will be wasted. A way out is to install light funnels named Wiston cones, which are now in use in many telescopes. In MAGIC, we will use hexagonal to round hollow light funnels shaped like Wiston cones (see Ref. [17]) and a nearly 100% active area camera is achived by placing a plate of these light concentrators cones in front of the photodetector matrix (as seen in Fig. 3.3). These cones achive two goals: firstly to concentrate without losses the light entering the (hexagonal) pixel entrance area onto the restricted (round) active area of the photodetectors and secondly, to reject the background light outside the aperture defined by the mirror dish.

The prime focus dectector package (including the camera, HV generators, preamplifiers, optical fibre drivers and housing) will weigh about 150 kg. The detector package will be circular to allow for rotations by means of equipping it with steeping motors that allow rotation up to 180°. This will allow to maintain the orientation of the star field in the camera coordinate system throughout the course of each observation, a feature of particular importance for the study of extended objects.

3.3.2 The Light Sensor Options

In addition to a large collector, the light collection and light conversion efficiency need to be optimized for operation in the sub-100 GeV domain. For the light sensors three options have been envisaged: classical photomultipliers, hybrid photomultipliers (HPDs) with higher quatum efficiency, and avalanche photo diodes (APDs) as a possible option in the future.

In the first stage of the MAGIC telescope, the phase I, the camera will be equipped with bialkali photocathode PMTs. The new compact hemispherical 6-dynodes PMTs from Electron Tubes 9116A (25 mm Ø) as inner pixel, and D567B (38 mm Ø) as outer pixel have been designed and already tested (see Ref. [18]) to match most of our requirements. In Fig. 3.4 these PMTs are shown.

Figure 3.4: *PMTs that will be used in the MAGIC's camera (phase I).*

The classical PMTs with a bialkali photocathode and borosilicate windows are well suited for the observation of Cherenkov light from showers in the TeV region. The spectral cutoff of standard glass windows is reasonably matched to the ozone cutoff of the atmosphere while the QE peaking between 300 and 450 nm is well matched with the UV peaking of the Cherenkov light. In addition, the contribution or the LONS in the UV is rather low. However, the situation changes quite significant when distant showers are observed, i.e., when observing at large zenith angles or when observing low enegy showers which stop high up in the atmospeher. Rayleigh and Mie scattering will scatter most of the short wave Cherenkov photons in such a way that the remaning spectrum at the detector level shifts peaks to higher wavelengts. For example, at a zenith angle of 75° the spectrum is rather flat between 400 and 600 nm with its peak around 450 nm, whereas below 350 nm almost no light at all is observed. Therefore it is desirable to have red-extended (up to $\sim$ 600 nm) photocathode sensitivity. Thereby, in a second phase, we intend to implement a camera made out of hybrid PMTs (HPDs) with a GaAsP photocathode produced by INTEVAC Inc., with a 1 mm Ø GaAs PIN diode as anode[2]. This typpe of HPDs is characterized by a remarkably high QE of about 45% that extends into the red part of the spectrum, which will reduce the LONS since the value of $S/\sqrt{NSB}$ increases more slowly than S as a function of wavelength. Another strong argument in favor of using red-extended light sensors comes from the prospect of carrying out observations in the presence of moonlight. Unless one is observing within a few degrees around the moon, one is confronted only with a background of scattered moonlight, which will shows peaks around 400 nm with nearly half ot its photons below thiw wavelength. The QE in the blue will be increased to the same level by the applications of wavelength shiter dye.

A future option (in a third phase) will be an all-silicon avalanche photodiode camera. Solid state devices with internal photoeffect (Si, GaAsP,...) have a QE of 80%, which is still higher by a factor of 2 than that of the Intervac GaAsP vacuum photodetector. Though APDs could already be used for Cherenkov telescopes, their full advantanges canot yet be entirely explotied due to their relatively high noise level (see Ref. [19]).

In Fig. 3.5 the QE of the bialkali PMT is compared to the QE of an HPD, an APD and to the QE of an HPD covered by wavelength shifter dye.

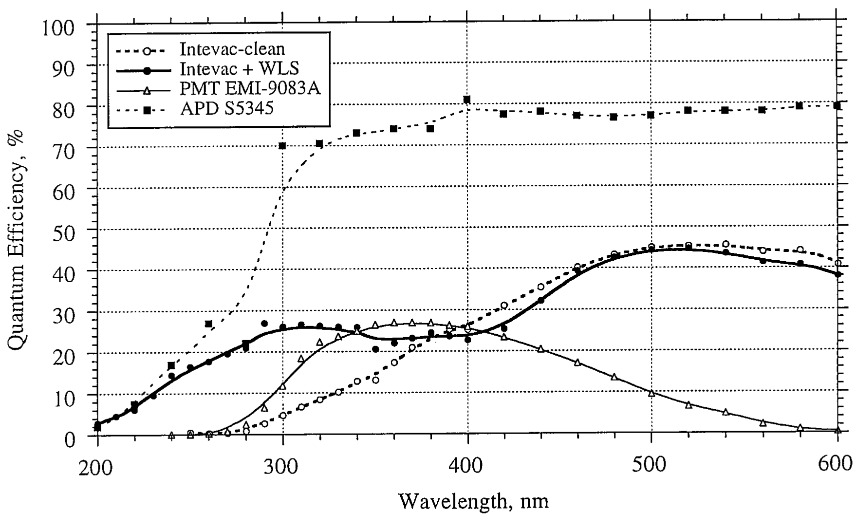

Figure 3.5: *Spectral QE of an bialkali PMT compared to an INTEVAD HPD, to an APD and to an INTEVAC tuve coverd by wavelength shifter dye.*

Nowdays, the restricted size of the active area and the price of both GaAsP HPDs and high gain APDs are the most limiting factors. However, the recent progress in the field allows one to hope to make use of them for full-scale IACT detecetors in a few years from now.

[2]In this photosensor, the photoelectrons are accelerated by a cathode to an anode voltage of 2-10 kV ca. and generate up to about 1500 electron-hole pairs in the diode.

3.3.3 The Camera Electronic Readout Chain

Specific featured of the MAGIC camera electronic chain (Fig. 3.6) are the use for a fast low noise transimpedance amplifier, analog signal transfer through the 70 m optical cable, and signal digitalization by FADC.

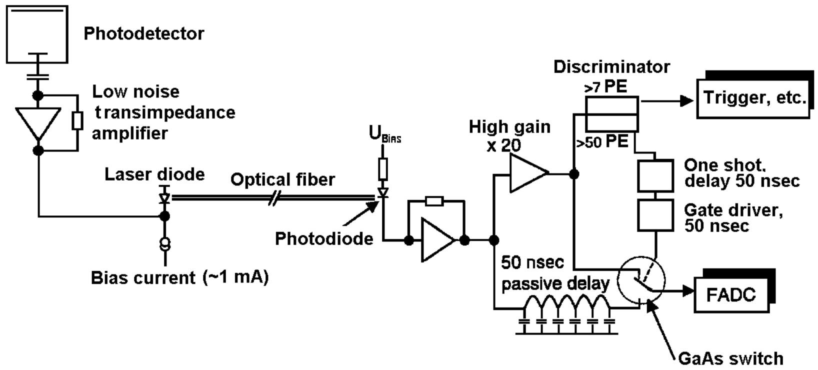

Figure 3.6: *The MAGIC camera readout electronic chain.*

The PMTs of a IACT must work with low amplifiction due to the LONS, specifically is one wants to operate in the presence of moonlight, which can increase the normal rate easily up to a factor 30 (see Ref. [20]). In the case of MAGIC, in order to keep the PMT current flow produce by the LONS at the level, of say $1 \sim \mu$A, then, the PMT gain should not exceed $(1-2)\cdot 10^4$. But the signal needs further amplification in order to drive the optical analog glass fibre system. For that, to compensate the low PMT gain, the PMTs will be followed by a fast $\sim$ 1 GHz bandwidth transimpedance amplifier with a gain of 7-10, providing a single *phe.* amplitude of 0.5-1 mV.

After the amplifiction stage, one partial signal is passed to a discriminator and used for the first-level trigger (FLT) decision. The discriminator threshold can be set independentlly for each channel. In addition, it is possible to enable/disable each single channel for the trigger in order to suppress the influence of bright stars in the field-of-view. The first-level trigger is derived from a four-fold majority coincidence of all pixels within the inner 1.6° area of the camera. Lowering the energy threshold implies lowering the discriminator threshold for the sinple pixels. The minimum of this threshold is given by the random coincidences due to the light of the night sky. The light of the night sky is a very steep function of the threshold and saturates the readout system. In order to reduce the random coincidence rate we can reduce the discriminator pulse width by taking a FLT width $\leq$ 5 ns. We can also reduce the number of four-pixel combinations making use of the topology of images from γ-showers in the camera. For the second level trigger it is planned to implement the nearest-neighbour trigger (e.g. $\geq$ 7 phe in

≥ 4 neighbour pixels in a close packed configuration, that is, each of the triggered pixels has at least 2 triggerd neighbours) on the hardware level using programable gate arrays. Another options is to use an "intelegent" neural network hardware trigger. Such a trigger can help to reject muon and hadron backgrounds, which at pesent is only possible off-line. Since for normal operations a data flow of ~ 1 KHz is expected, a third level trigger based on the arrival time distribution of the Cherenkov photons is being considered.

Whenever the trigger condition is fulfilled, the fast analog signals have to be digitized. As it has been already pointed out, in order to keep the timing information from the camera, a 300 MHz 8-bit FADCs are going to be used in the digitization process. The use of FADC based DAQ, instead of classical gated ADCs (CAMAC, Fastbus) will allow zero deadtime readout by storing the information in an intermediate ring buffer during the 2 level trigger decision. Furthermore, it will reduce the night sky and moon light noise, and will improve the γ/hadron separation by measuring the arrival time distribution of the Chrenkov light in different pixels.

The Cherenkov flashes, particularly those from γ-showers, are very "sharp" in time (usualy with FWHM values of $< 1 - 2$ ns). Depending on the photosensor and preamplifier configuration, the electronics signal will be somewhat widened. Nevertheless, the time can still be reconstructed to the above mentioned precision. In order to make full use ot this low-spread (so that, a fast coincidence time for trigger can be achievable) it is necessary to use an isochronous mirror profile and very fast optical readout elements to avoid any signal distortion during its transportation to the trigger unit (for this purpouse, optical analog fibres is preference over coaxial cables). For signal/noise optimization it is also necessary to use a time recording system matched to the above timing requirements. A modern FADC system can fulfill both requirements, the amplitude and time resolutions. With ≤ 4 ns digitizer time-slices, a resolution below 1 ns can be reached for large pulsed, and about 2-3 ns for small pulses extending barely above noise. Therefore a very good correlation of the different pixel contents with the image an efficient noise reduction should be possible.

Chapter 4

Montecarlo Simulations for the MAGIC Telescope

For carry out our first goal of studying the power of the MAGIC Telescope for the observation of γ-ray pulsars, we firstly have to know the capability of the telescope for the detection of γ showers of low energy, in the energy range of some tens of GeV. For that we will obtain in this chapter the main characteritics that define the performance of a IACT telescope, such as its trigger probabilities and effective collection areas, by means of Monte Carlo simulations. The realization of the simulations involved several steps. First, atmospheric showers are simulated with a specific program designed for such a purpose called *CORSIKA*. Once that we have simulated a library of EASs, the next step is simulate the response of the detector to the Cherenkov light produced in the showers, by means of the simulation of the reflexion of the cherenkov photons on the telescope's reflector and then by the simulation of the formation of the images on the camera.

In this chapter we will simulate γ, electron and proton induced showers. Firstly, we will obtain the MAGIC trigger efficiency and effective collection area for γs. With the effective collection area for γs we will be able to obtain in next chapter the MAGIC detection rates for the EGRET pulsars. We will also need to evaluate the background rate for MAGIC since for the calculation of the observation times that MAGIC will require for the detection of the EGRET pulsars we will need this value. For that, we will study the electron and proton background at low energies. The result obtained for electrons are mainly to be used in the last chapter of this work.

We are going to divide this chapter in three main sections: a first section in which we will discuss about the software and the procedure followed for the simulation of the atmospheric showers and of the detector. A second part in which we explain how to calculate the trigger efficiencies, effective collection areas and detection rates of an IACT telescope. And finally we will show the results of our simulation for γs, electrons and protons.

4.1 Extensive Air Showers Simulation

The simulation of atmospheric showers is a complex task which can only be achieved by detailed Monte Carlo programs. In the implementation of such a kind of programs, one not only have to simulate all the physical processes involved in the development of the showers, but also the environmental parameters, such as the atmosphere and the geomagnetic field. We have already seen in Chapter 2 the main processes that take place in an EAS, so it is easy to see the difficulty in modelling such interactions for all the secondary particles generated in an EAS. In addition, we have the problem that the knowledge of high energy interactions is still incomplete in important features.

4.1.1 The CORSIKA program

The program that we have chosen for the simulation of the EASs is the CORSIKA program, version 5.20. CORSIKA (COsmic Ray SImulations for KAscade[1]) is a detailed Monte Carlo program to study the evolution and properties of extensive air showers in the atmosphere, initiated by photons, protons, nuclei, or any other particle. The program inplements detailed subroutines which simulates the transport of particles through the atmosphere and their decays and interactions with air targets, including also a model of the atmosphere and taking into account the Earth's magenetic field. All particles are tracked along their trajectories and the output of the program gives type, energy, location, direction and arrival times of all secondary particles that are created in an air shower and pass a selected observation level.

Without entering in detail in the internal working of the program we would like to comment some general aspects of it in order to know what are we working with, putting special emphasis in the generation of the Cherenkov light.

The CORSIKA program can be basically divided into 4 parts. A first part which performs the tracking of the particles, taking into account ionization energy loss and deflection by multiple scattering and by the Earth's magnetic field. The second part simulates the processes which take place in the hadronic showers, that is to say, the hadronic interactions of nuclei and hadrons with the air nuclei at high and low energies, and the decay of the unstable particles. A third part describes the electromagnetic interactions of electrons, positrons, and photons of the electromagnetic showers and subsowers. And a fourth part treating the generation of the Cherenkov light. For the simulation of the hadronic and electromagnetic interactions, CORSIKA implements several models that may be activated optionally by the user with varying precision of the simulation and consumption of computer time.

[1] CORSIKA was originally developed to perform simulations for the KASCADE experiment at Karlsruhe in Germany, which measures the elemental composition of the primary cosmic radiation in the energy range $3 \cdot 10^{14}$ to $1 \cdot 10^{17}$ eV.

Particle tracking through the atmosphere

For propagating particles between two interactions points their space and time coordinates as well as their energy have to be updated, by taking into account the following processes.

- *Ionization energy loss*: Charged particles lose energy by ionization whereas neutral particles proceed without energy loss. The ionization energy loss is computed along the particle trajectory with the Bethe-Bloch stopping power formula.

- *Coulomb multiple scattering*: Charged particles are scattered in the electric Coulomb field of a nuclei in the air. As these nuclei are generally more massive than the scattered particles, the direction of flight might be altered, but not the energy. In CORSIKA the process of Coulomb multiple scattering is considered only for muons and only once for each tracking step in the middle of the tracking distance.

- *Deflection in the Earth's magnetic field:* All charge particle with momentum $\vec{p}$ suffers a deflection which points to the direction normal to the plane spanned by the magnetic field $\vec{B}$ and $\vec{p}$.

The atmosphere adopted in CORSIKA consist of N_2, O_2 and Ar with the volume fractions of 78.1%, 21.0% and 0.9%. The density variation of the atmosphere with altitude is modeled by 5 layers and a flat atmosphere is considered, understanding by flat atmosphere a series of parallel layers not taking into account the Earth's shape. This is an important fact that has to be taken into account if one wants to generate showers at high zenith angle where this approximation is no valid.

Hadronic interaction models and Decay of unstable particles

The distance a particle travels before it undergoes its next interaction or decay is determined by the cross section for a hadronic reaction together with the atmospheric density distribution along the flight path, and the probability to decay. A decay length and an interaction length are determined independently at random and the shorter one is taken as the actual path length. By this procedure it is also decided whether a particle decay or interacts.

Hadronic interactions are simulated within CORSIKA by several alternating models depending on the energy.

- *High energy interactions:* For the hadronic interactions of nuclei and hadrons with the air nuclei at energies above $\sim$ 80 GeV the following models are used: the VENUS model (Very Energetic Nuclear Scattering) [21] for simulation of ultra relativistic heavy ion collisions with detailed simulation of creation, interaction, and fragmentation of color strings; the quark-gluon-string model QGSJET [22]; the Dual Parton Model DPMJET [23] or the

QCD minijet model SIBYLL [24, 25]. As an alternative model of the interactions between hadrons and nuclei at high energies, a phenomenological simple Monte Carlo generator inspired by the Dual Parton Model, called HPDM [26], may be used. These high energy models only work for energies above 80 GeV because below this energies the generation of strange baryons takes place, and a model for low energy interactions is needed.

- *Low energy interactions.* The low energy hadronic interactions at energies below $\sim$ 80 GeV may be simulated either with the GHEISHA code [27], that is a well approved detector Monte Carlo program in the energy region up to some hundred GeV, or by very simple routines, but faster, based on the ISOBAR and fireball models [28].

Most of the particles produced in high energy interactions are unstable and may decay into other stable or unstable particles. Neutral pions π° and η mesons as well as all resonance states have such a short life time that interactions is negligible before the decay. Muons are prevented from penetrating the complete atmosphere by decay only. Neutrons are treated as stable particles due to their long life time. For all the other unstable particles there is a competition between interaction and decay processes and the decision is taken when calculating the actual mean free path.

Electromagnetic interaction models

The interactions of electrons and photons is treated with the EGS4 (Electron Gamma Shower System version 4) code [29], which performs a full Monte Carlo simulation of the electromagnetic component of the showers. For electrons or positrons it treats bremsstrahlung and multiple scattering, Bhabha and Moller scattering, and annihilation. γ-rays may undergo Compton scaterring, electron-pair production and photoelectric reaction. The photoproduction of muon pairs and the photonuclear reaction with the protons and neutrons of atmospheric nuclei are also taken into account. An alternative way of treating the electromagnetic component is to use the improved form of the analytical NKG (Nishimura Kamata Greisen) [30] formula. It is faster but less accurate, and coordinates of electromagnetic particles cannot be obtained, but only total electron numbers at various atmospheric depths together with some parameters that give information above the general development of the electromagnetic component of the shower.

Simulation of the Cherenkov Light in CORSIKA

Based on a program extension made by HEGRA collaborators [31] the simulation of the Cherenkov radiation by mainly electron (but also by muons and charged hadrons) is implemented in the CORSIKA code. We have seen in Chapter 2 how and under what conditions this radiation is produced. In the program the condition $v/c > n$ is examined for every tracking step of a charged particle, where the refractive index n is approximated by the local density $\rho(h)$ (in g/cm^3): $n = 1 + 0.000283 \cdot (\rho(h)/\rho(0))$, neglecting the wavelength dependence of n. If this condition is fulfilled, then the number N_c of photons which are emitted per path length s at an angle θ_c is calculated as:

$$\frac{dN_c}{ds} = 2\pi\alpha \int \frac{sin^2\theta_c}{\lambda^2} d\lambda \tag{4.1}$$

where the integral extends over the wavelength band, within which the Cherenkov detector is sensitive; α is the fine structure constant, and the angle θ_c relative to the charged particle direction is given by: $\theta_c = \arccos 1/(\beta \cdot n)$

The emission of Cherenkov photons is treated in the following way: once that the total number of emitted photons N_c have been calculated for a given tracking step, this step is subdivided into smaller sub-steps, such that the number of Chrenkov photons emitted per sub-step is less than a fixed predefined bunch size. In such a sub-step all the photons are sent in a compact bunch along a straight line, defined by the emission angle θ_c and a random value for the azimuthal angle around this direction. This photon bunch is treated as a whole rather than each single Cherenkov photon, thus reducing the computational effort and time considerably.

The Cherenkov photons are considered within a wavelength band which may be specified by the user. The atmospheric absorption of the Cherenkov photons is not taken into account, but by writing the original height of each photon bunch onto the Cherenkov output, the absorption may be introduced later when analyzing the output data. Only Cherenkov photons arriving at the observation level are recorded in the output file. In the output file, for each bunch are recorded the number of Cherenkov photons, the x and y position coordinates at the observation level, direction cosines u and v, arrival time, and height of production above sea level.

4.1.2 Running CORSIKA

In CORSIKA, the simulation of air showers is steered by parameters that have to be given by the user in an input file or *steering card*. This input file serve to adequate the simulation to our necessities. Among other options, we have to specify in the input file the kind of primary particle that we want to simulate and its initial energy and zenith angle, and other options with do not depend on the kind of primary particle such as the location of our detector, the model for the hadronic and electromagnetic interactions that we want to use, etc.

The following table shows the values choosen for the main parameters of the CORSIKA program used in the generation of both γs and background showers.

Parameter	**Value**	**Comment**
OBSLEV	2200.E2	This parameter specify the observation level above sea level (in m). As MAGIC will be place at 2200 m, we set this parameter to that valuee.
MAGNET	29.5 23.0	These are the values of the horizontal (to the north direction) and vertical (downwards) component of the Earth's magnetic field in μT at Central Europe.
VENUS	T	By setting this flag to True we select the VENUS and GHEISA hadronic interaction models.
ELMFLG	F T	These parameters serve to choose the electromagnetic model. The two flags active/desactive the NKG and EGS4 model respectively.
STEPFC	1	Factor by which the multiple scattering length for $e^{\pm}$ in EGS4 simulations is elongated. Although the default value is 10 we thought that a more extended treatment of the multiple scattering of $e^{\pm}$ by a reduction of this factor may be necessary to reproduce experimental data in experiments which are sensitive to the $e^{\pm}$ flight direction, such as Cherenkov detection with primary energy in the GeV range.
CWAVLG	290. 600.	This specify the wavelength band within Cherenkov photons are considered.
CERSIZ	1	Defines the maximal bunch size of Cherenko photons that are treated together. Setting this value to 1, we have a bunch per photon, treating in that way each photon individually, obtaining a bigger sample of photons.
CSCAT	1 0 25000	This factor allows the use of a shower multiple times and to fix the shower core impact point (in cm). We only used each shower event once and a random core in the range $x_c = 0$ and $-250 \leq y_c \leq 250$ (in m).
ECUTS	.3 .3 .02 .02	This four values are the kinetic energy cut-off (in GeV) for hadrons (energy per nucleon), muons, $e^{\pm}$ and photons respectively. Since we are interested in Cherenkov radiation, only $e^{\pm}$ with energies higher than $\sim$ 21 MeV interest us. For hadrons an muons the same argument is valid, but since the mass of the muon is around $\sim$ 200 times the $e^{\pm}$ mass, we select an energy cut of $\sim$4 GeV for muons. For the hadrons, the lightest ones are the $\pi^{\pm}$ which have a mass around 200 times higher than the $e^{\pm}$, so we set the cut at $\sim$3 GeV.

Table 4.1: *Input parameters used in our simulations.*

4.2 Detector Simulation

Once that we have generated atmospheric showers, the next step is simulate how these showers would be recorded by the detector. The simulation of the detector is one of the critical points of every work that studies EASs through the simulation procedure. The results of the work depend very strongly on the parameters that define the simulated telescope and camera so these parameters have to be chosen very carefully. In our simulation we tried to be as close as possible to the real situation so many parameters are needed in order to achieve such an order of realism. Simulation parameters go from the mirror's reflectivity to the QE of the PMTs going through the area of the telescope, ADC gate, etc.

For the simulation of the telescope we are going to use two programs developed by the MAGIC collaboration. The first one, called just *reflector*, takes the output of CORSIKA and simulates the reflector of the telescope translating the photons from the ground to the pixelated camera. This program previously calculate the atmospheric extintion suffered by the Cherenkov light. The output of this first program is taken by a second program, called *camera*, that will obtain the Hillas image parameters using the second moment fits already described in this work. This second program also simulates the LONS (Light Of the Night Sky), in order to achieve a more realistic situation. In both programs we will include the technicals characteristic of the MAGIC telescope described in Chapter 3.

4.2.1 Simulation of the Reflector

We have already said that the CORSIKA program doesn't calculate neither the atmospheric extintion nor the scattering (such as Rayleigh and Mie scattering) suffered by the Cherenkov photons as they travel through the atmosphere, since the are emitted until the reach the ground. Therefore, the first step that the reflector program has to perform is the simulation of these phenomena, which are going to cause a reduction on the number of Cherenkov photons which reach the ground (specially for low energy showers) and a change in theirs wavelength.

Once that the atmospheric extintion and the scattering have been taken into account, the next step is the simulation of the reflexion of the Cherenkov photons on the detector's mirrors and the calculation of the points that the reflected photons reach in the focal plane. This part involves both the effect of the reflectivity of the mirrors and the use of the ray tracing technique, and for that, the thecnicals characteristics of the MAGIC telescope was implemented, like a mirror reflecitivity of an 85% and the exact position and orientation of each single mirror element (also the planned 5 mm gaps between neighbouring mirrors was taken into acount). The Cherenkov photons from showers which hit the reflector are traced through the atmosphere and the coordinates of reflected photons in the focal plane are obtained fron the ray tracing technique. In this way realistic aberrations of the tessellated reflector of MAGIC Telescope are simulated. In the simulation of the camera, we will obtain at which camera pixel corresponds this coordenates.

4.2.2 Simulation of the Camera

The simulation of the camera is obviously the more critical step in all the process. Besides implements the characteristics of the camera, such as the QE of the PMT's, we have to choose carefully the parameters that define the trigger conditions, like the threshold, the number of next neighbours and the camera trigger radius. The values that we use for this parameters are going to be of an overwhelming important in all our results. We have to choose the optimal values which allow us push down the accidental trigger due to the night sky background as low as possible, but retaining the bigger number of gammas posible. The quest for the optimal trigger condition is quite difficult, and we will discuss about it later.

The simulation of the camera includes the obtention of the number of photons which reach each photomultiplier and the simulation of the camera's electronics which includes taking into account the effect of the QE, the trigger loggic and the FADC's. Also the LONS has to be taking into account. The output of the program are camera pixelated images with theirs corresponding Hillas parameters. Lets see briefly each of these steps.

1. The first step is quite simple. The output of the *reflector* program give us the coordinates of each reflected photon in the focal plane. Thus, with the coordinates of this point and taking into account the number of pixels of the MAGIC camera, their size and location, we obtain the number of the pixel at which each photon arrives. Although, as we saw in § 3.3.1, the camera will be composed of two regions of differents PMTs, for the sake of simplicity, we have considered that all the camera is composed of the same PMTs, the ones of the central region of 10° size (the 9116A bialkali PMTs).

2. Once that we have the number of photons that arrive to each photomultiplier, the program simulates the QE of the PMTs and the camera electronic (described in § 3.3.3) in order to obtain the pixelates images for each shower, as they would be seen by the real telescope. The QE as a function of the wavelength that we have use for the PMTs is shown in Fig. 4.1. It was obtained by measuring the QE of the PMTs at different wavelength. When a photon of a given wavelength, different from the measured points, hit a PMT, the value of QE is taken by a third order extrapolation between the closest measured points. A 90% light collection efficiency was taken for the light guides which are to be attached to the PMT's and the collection efficiency for the photoelectrons fron the photo cathode was also assumed to 90%.

3. Lately, we simulate the trigger logic. For each pixelated image, the program calculate if it pass the trigger condition. If so, in the program output file that shower is marked as a triggered one. This allow us to have in the

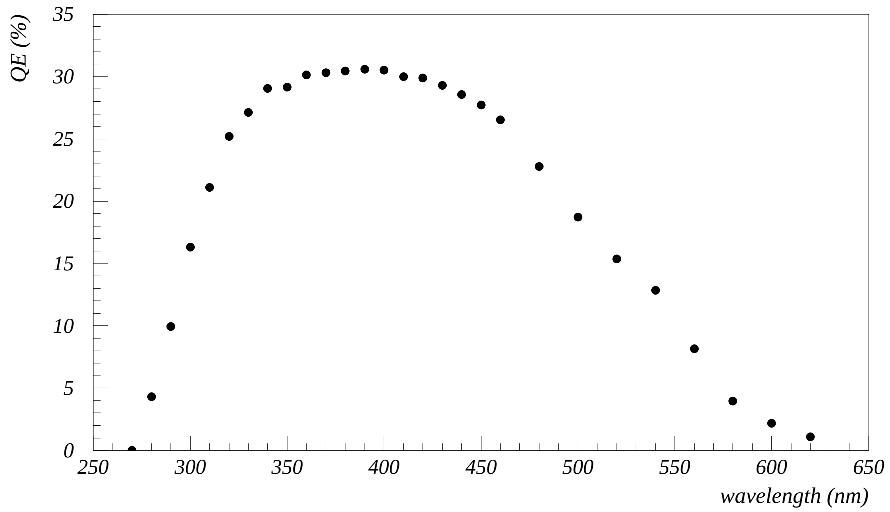

Figure 4.1: *Quatum efficiency for the MAGIC's PMTs.*

output file those showers with trigger the telescope together with those which don't trigger in order to study the differences between both of them.

There are two critical factors in the simulation of the camera and the results obtained will depend very strongly on those factors. One is the trigger condition of the telescope and the other one is the 'tail cut' applied for the image analysis. Next, we will discuss about the simulation of the light of the night sky and about the choice of the trigger condition and tail cut.

The Light of the Night Sky

As we have already said in §1.2.1, the telescope is constantely exposed to the high rate of the LONS. The LONS is one of the most important factors is limiting the energy threshold of atmospheric Cherenkov telescopes. It causes accidentral triggers and also contaminates the γ images close to the energy threshold.

The intensity of the diffuse NSB was masured at the site of the "El Roque de los Muchachos" observatory on the Canary Island of La Palma [32], which provides one of the best sky in the world for astronomical observations. This measurement was performed using the single photo-electron counting technique in the wavelength range of 300-600 nm. This spectral range was chosen since the PMT with bialkali photocathode are sensible to light in that range. We use here the result for a narrow angle detector (angular acceptance $\leq 1°$) since this will be the case of the finely pixelized MAGIC Telescope. Therefore, according to this measurement, we took for our studies the NSB photon flux to be:

$$\Phi_{LONS} = (1.7 \pm 0.4) \cdot 10^{12} ph/m^2 \cdot sr \cdot s \tag{4.2}$$

over the spectral range between 300-600 nm

With this value for the flux of the LONS and the MAGIC characteristics, namely, 236 m^2 of mirror area, 0.05° pixel radius[2] and 90% mirror reflectivity we get the following single-pixel photon rate R_{pixel} due to the night sky background light.

$$R_{pixel} = 863.8 \text{ MHz/pixel}$$

As can be easily seen this is a very high value for the rate, which leads to impose trigger conditions.

Taking into account this value for the LONS photon rate in each pixel, the 30% QE of the PMTs and the integration time of the FADCs gate, we estimate an mean number of photoelectrons[3] per pixel due to the LONS contribuition of $\sim$ **3** ph.e./pixel per measured event. According with this, we take into account the LONS by generating Poisson randomly distributed events with a expected number of 3 ph.e. In generating images of showers the Poisson fluctuations of this value are added to the genuine charges measured in pixels. In the transformation from signal photons to ph.e.s first the mean number of ph.e.s is determined by taking into account the QE(λ) and then the real measured charge is defined by the fluctuations from the mean.

The Trigger Logic

Due to the LONS the detector is receiving photons continuously so if no trigger condition is set then, every time a photon reaches the photomultiplier the system would be triggered. This trigger caused by spurious signals is called accidental trigger. This situation has to be avoid, so in order to suppress the accidental triggers produced by background signal, a trigger condition has to be set. First, lets see how the trigger works in an IACT. When a signal arrives to one of the PMT a certain current is originated at the anode. After going through the amplifier the signal is divided in two, one going via delay cable to the ADC and the other to the discriminator. A discriminator is a device which responds only to input signals with a pulse height greater than a certain threshold value (in mV). If the criterion is satisfied, the discriminator responds by using a standard logic signal, if not, no response is made. If the signal passes the discriminator the signal is sent to the input of a coincidence unit which provides an output signal if N out of M inputs are coincident in time. In this case the trigger signal opens the gates for the ADCs, latches the rubidium clock bit pattern and generates a

[2]We consider, for simplicity, that all the pixels have the same size of 0.1°.

[3]A PMT consists of a cathode made of photosensitive material followed by an electron collection system, a set of what are called dynodes, and finally an anode from which the final signal can be taken. The conversion factor between arriving photons at the cathode and electrons produced at the cathode is the quantum efficiency QE of the PMT. The photoelectrons (ph.e.s) are the electrons produced in the PMT's cathode with the arrival of one photon.

computer interrupt to start the readout cycle. There are several trigger levels and every level gives a different trigger rate. A first level is to ask for a pixel threshold q_0 (q_0 is the value in ph.e. set in mV at the discriminator) in order to suppress the accidental trigger rate. An important fact is that the pixel trigger threshold q_0, limits the minimum energy of the shower that we are able to detect and thus the energy threshold of the telescope, so q_0 is a very critical value that has to be chosen with care. A second trigger level would be to ask for N pixels to fire in coincidence within a time window. And finally we could impose that not only they have to be fired in coincidence but they have to be next neighbors. The important question is set the optimal values for discriminator threshold $\mathrm{q_0}$[4] and the number of next neighbours (NN) for killing the accidental trigger due to this high diffuse NSB succesfully, but without supress too much γ-rays events (specially a low energies).

For our simulations we will use the following trigger condition:"any 4 neighbouring pixels in a close-packed configuration above the pre-set threshold of 7 ph.e.s". The restrictive trigger condition of requiring a close-packed pixel configuration yields a strong suppression of the accidental triggers due to LONS and provides a very low trigger threshold. It allows one to trigger with high efficiency on γs while providing a much lower efficiency for hadrons due to the more diffuse shape of their images. Therefore we expect that this trigger condition will help to trigger readily on sub-100 GeV γs, while only hadrons mostly with energies above 100 GeV will produce enough light to initiate triggers.

The camera trigger radius

The camera trigger radius must provide high trigger efficiency for γs for the entire extended VHE energy range, simultanesouly triggers due to isotropic bakgrounds have to be minimized. To achive the highest γ rate the optimization of imaging camera trigger diameter is of key importance, because it allows one to considerably reduce the trigger rate due to different isotropic backgrounds, e.g. that of protons and elecrons.

Because sub-100 GeV γ showers develop higher in the atmosphere the telescope *see* them at smaller angles with respect to the source direction, which means that shower images are closer to the source position in the camera plane, that is, to the center of the camera. Thereby, for our work only those pixels which are within 0.8° radius from the camera centre were "set" into the trigger. With a larger trigger radius one would detect γ-rays over the entire energy and impact parameter ranges, increasing slightly the trigger rate. However the proton trigger rate would increase much more quickly with the trigger radius, since the trigger rate due to any isotropic emission is proportional to the camera acceptance solid angle.

[4] This value is set at the discriminator in mV, but it is equivalent to setting a condition in the number q_0 of photoelectrons produced at the cathode of the photomultiplier.

The tail cut choice

The measured Cherenkov light flashes contain the background light in each camera pixel. The influence of the background light is very strong for the pixels being at the *tail* of the Cherenkov light images, causing that pixels which have been fired by the LONS can be mistaken for pixels belonging to the image. This will lead to a wrong estimation of the image parameters. For avoiding this, what one usually does is to define the picure pixels in which Cherenkov light from the air shower dominates above the background light, as those which have a number of ph.e.s above a certain tail cut. And then one selects only those boundary pixels which have at least one neighbour picture pixel. With this tail-cut we eliminate pixels from the camera that do not belong to the image but that have big influence when obtaining the image parameters. For our studies, we have chose a tail cut of "10 ph.e.s".

4.3 How to Calculate the Collection Areas and Detection Rates

Assume we detect a shower of a given energy with impact parameter equals to zero. Next we can ask ourselves how far can the impact point be from the telescope in order to detect it. This way we can evaluate for a given energy the probability of detecting a shower at different core distances. For a given energy this probability depends only on the impact parameter, and gives us an idea of the dependance of the detection of γ-ray showers with the distance of the shower core from the telescope. Therefore, for a point source of primary γ-rays, the probability P that a shower triggers the telescope (which is pointed towards the source) depends on the energy of the primary γ and also on the impact parameter r of the shower with respect to the telescope. The effective collection area for γ-ray induced air showers is a energy-dependent magnitude which characterize the telescope capabilities for the detection of γ-rays. It is evaluated as:

$$S_\gamma(E) = 2\,\pi \int_0^\infty P_\gamma(E,r) \cdot r\,dr \tag{4.3}$$

where $P_\gamma(E,r)$ is the trigger efficiency or probability of detecting γ-ray air showers of primary energy E at different distances. For a given γ-ray source with differential flux dF_γ/dE, its detection or trigger rate is determined from the collection area as:

$$R_\gamma = \int_0^\infty \frac{dN_\gamma}{dE} S_\gamma(E) \cdot dE \tag{4.4}$$

The situation is different for the background of hadronic induced shower. For the isotropic cosmic ray background the detection probability depends in addition on the shower angle of incidence δ with respect to the axis of the telescope,

$P = P_{cr}(E, r, \delta)$. The collection area is then written as:

$$S_{cr}(E) = 4\pi \int_0^{\pi/2} sin(\delta) \cdot d\delta \cdot \int_0^{\infty} P_{cr}(E, r, \delta) \cdot rdr \tag{4.5}$$

Note that the S_{cr} has the meaning of an effective area times solid angle. Given the corresponding background flux, $dF_{cr}/dEd\Omega$, the detection rate is calculated as:

$$R_{cr} = \int_0^{\infty} \frac{dN_{cr}}{dEd\Omega} \cdot S_{cr}(E) \cdot dE \tag{4.6}$$

Method used in our simulations

In our simulation we evaluate the probability of detecting an event just by comparing the number of showers that fulfill the trigger condition against the total number of shower generated:

$$P_{\gamma/CR}(E, r, \delta) = \frac{\text{Number of triggered events}}{\text{Total number of events}} \tag{4.7}$$

Once we have this probability we evaluate the integral of the effective area at a given energy E numerically, as the sum of the products of the trigger probability at the distante r by its corresponding area of a ring of width w centered at r, from $r = 0$ up to the maximum value of the impact parameter generated:

$$S(E) = \sum_{r_i=0}^{r_{max}} P(E, r_i) \cdot \pi \left[(r_i - w/2)^2 - (r_i + w/2)^2 \right] \tag{4.8}$$

4.4 Generation of the Monte Carlo Library

For evaluating the main characteristics of the MAGIC telescope, such as trigger probabilities, effective collection areas and detection rates, we have used the program CORSIKA described above for generating our Monte Carlo library of atmospheric showers. The events generated have been γ events and proton events, and for that the following trigger condition have been used:

"any 4 neighbouring pixels above the threshold of 7 ph.e.s within 0.8° from the camera centre"

together with a tail cut of 10 ph.e.s. In addition, environmetal parameters were chosen to represent the conditions at La Palma island, as it was shown in table 4.1.

For our work we have simulated more than $1.3 \cdot 10^6$ γ-ray showers in the energy range between 5 and 200 GeV. The number of events per energy bin follow a power law given by: $dN/dE \propto E^{-1.5}$. The showers were generated at a zenith angle between 0° and 15°, and all Cherenkov photons at ground were collected if they fall within a area of 250 m radii centered on the core[5], that is, the impact parameter range was 0-250 m. Only those Cherenkov photons with a wavelenght in the range of 290-600 nm were recorded, recording the direction and the wavelenght of every photon which hit the detector. Taking into account the high trigger efficiency for γ-rays detected by the MAGIC Telescope, this is more than enough, providing a very good statistics for Monte Carlo studies.

IACT's have to deal with a background of electron- and hadron-initiated atmospheric showers. At very low energies below 50 GeV hadrons rarely generate enough Cherenkov light to trigger the telescope. As we will see in our simulations, its contribution to the background is negligible below 30 GeV. In turn, cosmic electrons will give rise to showers which are practically indistinguishable from γ-induced ones and thus can not be eliminated using traditional γ/hadron discrimination methods. They are isotropic and can be suppressed by means of an improved angular resolution when the telescope searches for point sources, but they constitute an irreducible background in extended source searches and diffuse γ flux estimations.

For the simulation of the cosmic electron background we have maded the assumptions that electron-initiated showers behave exactly like γ showers (as done in [34]). That is, we have use the generated γ library describe above, but taking into account that electrons arrive isotroplically in the camera. For that, the shower axis was generated parallel to the telescope pointing direction ("on-axis"), but also with a certain angle δ with respect to this direction ("off-axis") in order to characterize all posible incident directions. In particular values of δ between $0°$ and $1.5°$ were simulated.

The hadron events generated are protons, which for the energies involved in our work represent about 43% in the chemical composition of hadrons at 1 TeV [33]. The components in cosmic rays that are heavier than protons contribute about 25% to the total rate measured by Cherenkov telescopes. The proton showers were simulated within an solid angle range of $\pm 5°$ with respect to the axis of the telescope, and for an impact parameter between 0 and 500 m. The number of simulated proton showers is $\sim 3 \cdot 10^5$, with energies between 5 and 1000 GeV according to a differential energy spectrum $\propto E^{-1.5}$. For the simulation of the proton events we have taken into account that hadronic showers produce less Cherenkov photons light than γ showers of the same energy, in order to have approximately the same light intensity per unit of area as for the γ events. As we have seen in §2.3.1, this is due to the fact that hadronic showers should produce less light because not all of the primary energy goes into the electromagnetic

[5]Two things have been taken into account here. One the drop of the Cherenkov light pool around 150 meters and the other one the limited field of view of the detector. The field of view limits the detector in a way that light is collected only from within a small angular radius α from the axis. From geometry, if a shower falls, say 100 m from the telescope, only the part above an altitude of $100/\sin(\alpha) \sim 12$ Km, is seen.

cascade, from which most of the fraction of Cherenkov light produced in an EAS comes. Therefore, one has to simulate many tens of thousand events for energies below 100 GeV, because the protons are very strongly rejected already at the trigger level. Thereby, to increase the sample statistics we have use the same proton-induced shower 10 times in the *reflector* program, each time with a different shower angle of incidence δ with respect to the axis of the telescope.

The reason of simulating proton showers within an angular acceptance that is much wider ($\pm 5°$) than the trigger radius of the camera ($0.8°$) is twofold:

1. One takes into account triggers due to inclined showers, the axes of which lie outside of the camera acceptance, but whose light, due to the large multiple scattering angle, can trigger the camera.

2. One takes into account triggers due to Cherenkov light emission from charged single particles coming fron air showers, e.g. from muons. The later can sometimes have non-negligible angles with respect to the shower axes and though the showers itself can be outside of the camera acceptance, the muon can be in the filed of view and Cherenkov light from it can initiate a trigger.

Note that a telescope with a relatively large field-of-view and with very high light sensitivity, in the case of triggers from charged single particles, as a general rule, should also see at least part of the tracks of the parent shower.

4.5 Results of the Simulations

Below we present the results of the simulation for the MAGIC Telescope with the operational setup described above.

4.5.1 MAGIC Performance for γ-ray Events

For γ events, our results are the following.

Trigger Probabilities for γ-rays

Figure 4.2 shows the trigger probabilities for γs of different energies versus the impact parameter. On average 10 GeV γs trigger the telescope with a probability of only $\sim 0.2\%$ up to impact parameter of about 120 m, i.e. only one γ-induced shower in 500 with an energy of 10 GeV initiates a trigger. 20 GeV γs trigger with a probability of 4%, which increase to 25% for 40 GeV. The 60 GeV γs trigger with a probbility of 60% up to the same distance and the 80 GeV γs trigger with a probability of 85%. The 100 GeV γs trigger with a probbility of 95% above which the trigger probability reaches the plateau level of almost 100%.

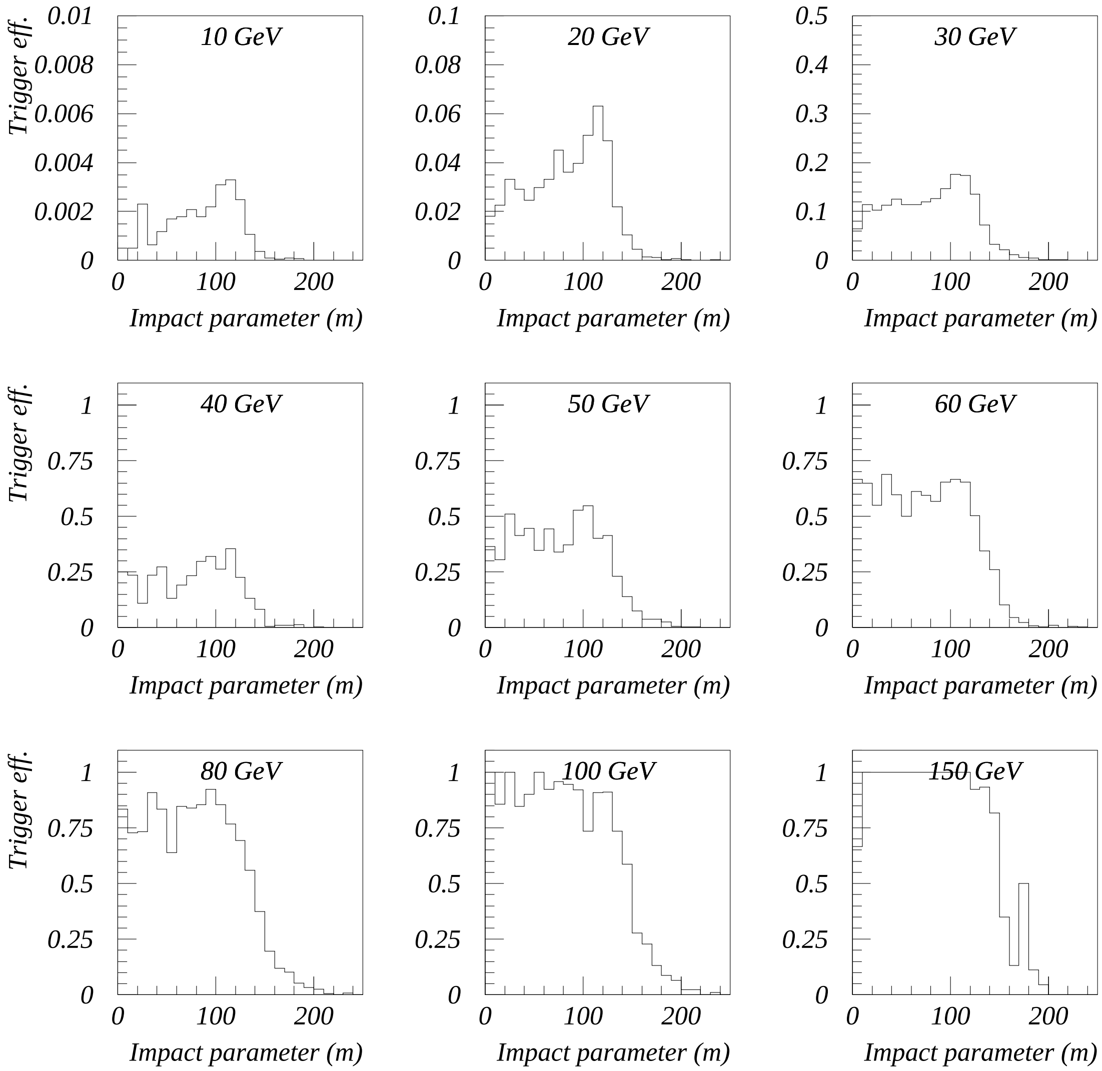

Figure 4.2: *Trigger probability for γ-rays of different energies versus the impact parameter. The trigger condition "any 4 neighbouring pixels above the threshold of 7 ph.e.s" has been applied.*

Effective Collection Area for γ-rays

Figure 4.3 shows the MAGIC raw collection area (i.e. with no γ selection cuts) for γ primaries. The collection area was calculated using the method described in § 4.3. A trigger condition of four next-neighbour pixels with at least 7 photo-electrons in a trigger region of 0.8° was adopted.

As we see in the figure, at energies around 10 GeV the collection area is already larger than 100 m^2, which is already orders of magnitude larger than the corresponding collection area of EGRET. So regarding with pulsar observations, MAGIC will have the capability to trigger 10 GeV γ-rays, and with a collection

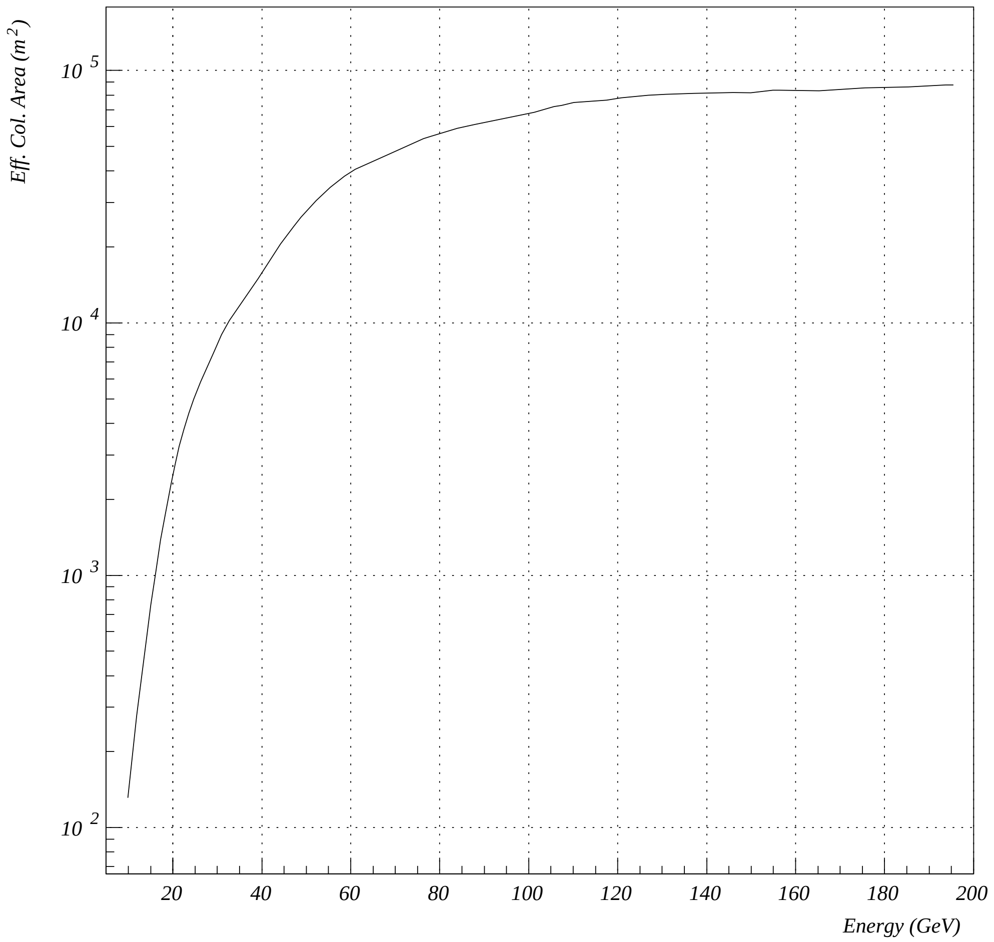

Figure 4.3: *Effective collection area after triggering for γ-rays (of energies between 5 and 200 GeV).*

area which increases rapidly with increasing energy, MAGIC should be able to overlap with EGRET in the 10-30 GeV range and capture pulsed γ-rays in this range.

Image parameters for γ-induced showers

Because sub-100 GeV γ showers develop higher in the atmosphere the telescope *see* them at smaller angles with respect to the source direction, and therefore, the images measured are more round. It is expected that this causes that the accuracy of determining both the orientation and the shape parameters deteriorates for low energy γ showers.

Fig. 4.4 shows the distributions of the Alpha parameter for γs of different energies. One can see that the width of the Alpha distributions (at half-maximum level) is larger for lower energies. Its value is about 5° for energies above 200

GeV, becoming 10° for energies of 60 GeV and about 20° for energies of 10 GeV, confirming the above mentioned expectation. It is interesting to note that although γ-rays from a point source enter the atmosphere parallel to the axis of the telescope, our simulations of very low energy showers reveal that they sometimes develop showers, whose axes make non-zero angles with that of the telescope. A possible explanation for this could be that the direction of shower development begins to fluctuate already during the first few interactions.

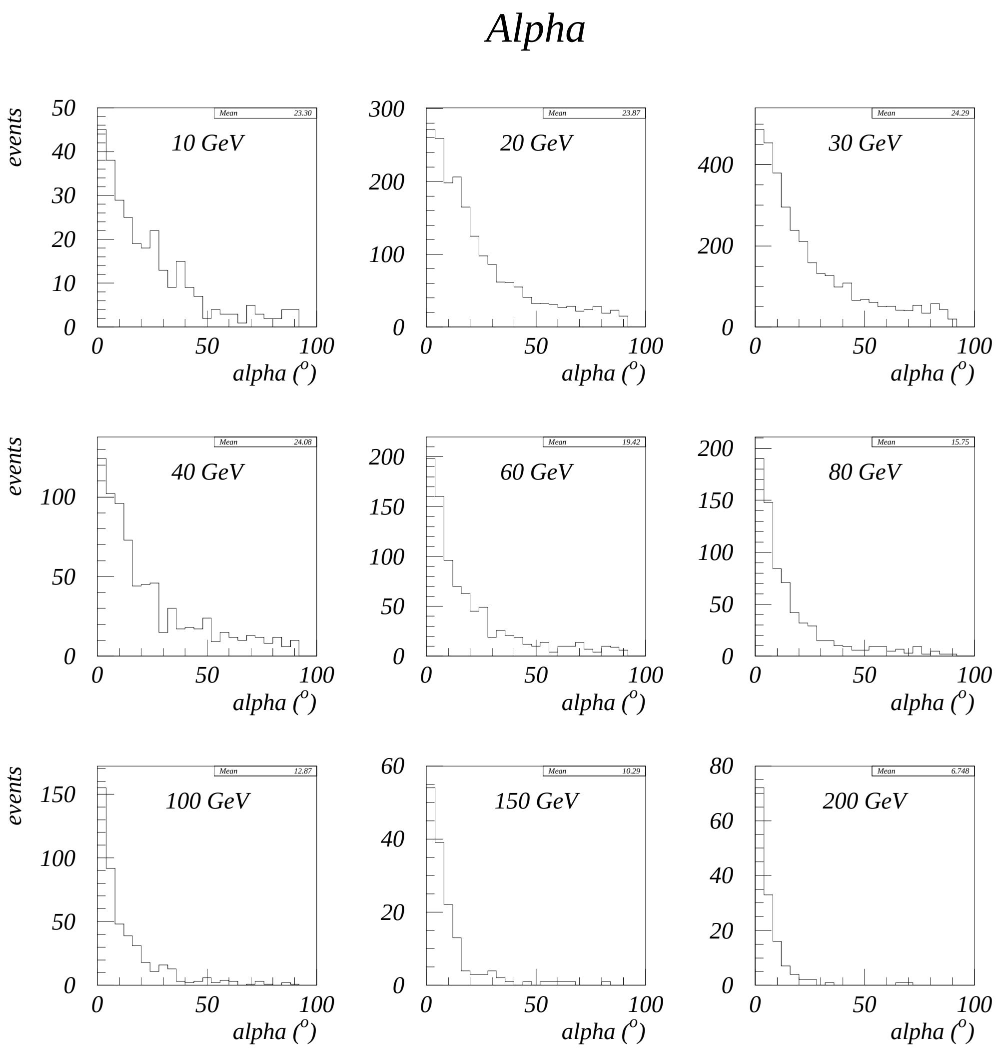

Figure 4.4: *The Alpha image parameter distribution for γ-rays of different energies (from 10 to 200 GeV). A trigger condition of four next-neighbour pixels with at least 7 photoelectrons in a trigger region of* 0.8° *was adopted.*

In Fig. 4.5 we see that the average value of the distance parameter is almost the same for all the energies between 10 and 100 GeV, with mean value of about

0.5°, increasing at energies above 100 GeV, up to reach a value of about 0.7 at 200 GeV.

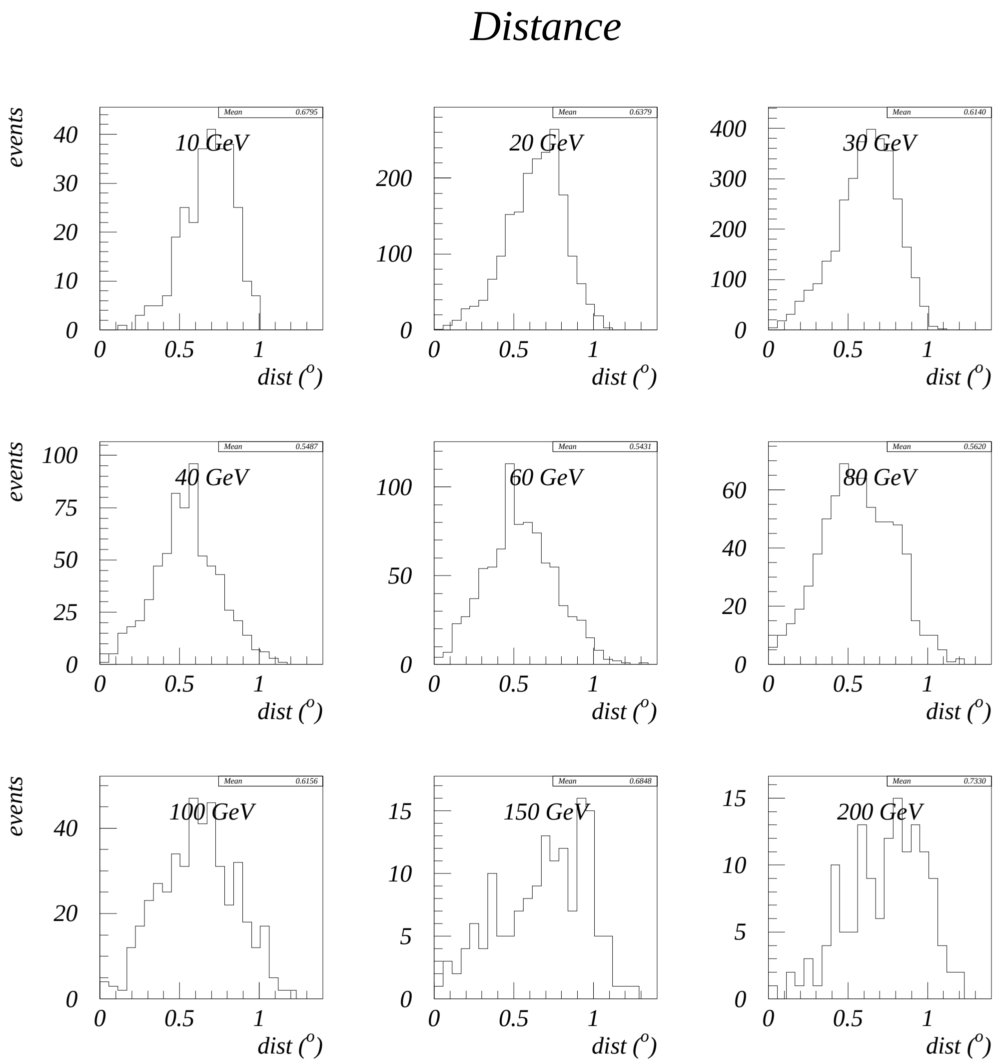

Figure 4.5: *The Distance distribution for γ images of different energies (from 10 to 200 GeV). A trigger condition of four next-neighbour pixels with at least 7 photoelectrons in a trigger region of* 0.8° *was adopted.*

In Figs. 4.6-4.7 we can see the tendency for the mean values of the images parmeters Width and Length to increase gradually with increasing energy. On average the 40 GeV showers have Width's of 0.03°, which increase to 0.05° for 100 GeV showers and to 0.07° for 200 GeV showers. Similarly, the Length of 40 GeV showers is about $0.10^\circ - 0.15^\circ$, and this increases to 0.2° for 200 GeV.

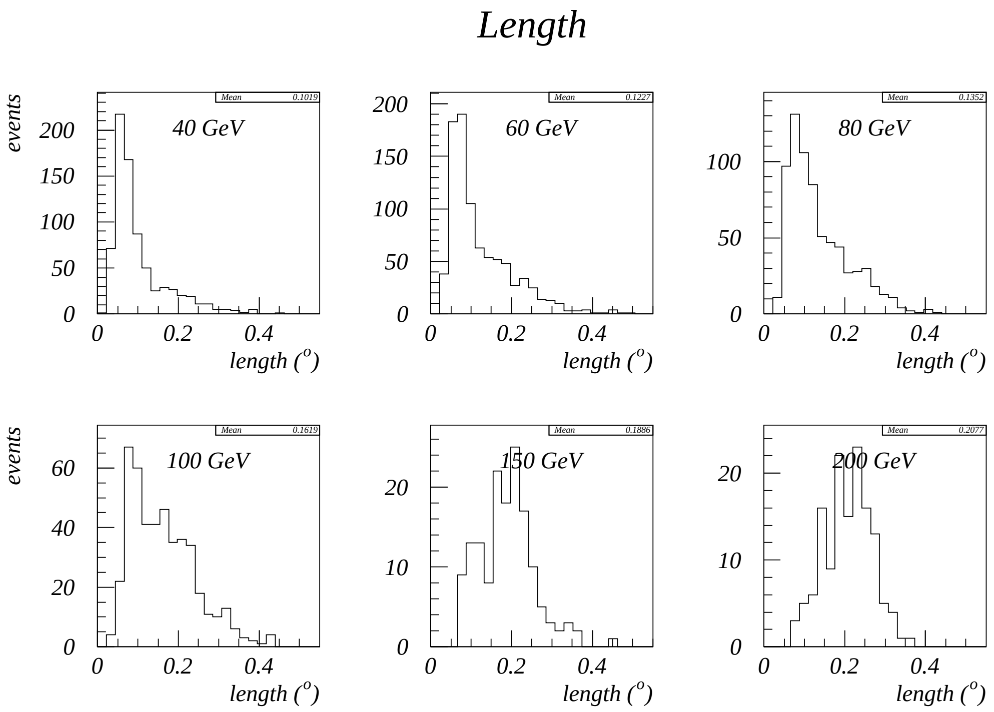

Figure 4.6: *The Length distribution for γ images of different energies.*

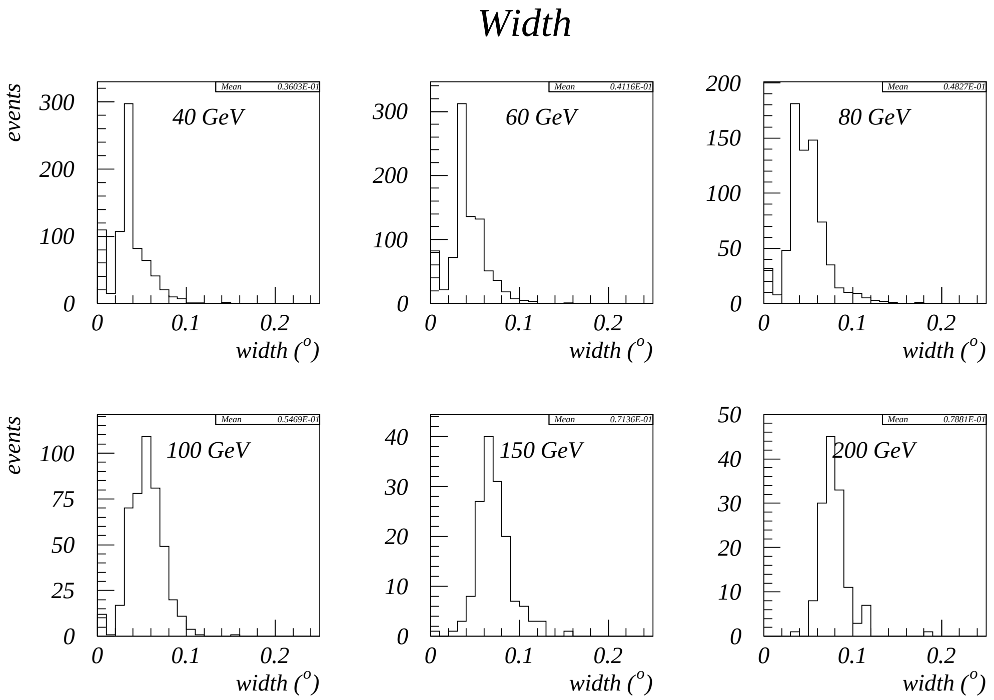

Figure 4.7: *The Width distribution for γ images of different energies.*

4.5.2 The Cosmic Electron Background

At the low energies at which MAGIC will operate for pulsar searching, cosmic electrons significantly contribute to the telescope background, and they are in principle indistinguishable from γ-rays.

Trigger Probabilities and Effective Collection Areas for Electrons

Electrons arrive isotroplically in the camera, so the shower axis was generated parallel to the telescope pointing direction ("on-axis"), but also with a certain angle δ with respect to this direction ("off-axis") in order to characterize all posible incident directions. Figure 4.8 shows the dependence of the trigger probability for electron showers on the impact parameter and energy for different shower angles of incidence δ with respect to the axis of the telescope.

In Fig. 4.9 we show the calculated collection areas after trigger for electrons, for different incidence angles δ. To allow an easier comparison with S_γ we plot S_e/Ω_0 in Fig. 4.10, where Ω_0 denotes the maximum solid angle of incidence of the showers generated, that is $1.5°$. S_e/Ω_0 can be interpreted as the average effective area for electrons within the field of view of the camera.

Differential and Integral Rates for Electrons

We can use the raw collection areas along with the electron energy spectrum displayed in figure 4.11 (taken from [45]), in order to estimate the raw rate of electron triggers in MAGIC. Figure 4.12 show the electron raw differential and integral rates at zenith as a function of electron primary energy.

From Fig. 4.12, we can see that the cosmic electron rate estimated for MAGIC is **3.4 Hz**.

4.5.3 The Cosmic Proton Background

Effective Collection Area for Protons

As in the case of electrons, we first evaluate the effective collection areas for the different shower angles of incidence δ (between 0 and $5°$) with respect to the axis of the telescope, and then, to allow an easier comparison with S_γ we plot S_p/Ω_0. In this way, the Monte Carlo evaluated effective area for protons is shown in Fig. 4.13. Due to the diffuse character and the lower light content in proton images (compared to γs of the same energy) and the restrictive trigger condition demanding a certain minimal amount of light in at least 4 neighbouring pixels, protons trigger with much smaller probabilities. This yields to a very low collection area for protons. For instance, the effective collection area is only

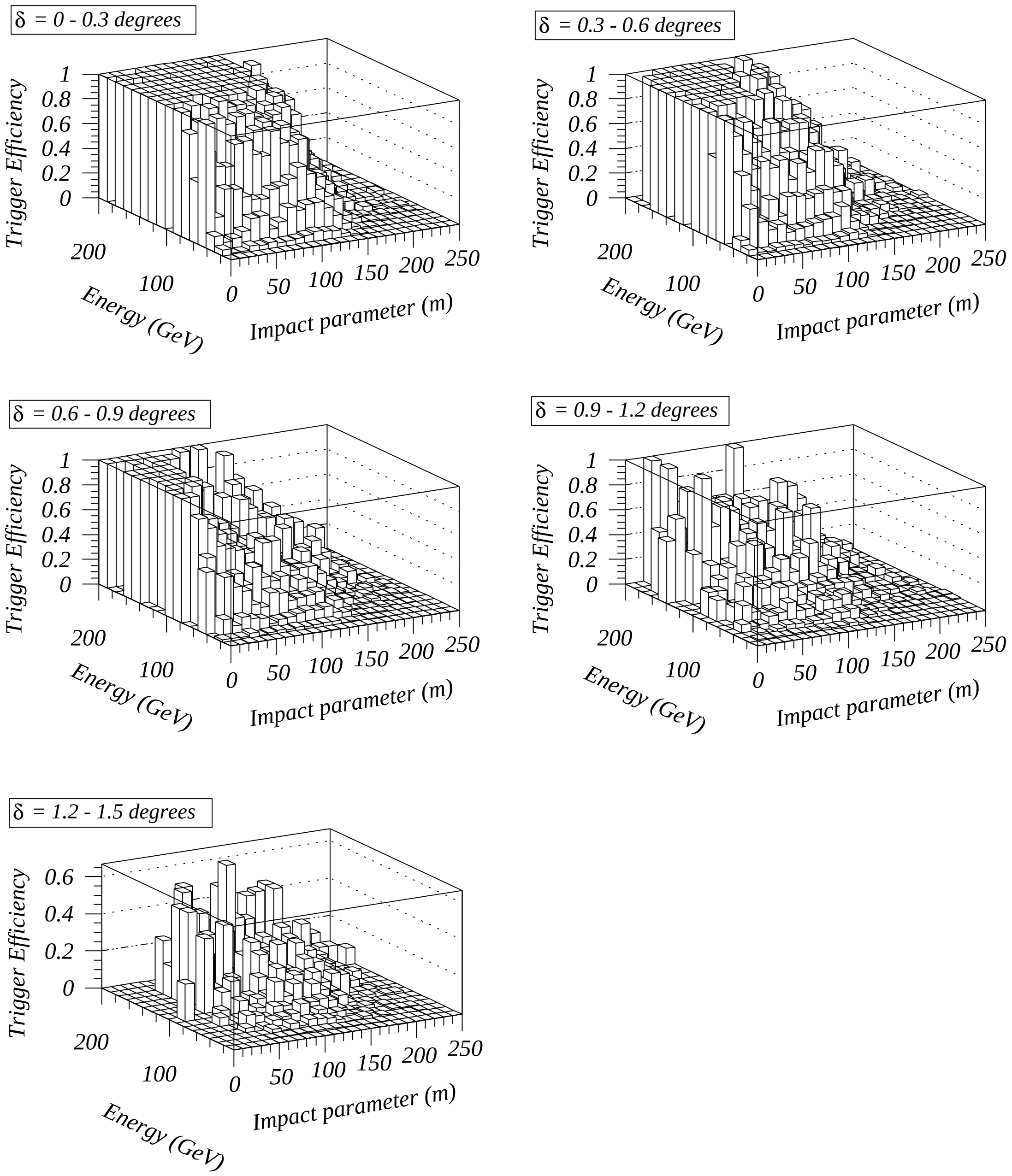

Figure 4.8: *Trigger efficiency for electrons for different shower angles of incidence δ with respect to the axis of the telescope.*

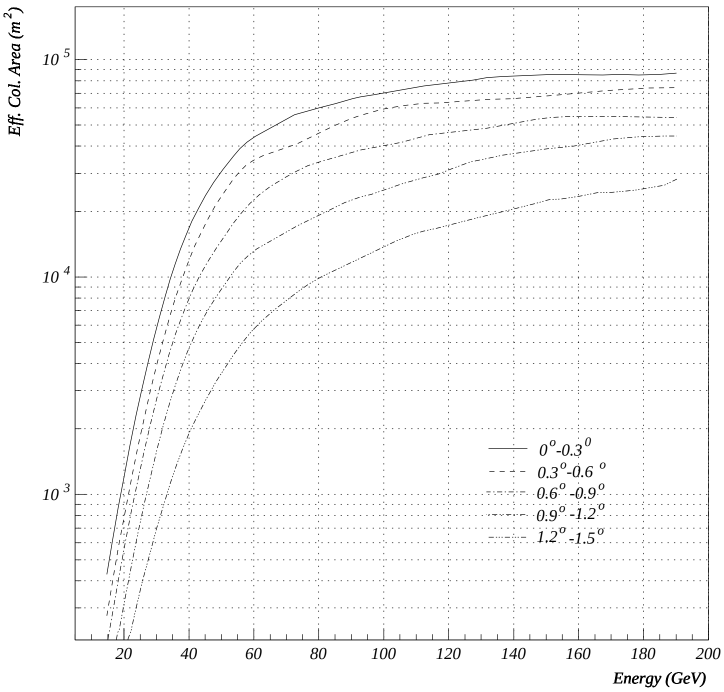

Figure 4.9: *Effective collectin area for electrons for different shower angles of incidence δ with respect to the axis of the telescope.*

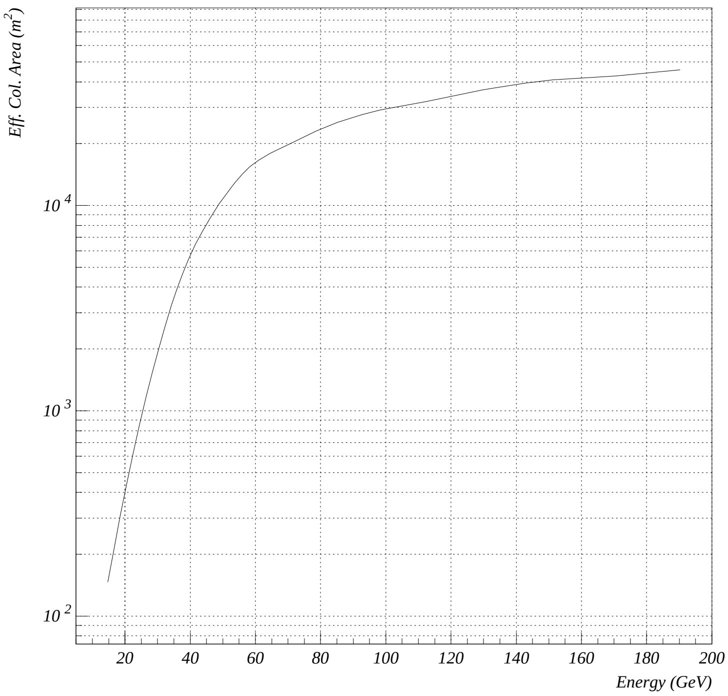

Figure 4.10: *Average collection area for electrons over the solid angle $\Omega_0 = 1.5°$.*

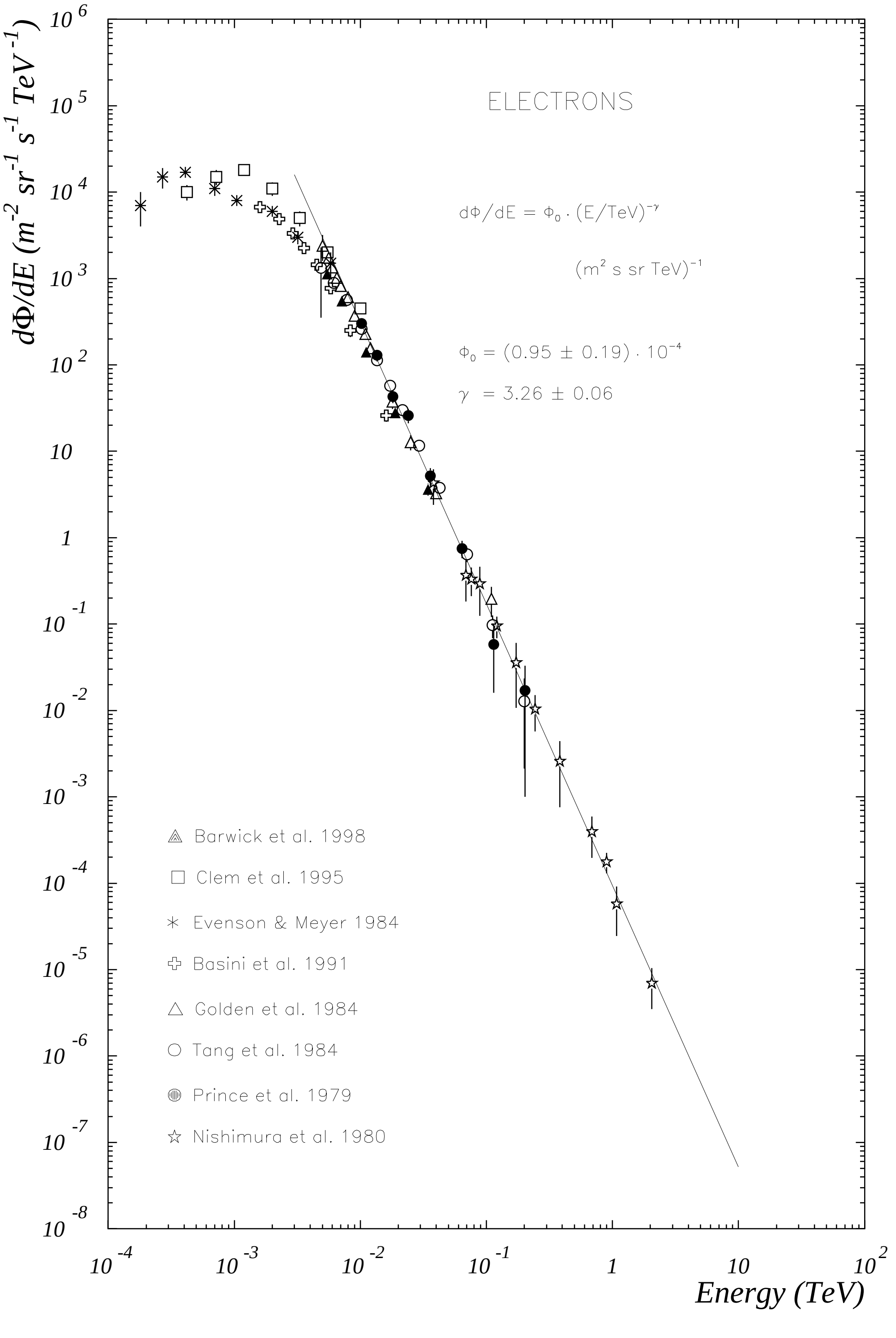

Figure 4.11: *Cosmic electron differential spectrum (from a number of different experiments as sumarized in [45])*

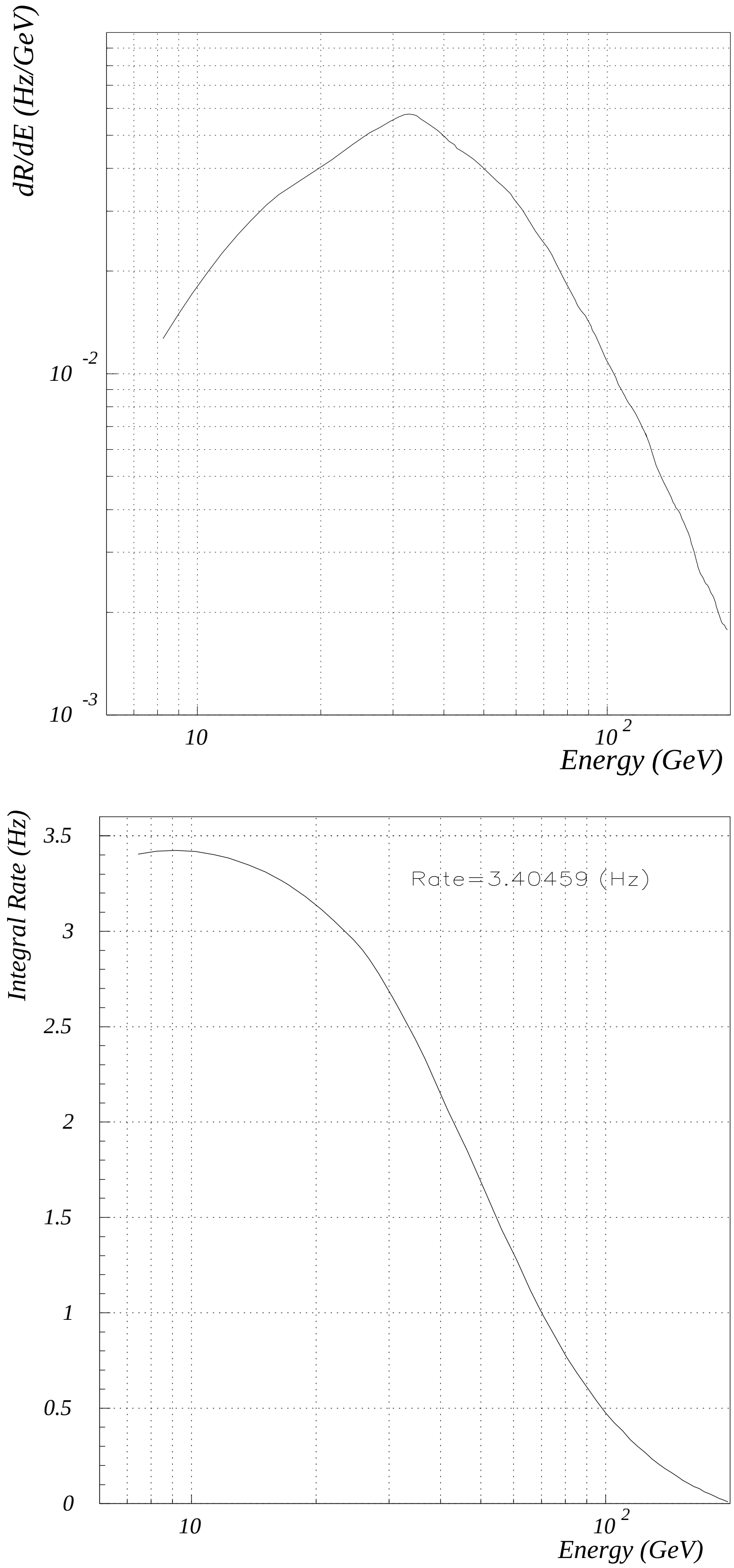

Figure 4.12: *Differential and integral trigger rates for electrons.*

$\sim 25\, m^2$ at energies of 60 GeV, compared with a collection area of $\sim 4 \cdot 10^4$ for γs at the same energy.

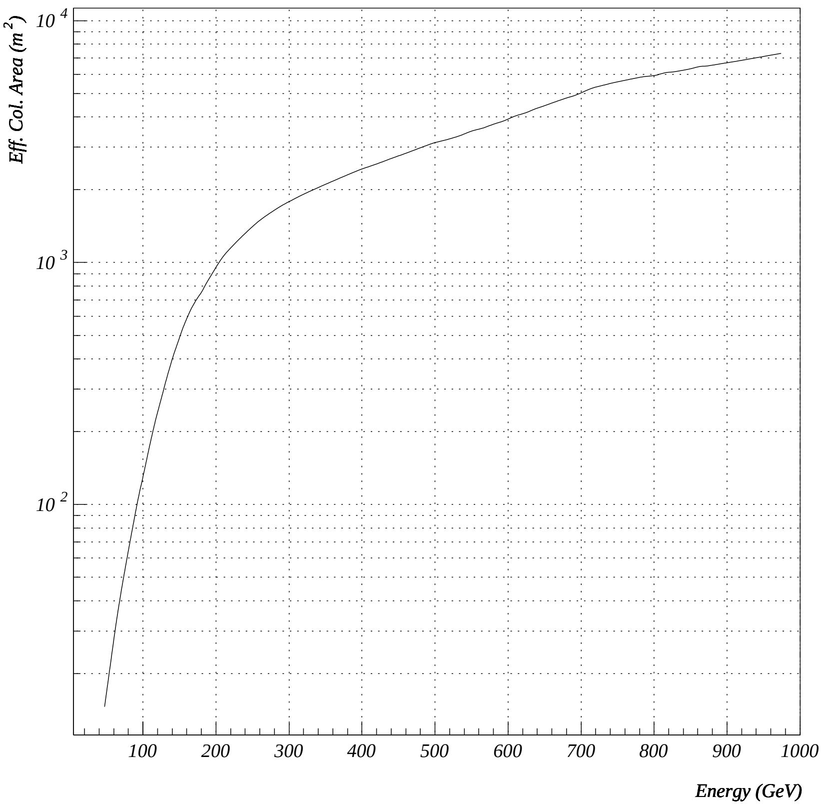

Figure 4.13: *Average collectin area for protons over the solid angle of the trigger acceptance zone* $\Omega_0 = 5°$.

The different behaviour between S_γ and S_p arises mainly since γ-ray showers generate about two times more Cherenkov light than proton-induced showers with the same energy, resulting in a lower detection threshold for γ-rays. In addition, Chrerenkov images of proton-induced showers are more diffuse than images of γ-induced showers, and therefore less likely to reach the trigger thresholds. At high energies both types of primaries produce enough light, and the effective areas are essentially governed by the radius of the Cherenkov light pool (as it was seen in §2.3.1). Therefore, the differences between S_γ and S_p/Ω_0 disappears. At very high energies, the effective area S_p/Ω for proton-induced showers grows beyond that for γ-ray showers. The reason is that now even showers with direction outside the field of view of the camera generate triggers; for example, a high-energy shower with a large impact parameter and a relatively large angle with respect to the telescope axis may still have its shower maximum within the field of view, and radiate a sufficient flux of photons towards the telescope. Conversely, because the field of view is limited for γ-induced showers, S_γ tends to a constant value and the shower image moves away out of the field of view for showers with impact parameter greater than ~ 100 m.

Integral Rate for Protons

Using the differential spectrum for the cosmic protons background, given by:

$$\frac{dF_p}{dE} = 10.91 \cdot 10^{-2} \left(\frac{E}{1\ \mathrm{TeV}}\right)^{-2.75} \quad \mathrm{m^{-2}s^{-1}sr^{-1}TeV^{-1}} \tag{4.9}$$

and the the effective collection area shown in Fig. 4.13, we obtain the integral rate for protons, as it is shown in Fig. 4.14.

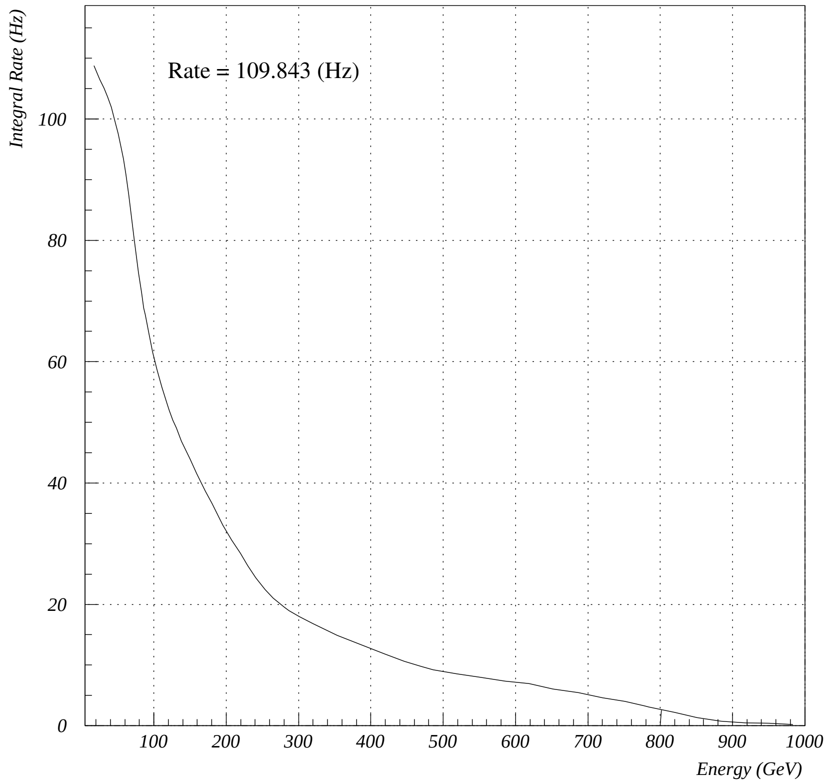

Figure 4.14: *Integral rate after triggering for protons for a camera with* 0.8° *trigger radius. The trigger condition "any 4 neighbouring pixels above the threshold of 7 ph.e.s was applied.*

The proton background rate estimated for MAGIC is about **110 Hz**. We have to note that we have only performed simulations for protons at energies below 1 TeV. Simulations up to highers energies very likely would have increase this rate.

With the values of the electron background and proton background calculated we estimate a total cosmic background rate of ~ 115 Hz. This will be the background rate that we will use in the next chapter.

Chapter 5

Study of the Power of MAGIC for the Observation of γ-ray Pulsars

One of the main goals of this work is to know is the MAGIC Telescope will be able to observe the seven known γ-ray pulsars, so far only detected by the EGRET instrument. As we said in §1.3 this will be of great important since it would allow to study for first time the pulsar spectra cutoff with takes place at some GeV, above the detection limit of EGRET and far below the energy thereshold of the current IACT telescopes. Our Monte Carlo simulations performed in the previous chapter show that it is well possible to use the MAGIC Telescope for the observation of γ-ray pulsars above 10 GeV. But as we will see in this chapter, it is also neccesary that MAGIC is able to detect them in few hours. Then, for knowing the power of MAGIC for the detection of the EGRET pulsars we will need to calculate the hours required for MAGIC to obtain a significant detection from them.

Firstly, we will use the effective collection area for γ events obtained in the previous chapter, for evaluating the MAGIC detection rates for each of the EGRET pulsars. And then with these rates and with the background rates, along with some statistics, we will obtain the observation times required for the detection of these pulsars.

Finally, we will try to predict the shape of the pulse profiles that MAGIC should observe from the EGRET pulsars at energies above 10 GeV. For that, we will do skymaps with each single photons recorded by EGRET from the position of these pulsars.

5.1 Expeted MAGIC Detection Rates for EGRET Pulsars

According with §4.3, the expected MAGIC γ-ray rates for EGRET pulsars are calculated just by multiplying the MAGIC effective collection area for γ events $S_\gamma(E)$ by the pulsar spectra dN_γ/dE, and then integrating over the energy range of the γ showers simulated (5-200 GeV):

$$R_\gamma = \int_5^{200} \frac{dN_\gamma}{dE} S_\gamma(E) dE \tag{5.1}$$

The MAGIC effective collection area was obtained in the previous chapter (Fig. 4.3). An for the pulsar spectra we follow the procedure described by de Jager et al. [38, 40] based on the polar cap model, modelling the spectra above 1 GeV as a power law times an exponential cutoff with cutoff energy E_0:

$$\frac{dN_\gamma}{dE} = K \left(\frac{E}{E_n}\right)^{-\Gamma} exp(-(E/E_o)^b) \tag{5.2}$$

where the constant K represents the monochromatic flux at the normalising energy $E_n \ll E_o$. We will normalise spectra at E_n near 1 GeV. The strength of the cutoff is determined by the index b. The most conservative estimate for the detection sensitivity is to take $b > 1$, consistent with magnetic pair production above the polar cap, whereas a value of $b < 1$ will yield a very optimistic detection rate.

Table 5.1 shows the spectra parameters used for our calculations. They were obtained by de Jager, as the result of a fit of the total pulsed spectra of the six brightest EGRET γ-ray pulsars to Eq.5.2 (see Ref. [39]). These spectral parameters reproduce the EGRET flux up to 30 GeV, and are consistent with the TeV pulsed limits from observations with CTs. They also reproduce the GeV source catalog flux of Lamb & Macomb [41]. In the case of Vela and Geminga the cutoffs are well defined by the EGRET data and errors on E_0 are relatively small ($\sim 20\%$). In the case of Crab and PSR B1055-52, some evidence on turnover is seen in te spectra above 10 GeV, although it is difficult to obtain reliable measures of E_0 and b. In the case of PSR B1951+32 and PSR B1706-44 there is no evidence of a turnover up to 30 GeV, and a minimum value of $E_0 = 40$ GeV (consistent with EGRET) was selected. With $b \geq 1$, we find that K for EGRET pulsars are typically large, so that it is desirable to push the trigger threshold as low as possible. If q_0 is the photo-electron threshold, then, to first order, we find that the integral cosmic ray background typically scales as $q_0^{-1.7}$ and the accidental triggers due to the night sky background (NSB) scales as $\sim q_0^{-4}$ (with the exact exponent depending on the trigger logic). If q_0 corresponds to an energy just above E_0 (which lies between 5 GeV and 40 GeV, as seen in Table 5.1) then the signal to noise ratio rises faster than the NSB as the threshold is reduced, until

Object	k ($\times 10^{-8}$) ($\mathrm{cm^{-2}s^{-1}GeV^{-1}}$)	Γ	E_o (GeV)	b	$F(>1\ \mathrm{GeV})$ ($\mathrm{cm^{-2}s^{-1}}$)
Crab	24.0	2.08	30	2	22
PSR B1951+32	3.80	1.74	40	2	4.9
Geminga	73.0	1.42	5.0	2.2	76
PSR B1706-44	20.5	2.10	40	2	20
PSR B1055-52	4.00	1.80	20	2	4.5
Vela	138	1.62	8.0	1.7	148

Table 5.1: *Gamma-ray spectral parameters above 1 GeV.*

the effective threshold is just below E_0. This holds especially for a very bright pulsar such as Geminga, which is known to have a large value of K, $E_0 \sim 5$ GeV, and $b \sim 2.2$. The only limit then is the constraints imposed by the data acquisition system. This type of operation is then called the *pulsar mode*, as opposed to the normal imaging mode operating at higher thresholds.

In figures 1-6 the expected differential and integral rates obtained for each of the EGRET pulsars are shown. And in table 5.1 the detection rates are tabulated. Notice that only Crab, PSR B1951+32 and Geminga can be observed from the MAGIC location at la Palma (latitude $\sim 29°$)

Object	R_γ ($\mathrm{hour^{-1}}$)
Crab	771
PSR B1951+32	660
Geminga	22
PSR B1706-44	1034
PSR B1055-52	121
Vela	414

Table 5.2: *MAGIC rates for EGRET pulsars.*

5.2 Required Observation Times for EGRET Pulsars

Next we will calculate the minimum observation time required for detecting each of the EGRET pulsars. Given a pulsed γ-ray rate R_γ over a background rate R_B, for the minimun time we understand the observation time T that we need to obtain at less a marginal detection at the significance level $x = p\sqrt{N}$ where $N = (R_B + R_\gamma)T$ is the total number of events detected during that time, and $p = R_p(R_B + R_\gamma)$ is the so-called pulsed fraction (as shown in [43]). So, the

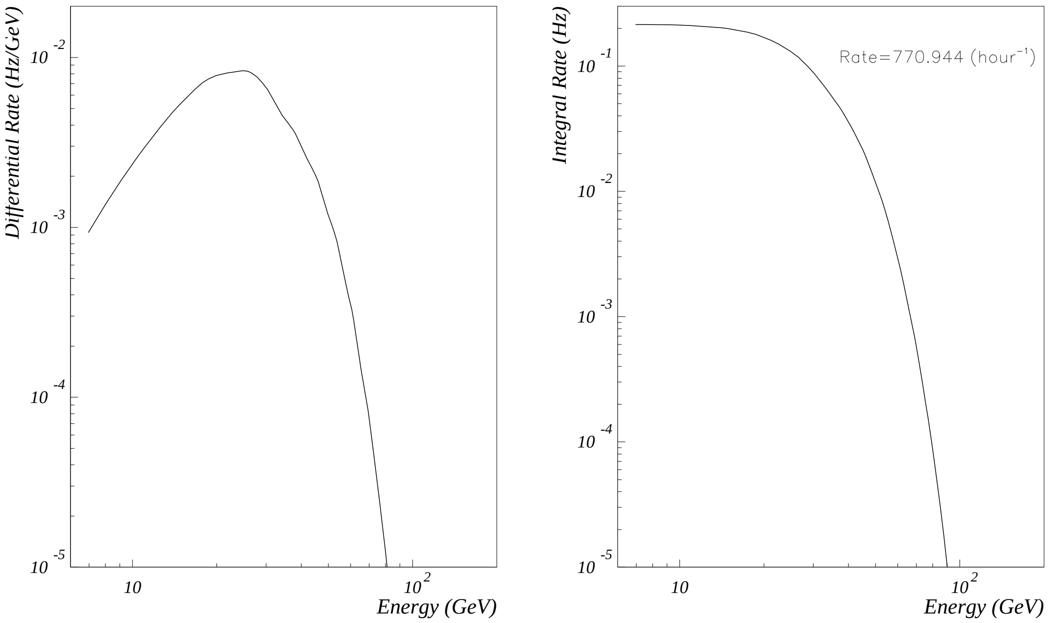

Figure 5.1: *Differential and integral detection rates for the Crab pulsar.*

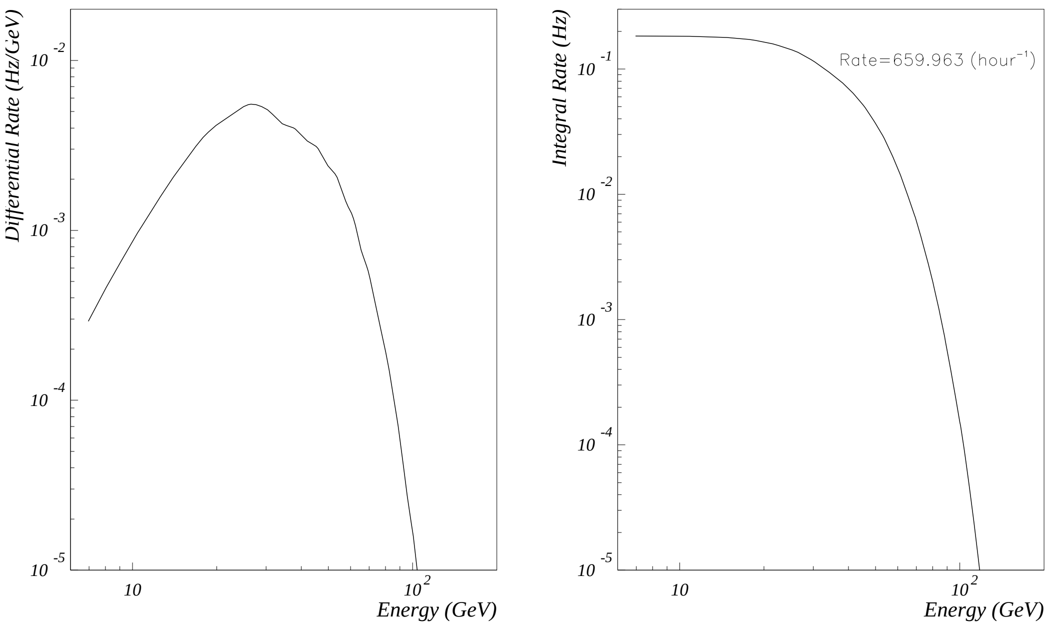

Figure 5.2: *Differential and integral detection rates for PSR B1951+32.*

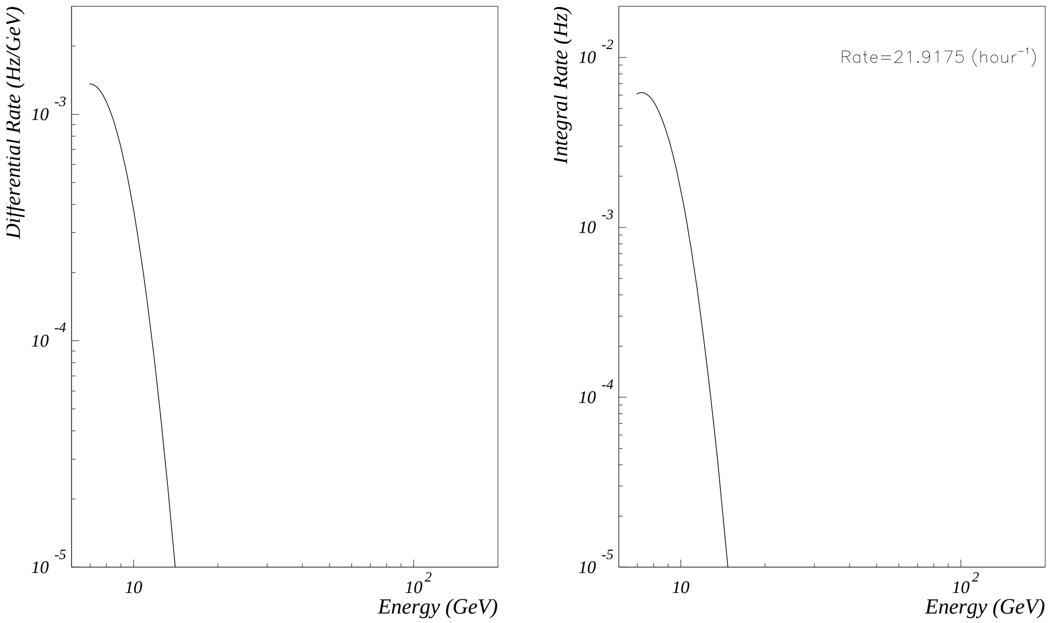

Figure 5.3: *Differential and integral detection rates for Geminga.*

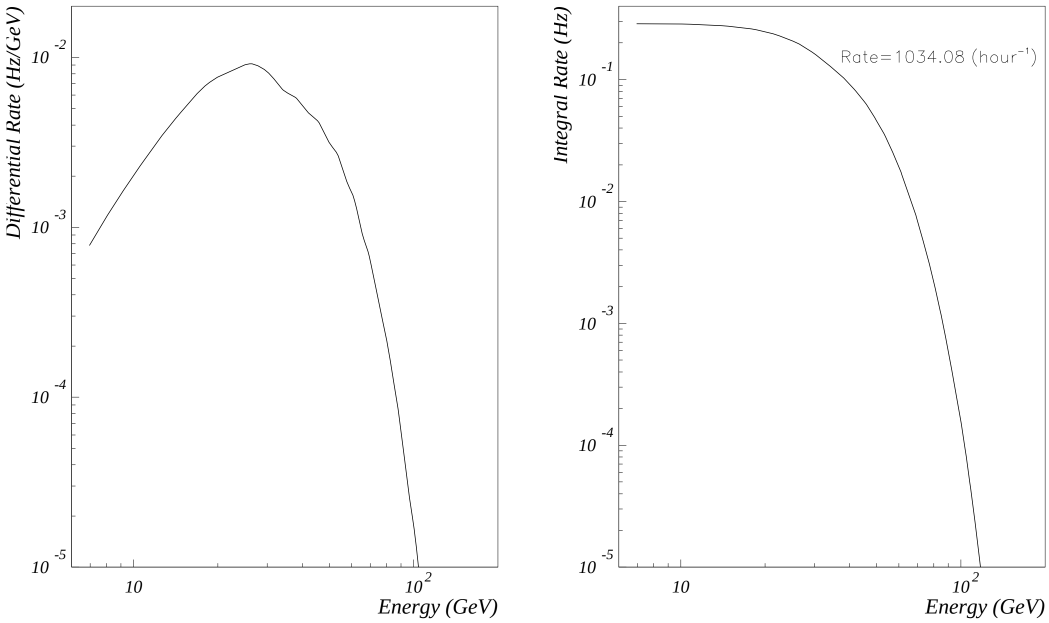

Figure 5.4: *Differential and integral detection rates for PSR B1706-44.*

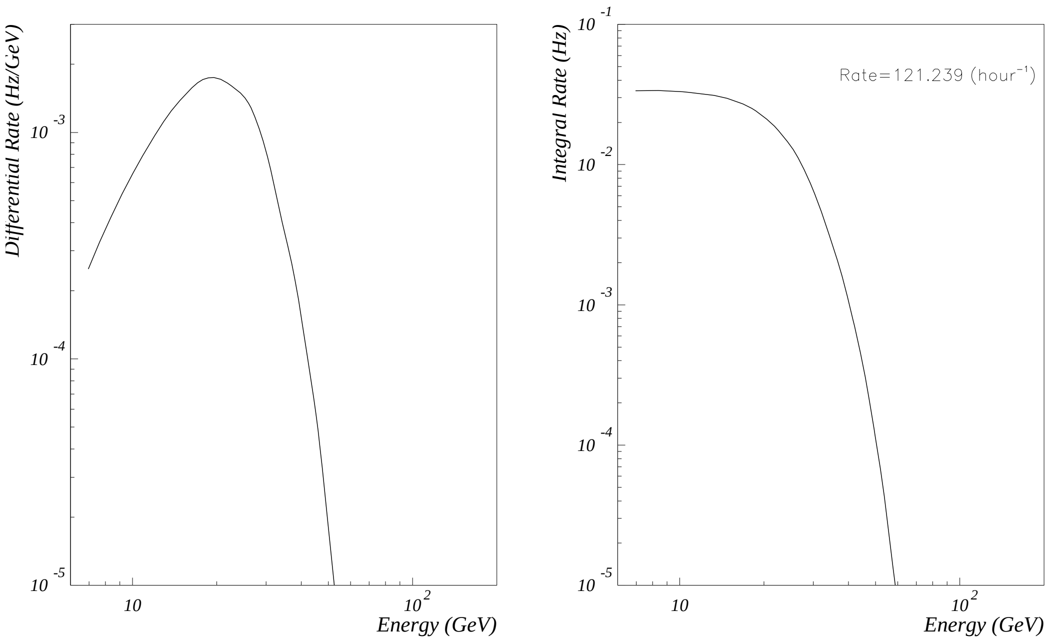

Figure 5.5: *Differential and integral detection rates for PSR B1055-52.*

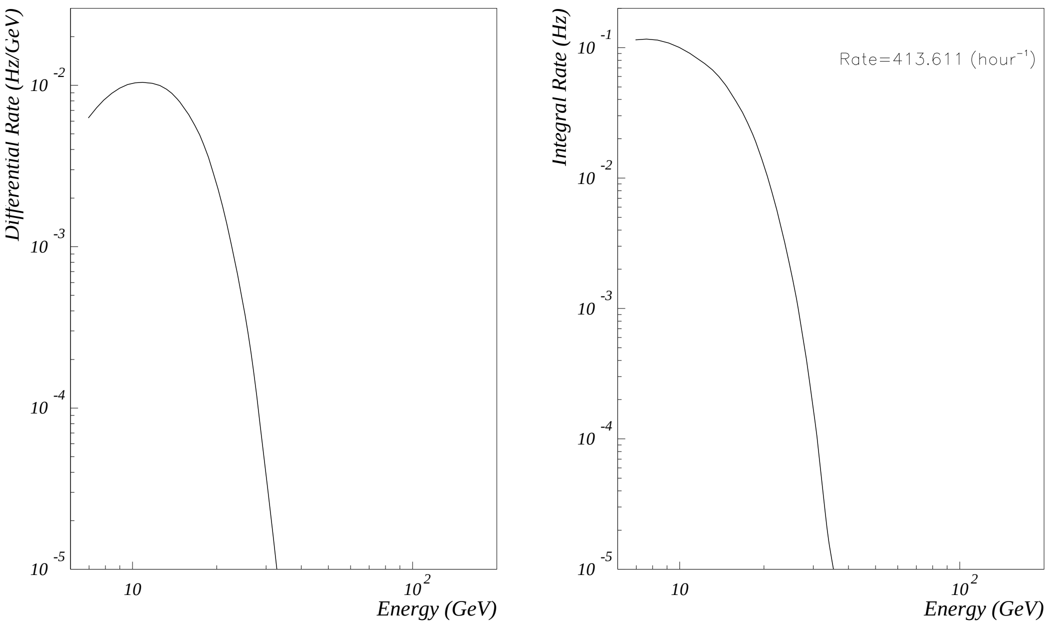

Figure 5.6: *Differential and integral detection rates for Vela.*

required time for having a detection at the significance level x is:

$$T = \left(\frac{x}{R_\gamma}\right)^2 (R_\gamma + R_B) \tag{5.3}$$

We have to take into account that for the observation of pulsars we will not have imaging capability since the values of the pulsar cutoffs E_0 are near the MAGIC detection threshold, and at these energies the showers are more round and very small. This causes that the accuracy of determining both the orientation and the shape parameters deteriorates at theses energies. Thererby, the way how we plan to do γ-ray pulsar searches with MAGIC is not by using the γ/hadron separation technique, but by mean of timing analysis. This is, after some hours of observation of the source, a test statistic (as for instance the well-known Z_m^2 test) will be used on the observational data to look for a periodicity. Then, one will claim a pulsar detection if the value of this statistic is high enough, that is, if the chance probability of that signal is due to statistic fluctuations is very small. As we will see in § 5.3 we expect that only a single sharp peak (typically P2 for Crab and PSR B1951+32, with duty cicle of δ=5%[1]) survives in the pulse profile above 10 GeV. Hence, we can model the pulse profile at these energies as a Gaussian function with a 5% FWHM. For this situation the Z_m^2-test with number of harmonics $m = 1/(2\delta) = 10$ should be optimal. As shown by de Jager [42], the expected value of the statistic is $< Z_m^2 >= x^2\Phi + 2m$, where Φ is derived from the form of the pulsar pulse profile, which for a Gaussian with a 5% FWHM takes a value of $\Phi = 5.8$. Thus, a DC excess of $x = 3\sigma$ above the sky background should give $< Z_{10}^2 >= 72$ which gives an average chance probability of 8×10^{-8} if the period is known. But we must notice that if the period is unkwown we would have to multiply this probability for the number of trials. If we want to search for a new pulsar in a $T = 6$ hour run in a frequency interval of Δf from 1 to 30 Hz (to searching for period as short as 20 ms) the factor of oversampling would be $\eta \sim 10$ per independent Fourier frequency. The total number of independent trials would then be $M = \eta T \Delta f = 6.5 \times 10^6$ and therefore the chance probability would be only of 0.5 after multiplying with all the trials. This should bury the true frequency among one of many candidate frequencies, which can be confirmed by one or two follow up observations the next few nights. The constraint for pulsar searches is that the detection must be done in a night, since the observational conditions and the pulsar period can vary from one night to the other. So, the MAGIC obersevation times for the detection of the EGRET pulsar are required to be less than $\sim$ 6 hours.

Table 1 shows the required observation times T_{115} (R_B = 115 Hz) and T_{50} (R_B = 50 Hz) for the pulsars with $x = 3\sigma$. The total expected MAGIC background rate that we obtained in the previous chapter is $\sim$ 115 Hz. The arbitrary

[1]The duty cicle is the peak width of the pulsar pulse profile, measured at the peak half maximum (FWHM).

rate of $R_B = 50$ Hz assumes some degree of background rejection based on a size- and distance cut, but detailed simulations are required to determine the best rejection factor against background. The only purpose of showing T for two background rates is to show how this time scales with the background. From the

Object	T_{50} (hours)	T_{115} (hours)
Crab	3	6.3
PSR B1951+32	4	8.6
Geminga	$\sim 10^3$	$\sim 10^4$
PSR B1706-44	2	3.5
PSR B1055-52	111	255
Vela	9	21.8

Table 5.3: *MAGIC observation times for the detection of the EGRET pulsars. Two different values for the background rate were used.*

table it is clear that we have to reach a background rate of less than 50 Hz after making suitable size- and distance cuts, so that a detection of Crab and PSR B1951+32 can be realised within one night. These two pulsars also transit close to La Palma, so that the minimum threshold energy can be realised at transit.

5.3 The Pulsar Sky Above 10 GeV

Now that we know that MAGIC will be very likely able to detect pulsed γ radiation above 10 GeV coming from the Crab and PSR B1951+32 pulsars, we ask ourselves how the EGRET pulsars look like in the new *energy window* which will be opened by MAGIC. Specifically, we want to know the shape of the expected pulsar pulse profile at these energies, as well as to see the relative proportion of pulsed and unpulsed γ-photons. For that, we have pressed the limits of EGRET by plotting individual sky photons above 10 GeV, where the effective collection area for MAGIC is already near a hundred square meter, which is already orders of magnitude larger than the corresponding collection area of EGRET, but at the cost of a high background relative to EGRET. We have used the public EGRET data from 1991 to 1997, and photons have been selected using a 2° angular cut around the position of each pulsar.

The more important result is that, whereas the pulse profiles of Crab, Vela, Geminga and PSR B1706-44 show typically two peaks per rotation, as shown by Thompson, 2001 [36] (see Fig. 5.7), we find that the second peak for Crab, Vela and Geminga becomes a significantly dominant feature above 5 GeV, and the first pulse for the case of PSR B1706-44. The pulse profile shape above 5

GeV may also resemble the expected profiles for MAGIC operating in the pulsar mode.

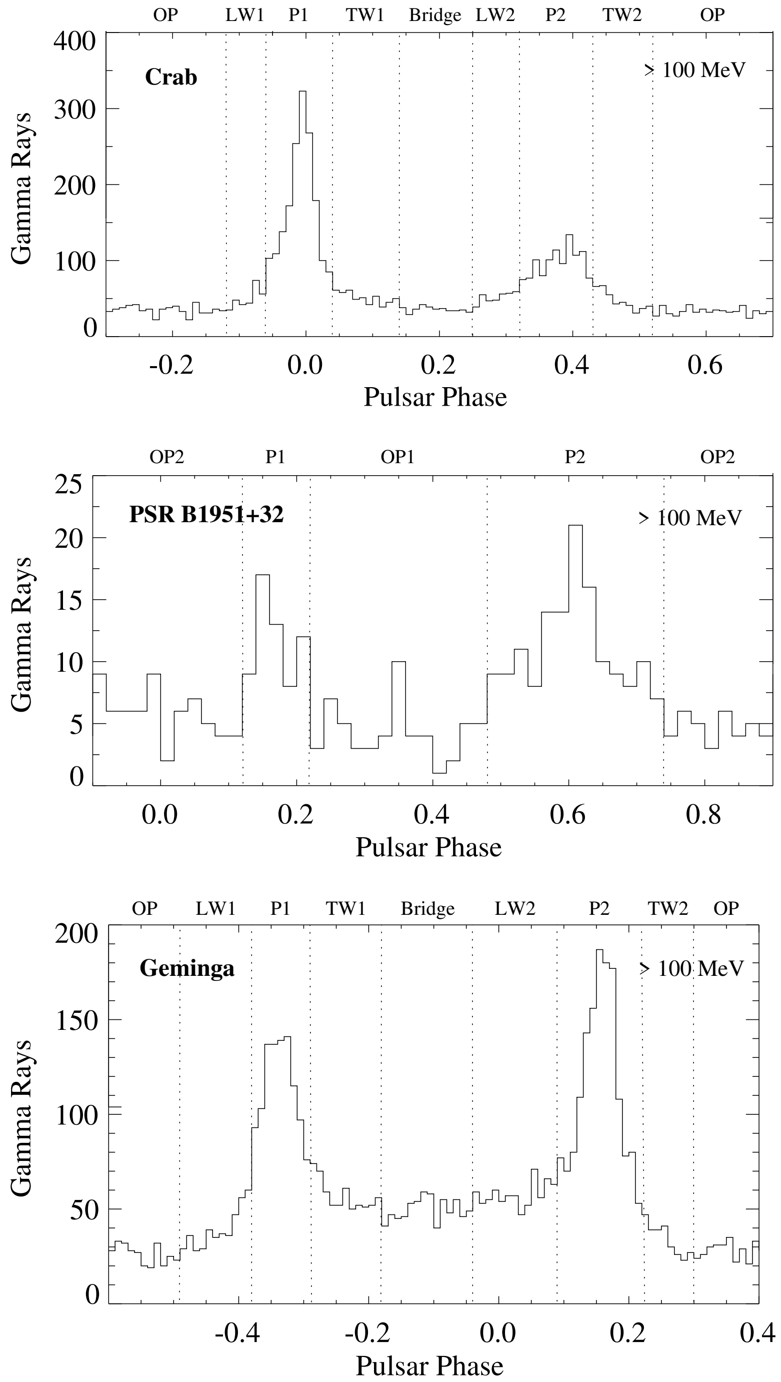

Figure 5.7: *Crab, PSR B1951+32 and Geminga γ-ray pulse profiles formed by epoch-folding all events above 100 MeV accumulated by the EGRET instrument during the years 1991-1994. Taken from [37].*

Below, we show our results only for the three EGRET pulsars which will transit at La Palma.

Figure 5.8 shows a skymap of the Crab region above 10 GeV. Seven, possible nine, photons are associated with the Crab (numbered 1 through 9) over a background of 5 unpulsed photons. The 5 GeV peak reported by Thompson extends between the leading wing of peak 2 (LW2), through peak 2 (P2). (See Fig. 5.7 for the definitions of the different regions of the pulse profile). In this region we possibly see three pulsed photons associated with the LW2+P2 structure.

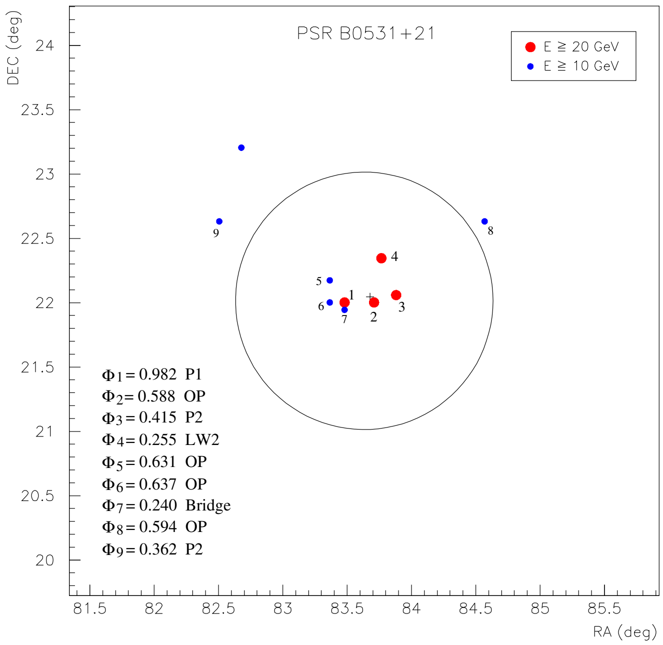

Figure 5.8: *A* $\sim 4^\circ \times 4^\circ$ *area of the* γ*-ray sky above 10 GeV around Crab. The cross denotes the position of the Crab pulsar and the solid circle the 95% acceptance area for photons above 10 GeV relative to the Crab. Each photon is indicated by a solid circle, with the circle size corresponding to the energy (see legend). The pulsar phase identification is as follows: (P1 - first peak; P2 - second peak; LW2 - leading wing 2; OP - offpulse).*

Figure 5.9 shows a similar picture for PSR B1951+32, but with only two photons in the 95% confidence circle for 10 GeV γ-rays. The phase difference between the two photons is 0.02, and both are associated with the sharp second pulse (P2), consistent with Fierro (1996) [37]. The third photon is marginally consistent with both the point spread function and the edge of P2. It is remarkable that there are not background photons around the postion of this pulsar. The two or possibly three pulsed photons are the result of the claim of an unchanged spectrum between 100 MeV and 30 GeV. Thus, Crab and PSR B1951+32 may have a similar pulsed brightness above 10 GeV, whereas PSR B1951+32 is much weaker compared to the Crab near 100 MeV, which is a result of the harder spectrum of PSR B1951+32. Crab and PSR B1951+32 will be prime candidates for MAGIC (pulsar mode) given their optimal declinations relative to the latitude of La Palma.

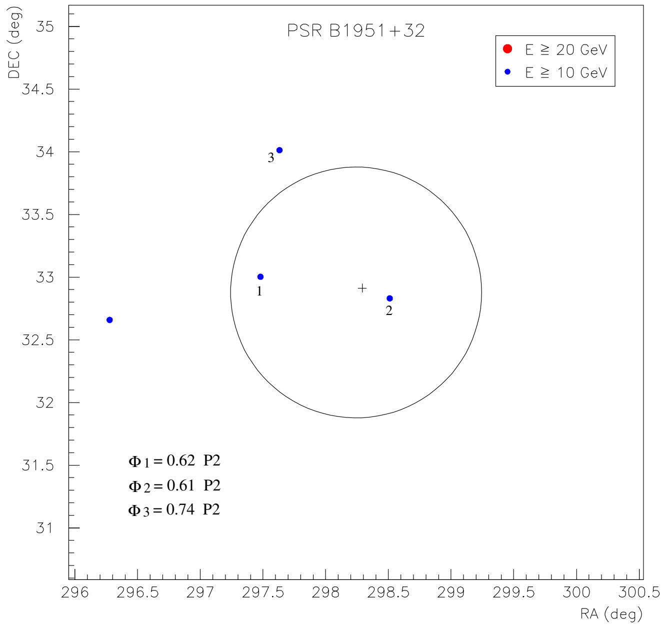

Figure 5.9: *A skymap of photons above 10 GeV around the position of PSR B1951+32 with the corresponding 95% confidence circle for 10 GeV photons relative to the pulsar (similar to Fig. 5.8). The pulsed photon phases are consistent with the second peak (P2) as indicated.*

In figure 5.10 we see the sky map for Geminga, which shows 5 pulsed photons inside the 95% confidence circle. They also belong to the second peak. This result is quite surprising since the Eq. 5.2 based on the polar cap model predict a energy cutoff for Geminga of 5 GeV. If we have found five photon in the EGRET database above 10 GeV (two of them above 20 GeV) it could mean that the γ emission in Geminga is produced according to the outer gap model.

As we have seen in §5.2, the pulsed spectra of Crab and PSR B1951+32 extrapolate to energies above 10 GeV (although with large errors), which should allow a detection within a few hours if the background can be reduced to 50 Hz. Investigating the sky maps of these pulsars above 10 GeV, we see that this conclusion is based on the existence of no more than 5 EGRET pulsed photons above 10 GeV from each of these sources, but buried in a very low 10 GeV background rate. In the case of Geminga we have shown that it seems to be impossible to detect any pulsed radiation given the fast cutoff of the pulsed spectrum below 10 GeV. However, the Geminga skymap above 10 GeV also shows five pulsed photons, which would, by analogy, also imply a detection within

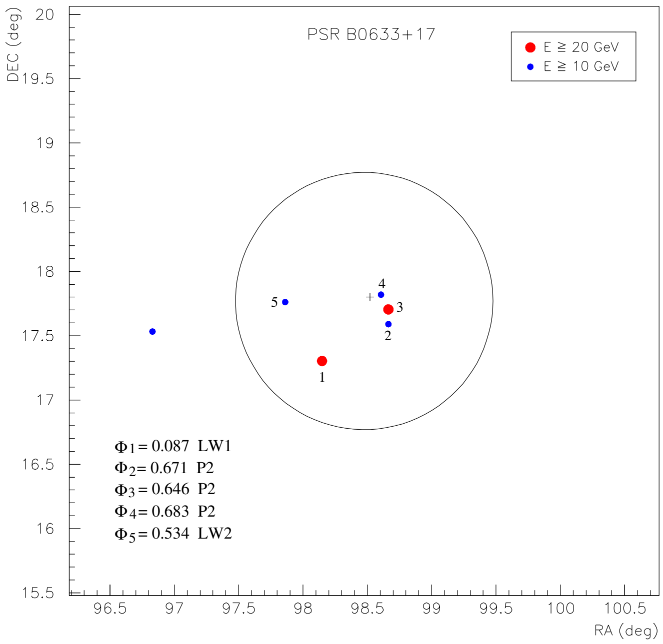

Figure 5.10: *A skymap of photons above 10 GeV around the position of Geminga for the 95% confidence circle. The pulsed photon phases are consistent with the second peak.*

one night. The long observation time for Geminga is a pathological effect of multiplying a spectrum dropping like a wall with a collection area rising similarly like a wall, and if the two walls do not overlap, the expected rate is zero requiring infinite observation time, whereas a slight reduction in threshold energy would allow the two walls to coincide in energy. Thus, in theory, Geminga may also be detectable within a single night under ideal conditions, provided that the trigger can be driven into the night sky background, and if the rejection against background cosmic ray showers (size- and distance cuts) can be managed at a hardware level.

Chapter 6

The Effect of the Geomagnetic Field on the Cosmic Electron Background

The cosmic electron background is going to be a limiting factor for the observation with the new generation of Cherenkov telescopes at energies of some tens of GeV. This is not only because at these energies it is the most important background (along with the LONS) to be taken into account (remind that we saw how the proton background is negligible at low energies), but also because electron-iniated showers are indistinguishable from γ-initiated showers, what makes impossible the use of the imaging technique. For this, the cosmic electron background is usually named the *irreducible background* of an IACT.

A difference of γ-rays, electron are charged particles, and therefore they are affected by the Earth's magnetic field as they come from the outer space to the Earth's surface. The effect of this magnetic field on the electrons is the same as the effect that any charged particle ungergoes when it moves through a magnetic field, namely, their trajectories are deflected somehow by the magnetic field lines, an even if their energies are low enough they can been prevented from reaching the Earth surface. Acting in this way the Earth's magnetic field as a filter for energies below a certain cutoff energy. This effect makes we ask ourselves wheather the Earth's magnetic field is going to prevent a considerable fraction of cosmic electrons (below a certain energy) from reaching the Earth, and then, from triggering the telescope.

In this chapter we will investigate the effect of the geomagnetic field in the cosmic electron background, following [34]. Firstly we will evaluate the energy cutoff for electron, below which, electron are preventing from reaching the Earth, and thus from initiating atmospheric showers. If this cutoff is relevant for our studies, that is, if we obtain a value for this cutoff about ~ 10 GeV, we will re-calculate the electron background rate for MAGIC.

6.1 The Earth's Magnetic Field composition

Until the discovery of the Solar Wind and the Earth's magnetosphere, it was natural to suppose that the magnetic field of the Earth is of dipole form and that it is through this field that the particles are propagated to the surface of the Earth. Nowdays, the magnetic field and particle distributions in the vicinity of the Earth have been well determined by space probe experiments and the results of these are shown schematically in Fig. 6.1. In the figure, the different

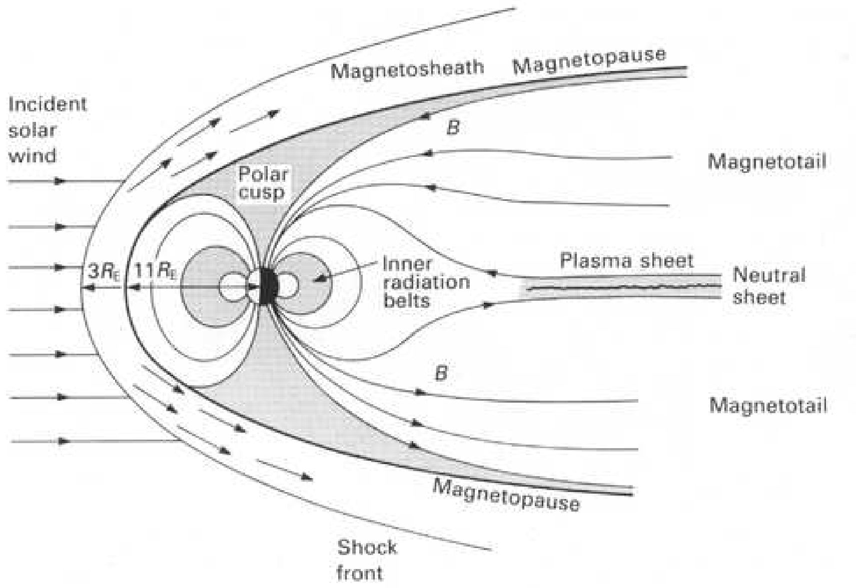

Figure 6.1: *A schematic diagram showing the structure of the Earth's magnetosphere. The names of various regions are shown.*

regions of the geomagnetic field are shown. There is a "bow" shock, similar to the bow shock in front of a solid object at a distance of about $14R_E$ (where R_E is the radius of the Earth) from the centre of the Earth in the direction of incidence of the Solar Wind, wich confines the Earth's magnetic field inside a cavity called the *magnetosphere.* Closer to the Earth, there is a boundary known as the *magnetopause* at a distance of about $11R_E$ which acts as the surface of the region within which the Earth's magnetic field is dynamically dominant. For the purpose of visualization, the magnetopause may be thought of as the surface of a solid obstacle. The Solar Wind plasma flows past the Earth between the schock wave an the magnetopause.

The Earth's dipole magnetic field is strongly perturbated by the flow of the Solar Wind so that, although it can be well represented by a magnetic dipole close to the surface of the Earth, further away it is distorted as shown in Fig. 6.1. Perhaps the most significant distortion is the fact that the magnetic field-lines of the down-stream side of the Earth are stretched out by the drag of the

Solar Wind. The magnetospheric cavity is stretched out into a long cylindrical region which has radius about $25R_E$ at the distance of the Moon's orbit, i.e. at a distance of about $60R_E$. This region is known as the *magnetotail*. The magnetic field lines are oppositely directed on either side of the equatorial plane, those in the northern region heading towards the Earth, those in the southern region pointing away from the Earth. Between the two regions is a thick layer of hot plasma which is known as the *plama sheet*. Because the magnetic field lines run in opposite directions on either side of the plasma sheet, there must be a surface of zero magnetic field separating the two regions which is known as *neutral sheet*. And because the magnetic field changes sign through the neutral sheet, an induced electric current flows in it and hence particles can be accelerated in the vicinity of the neutral sheet, creating magnetic fields which effect has to be add to the own Earth's magnetic field.

Therefore, we see that the Geomagnetic Field (GF) is a combination of several magnetic fields produced by different sources:

- The magnetic field generated inside the Earth, known as "main field" or "internal field". It represents more than 90% of the total GF. The main field can be described as a dipole (as in the original work of Störmer [44]) or more precisely as high order harmonic expansion whose coefficients are based on experimental observations and updated every few years, the so-called International Geomagnetic Reference Field (IGRF).
- The solar wind interacts wind the Earth's field and its effect is described by an external field. The currents induced in the magnetosphere and ionosphere may create magnetic fields as large of 10% of the main field and are varible on a much shorter time scale. Magnetohydrodynamic models are called for in order to describe the whole GF, such as Tsyganenko [46] or the Integrated Space Weather Prediction Model (ISM) [47, 48].

6.2 Effect of the Geomagnetic Field on Cosmic Rays: the Rigidity Cutoff

As early as 1929 there was evidence that the dipole component of the Earth's magnetic field influences the flux of cosmic radiation. In that year, Clay was travelling from Java to the Netherlands to calibrate his ionisation detectors at the bottom of a Dutch salt mine. During the voyage, he observed variations of the numbers of charged particles arriving at the Earth as a function of geomagnetic latitude, i.e the polar angle λ measured with respect to the equatorial plane of the Earth's magnetic field. And by 1932, Compton showed that the intensity of the cosmic radiation follows closely lines of geomagnetic latitude.

The effect of the geomagnetic field on the charged particles which come to the Earth is to bend their trajectories. This prevent low energy cosmic rays from penetrating through the magnetosphere and reaching the Earth's surface. Thus, for each location and for each direction on the Earth, there is a threshold energy below which primary particles do not cotribute to production of atmospheric showers. This energy is called the *geomagnetic cutoff energy*, although the magnitud which is usually used is the *rigidity* (since the effects of a magnetic field upon a charged particle depend only on the ratio of its momentum). The rigidity of a particle is defined as pc/ze, where c is the speed of light, p is the momentum and ze is the charge of the particle, and threfore, it has dimensions of volts[1]. The minimum allowed rigidity is known as *rigidity cutoff*.

6.3 Rigidity Cutoff Calculation

An analytical expression for the rigidity cutoff can only be obtained if we underestimate the external field, and if we approximate the Earth's internal magnetic field for a dipolar field. It is also possible to obtain more accurate values for the rigidity cutoff by describing the geomagnetic field as a multipolar field based on the IGRF coefficients, but in this case, only numerical solutions can be found.

6.3.1 Dipolar Aproximation

In the case of a dipole GF the rigidity cutoffs can be calculated analytically [44]. For our work we will draw mainly on an expession for the rigidity cutoff (R_c) given by Cooke [49] which is based on a dipole approximation to the IGRF1980:

$$R_c = \frac{59.4\cos^4\lambda}{r^2\left[1+(1-\cos^3\lambda\sin\theta\sin\phi)^{1/2}\right]^2}\ [GV]. \tag{6.1}$$

where λ is the magnetic latitude, θ is the zenith angle, ϕ is the azimuth angle measured clockwise from the magnetic north and r is the distance from the dipole center (in Earth radius units).

Analytical procedures always underestimate R_c due to the effect of the Earth shadow effect. A subset of the trajectories intersect the Earth and are physically impossible. This results in a region of rigidities some of which are allowed and some forbidden, usually referred to as penumbra. The penumbra can be studied by ways of numerical procedures of backtracking [50, 51]. The highest forbidden energy, so-called upper ridget cutoff, is 5-30% higher than R_c [52, 53].

R_C values in the zenith direction according to equation 6.1 are tabulated in table 6.1 for some geomagnetic latitudes. MAGIC will actually be built very close to the geomagnetic latitude of 30°N. Included in the table are the extreme cases of the magnetic pole (90° magnetic latitude), for which all trajectories are allowed, and the magnetic equator (0° magnetic latitude) for which the cutoff energy reaches a maximum. The values ranges for the cutoff tipically varies from

[1]For an electron, the rigidity cutoff in GV is equal to the energy cutoff in GeV.

Magnetic latitude	Rigidity cutoff (GV)
Magnetic pole 90°	0.
75°	0.1
60°	0.9
45°	3.7
30°	8.4
15°	12.9
Magnetic equator 0°	14.9

Table 6.1: *Electron rigidity cutoffs in the zenith direction for several magnetic latitudes calculated using Eq. 6.1. MAGIC will actually be built very close to* 30° *magnetic latitude.*

less than 1 GeV, for electron near the goemagnetic poles, to about 14 GeV for near equator. In addition, the flux of cosmic rays in the heliosphere varies due to the eleven years solar cycle, which causes a variation in the strength of the Solar Wind. All this causes that the electron spectrun doesn't really follow a power law.

6.3.2 Multipolar Field

As we have already said, the GF is not dipolar but multipolar. This produce that the rigidity cutoff depends not only on the latitude, and it is shown in Eq. 6.1, but also on the longitude since the geomagnetic multipolar field varies with it. Figure 6.2 shows the values of intensity of the Earth's GF on the North hemisphere, calculated starting from the IGRF2000 coefficients. We can see how for a given latitude the intensity varies with the geografic longitude.

For our work we will use the dipolar approximation of the geomagnetic field, since it is the only one which provide analytical expression for the rigidity cutoff.

6.4 Calculation of the Electron Dectection Rates Taking into Account the GF

Let us consider now the effect of the geomagnetic rigidity cutoff on the electron rates. For that, we only need to take into account that the GF is going to affect to the electron rates by means of preventing low energy electron from triggering the telescope. Then for calculating the rates we only have to consider electrons with energies above the cutoff. That is, we are going to calculate the electron rates in the same way that in §4.5.2, but now integrating only from energies above R_c up to 200 GeV. Firstly, we will calculate the rates when the telescope is making

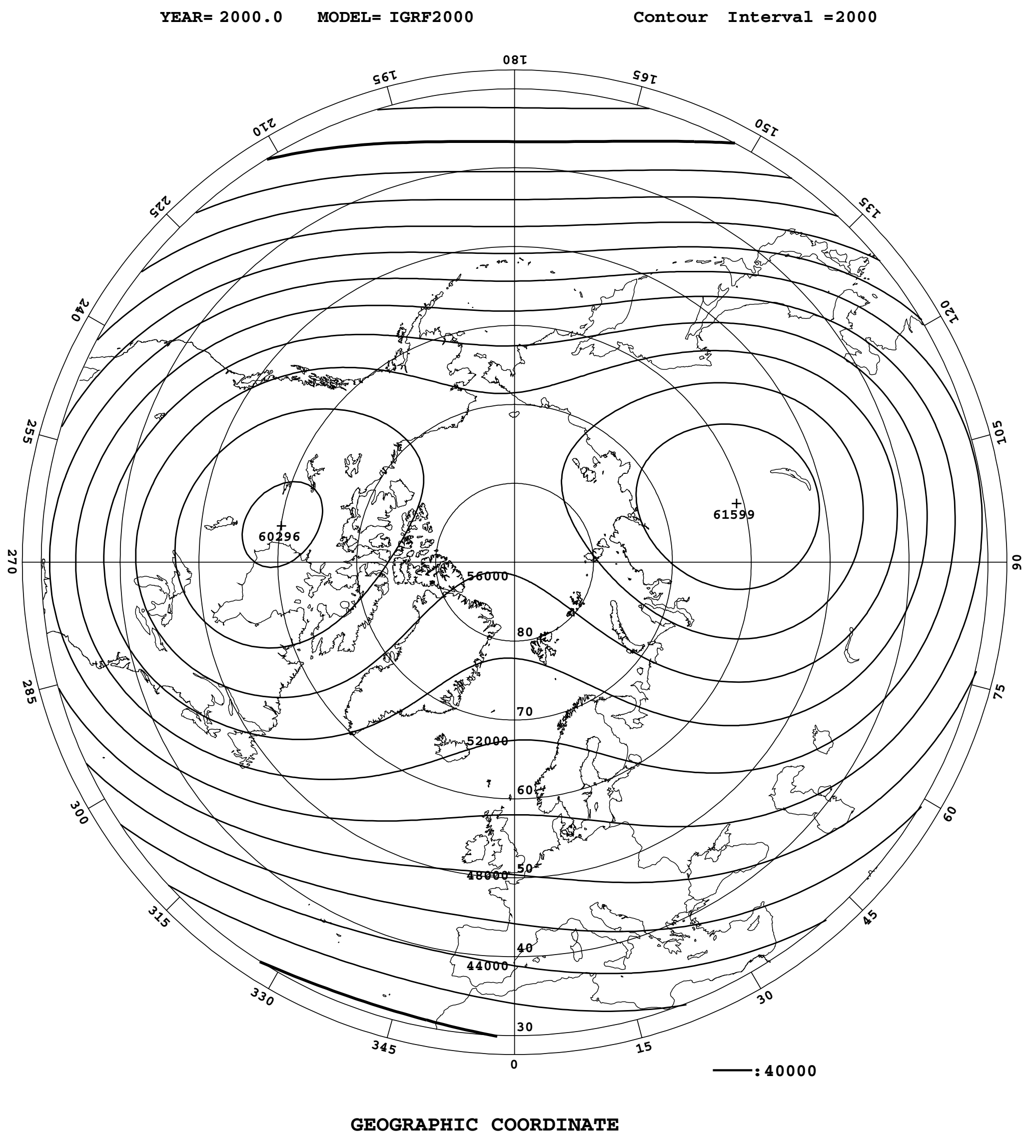

Figure 6.2: *Multipolar geomagnetic field based on the IGRF2000 coefficients. The figure shows the total geomagnetic intesisity (in nT) in contour intervals of 2000 nT.*

observation in the zenith direction. Then we will comment what would happen at other zenith angles.

6.4.1 Rates in the Zenith Direction

From Eq. 6.1 we obtain the value of the rigidity cutoff at the MAGIC location (latitude $\sim 29°$), and along with the MAGIC differential rate for electrons shown in fig. 4.12 we can re-calculate the electron detection rates, now taking into account the geomagnetic field.

Table 6.2 shows the electron rates at the MAGIC location taking into account the effect of the GF. Also shown is the fraction of this rate at the rate of 3.4 Hz that we obtained in §4.5.2 without consider the GF.

Location	Rigidity cutoff	Rate (Hz)	Reduction (%)
29°	8.0	3.2	6

Table 6.2: *Rigidity cutoff, electron raw rate expected for MAGIC and percent of reduction in the rate compared with the rate calculated without taking into account the GF.*

In the previous calculations we have assumed that there is an abrupt cut in the electron energy spectrum at the position of the rigidity cutoff, that is, we have ignored the penumbra. We may obtain an upper limit to the effect of the penumbra in the electron rate by assuming that all trajectories inside this energy region are forbidden and that the upper rigidity cutoff is always 25% higher than the rigidity cutoff. In this extreme case the rigidity cutoff at La Palma would be ~ 10 GeV, which yiels an electron rate of **3.1 Hz**. Thus. we obtain further reduction in the electron rate of at most **9%**.

6.4.2 Dependence on Zenith Angle

Above we have restricted our analysis to the zenith position of the telescope. Let us try to predict the geomagnetic cutoff effect at other zenith angles. The dependence of the electron rigidity cutoff on zenith angle for a number of azimuth angles at the MAGIC location, according to equation 6.1, is shown in Fig. 6.3.

For studying the dependence of the rates with the zenith angle we are going to consider two situations: zenith angles below 30° and zenith angles above 30°. This is because while a given IACT exhibits approximately the same collection area and energy threshold for all zenith angles below 30°, the energy threshold increases fast with zenith angle above 30°.

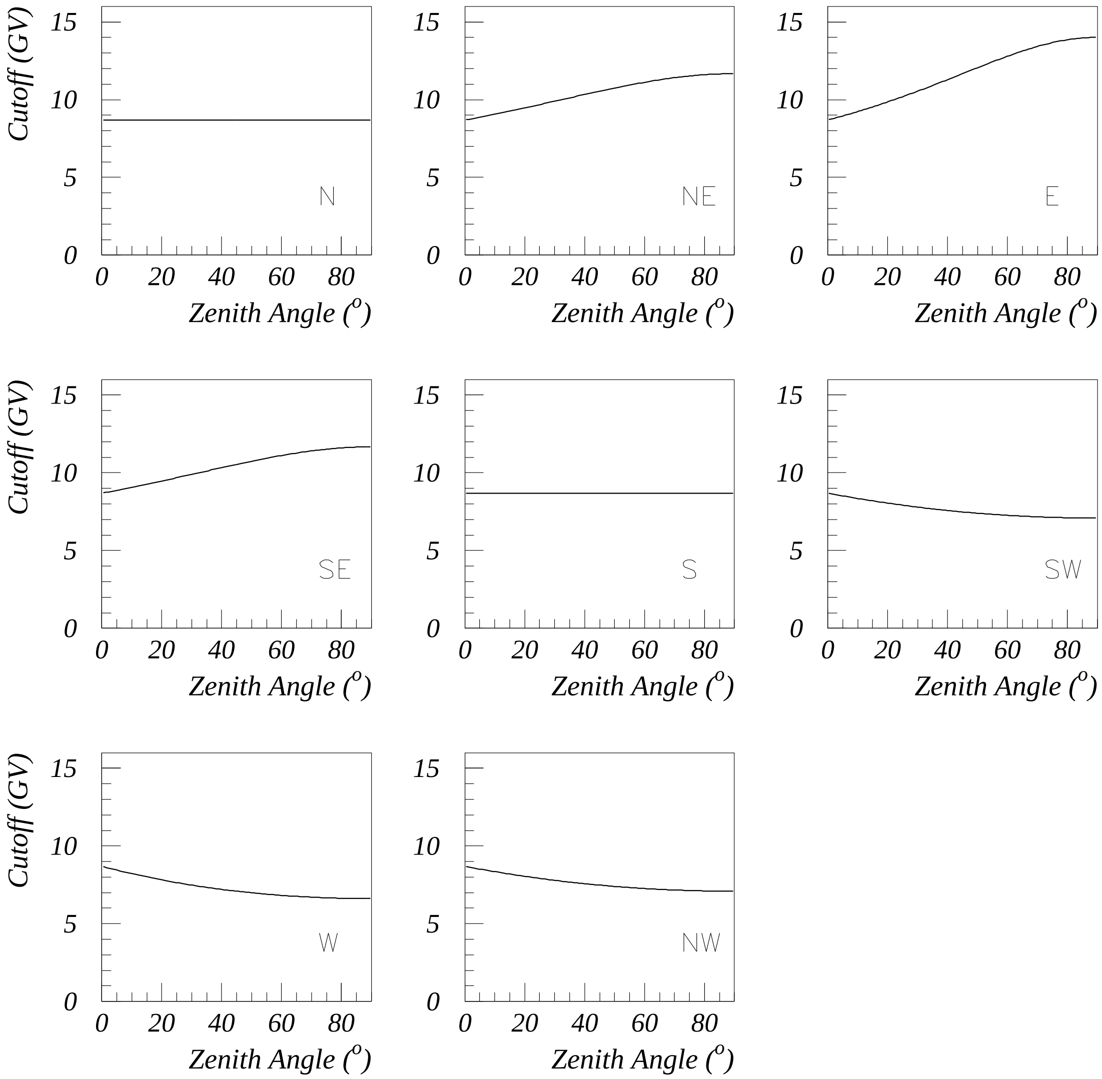

Figure 6.3: *Electron rigidity cutoff as a function of zenith angle for different azimuth angles, namely in north, nort-east, east, south-east, south, south-west, west and north-west directions.*

Zenith angle below 30°

As the collection area is approximately constant for all zenith angle below 30°, we can apply the zenith collection areas shown in Fig. 4.10 to all zenith angles below 30°. From Fig. 6.3 we see that the maximal reduction in electron rate will take place when the telescope point to the east. And the maximal enhancement will happen when the telescope points to the west. We have tabulated the rates expected for MAGIC in table 6.3 at zenith angles 0° and 30° in the west and east directions. The maximal rate reduction is **12%**. MAGIC sensitivity will thus improve sightly when pointing to the west and get slightly worse when pointing to the east. The effect of the zenith angle is expected to be greater in the case of MAGIC phase II.

Latitude	Zenith Angle	Azimuth	Rigidity Cutoff (GV)	Rate (Hz)
29°	0°	East/West	8.0	3.2
	30°	East	9.7	3.0
		West	6.9	3.1

Table 6.3: *Electron raw rates expected in the east and the west directions at zenith angles* 0° *and* 30° *for MAGIC.*

Zenith angle above 30°

In an IACT the energy threshold increases fast with zenith angle above 30° (see for example [54, 55]). At a zenith angle of 60° the energy threshold is already roughly one order of magnitude higher than the threshold close to the zenith. Because the cosmic electron spectrum falls with primary energy faster than that of the cosmic ray background or than those of most of the predicted γ-ray sources, we can expect the electron background to be less and less significant as we move to higher zenith angles. In adition the effect of the geomagnetic cutoff will decrease with zenith angle since R_c does not grow as fast as the telescopes threshold energy. Electrons triggering the telescope are thus never below R_c. Thus, the influence of the GF in this case is negligible for the electron trigger rate.

6.5 Influence of the Geografical Latitude on the Electron Detection Rates

As we see in equation 6.1 the geomagnetic cutoff depends on the geografical latitude. Therefore, the reduction in the electron rates also depends on the latitude. Thereby we ask ourselves what would be the electron detection rates for a telescope like MAGIC but placed in other location. It is clear that regarding with the GF, the optimal location would have been the magnetic equator, and the worse, the magnetic pole.

Let us going to calculate the expected electron rates at different locations, for observation at zenith and for different zenith angles.

6.5.1 Rates at Zenith

In table 6.4 we tabulate the electron rates pointing to zenith position that one would expect at different locations on Earth for MAGIC. Also shown is the fraction of the polar rate (rate at the magnetic pole). The polar rate is equal to the rate that we would obtain neglecting the rigidity cutoff. The effect of R_c is small for almost all the locations under consideration. Only at the magnetic equator do we observe a **25%** reduction in the rate.

Magnetic latitude	Rigidity Cutoff (GV)	Rate (Hz)	Fraction polar rate
Mag. pole 90°	0	3.4	1.00
75°	0.1	3.4	1.00
60°	0.9	3.4	1.00
45°	3.7	3.3	0.97
30°	7.3	3.2	0.94
15°	12.9	3.0	0.88
Magnetic equator	14.9	2.9	0.85

Table 6.4: *Electron raw rates and fraction of the polar rate as expected for MAGIC at different locations of the Earth's surface. The polar rate is equal to the rate that we would obtain in the absence of geomagnetic cutoff.*

6.5.2 Rates at Differents Zenith Angles

The dependence of the electron rigidity cutoff on zenith angle for a number of azimuth angles and geomagnetic latitudes according to equation 6.1 is given by Fig. 6.4.

Whereas the cutoff does not vary strongly with the zenith angle for geomagnetic latitudes above 30° (at most a 50% increase from 0 to 90° zenith angle in all azimuth directions), it rises by as much as a factor of 3 in the geomagnetic equator. The maximal reduction in the electron rate takes place in the magnetic equator when the telescope point to the east. The maximal enhancement happens also in the equator when the telescope points to the west. We have tabulated the rates expected for MAGIC in table 6.5 at geomagnetic latitudes 0° and 30° in the west and east directions. The maximal rate reduction is 30° while the maximal enhancement is 20%.

6.6 Validity of the Geomagnetic Model

Equation 6.1 is based on a dipole field. Hence we may consider to improve our calcultions by applying a more realistic main field such as the IGRF. Nevertheless because the dipole in equation 6.1 was approximated to the IGRF1980 value, we do not expect our results to differ considerably from the real values. It must be

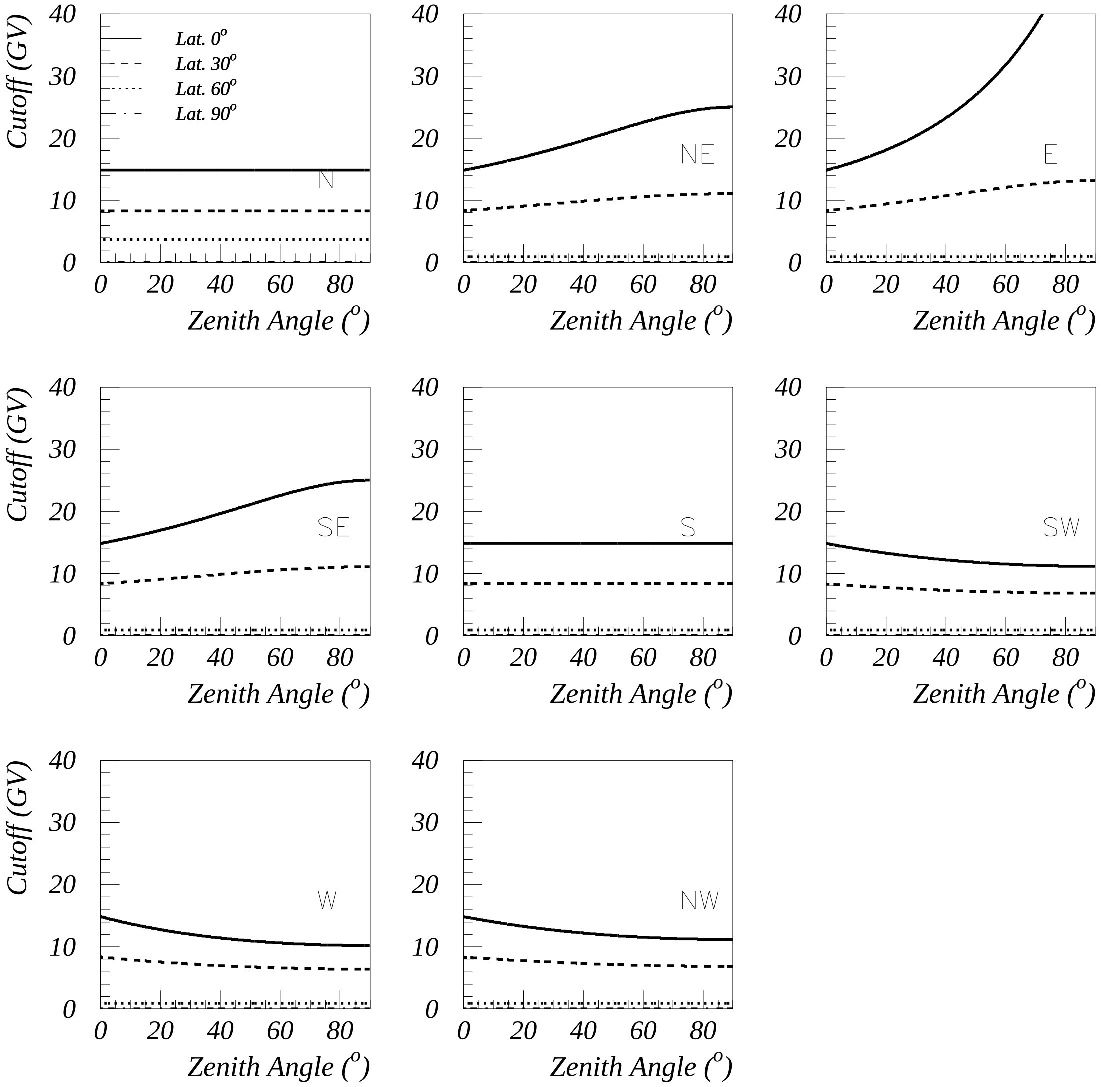

Figure 6.4: *Electron rigidity cutoff as a function of zenith angle for different azimuth angles, namely in north, nort-east, east, south-east, south, south-west, west and north-west directions. The four curves in each figure correspond to four magnetic latitudes:* 0° *(magnetic equator),* 30°, 60°, 90° *(magnetic pole).*

emphasized that no analytical solution for the rigidity cutoff is possible by using a field model more complex than a dipole field.

Effect of the Solar Wind

We have always neglected in our calculations the effect of the external geomagnetic field described in §6.1. Under normal conditions this field is asymetric due to the interaction of the Earth with the solar wind, which gives rise to a long tail extending to the direction almost opposite to that of the Sun (actually in

Latitude	Zenith Angle	Azimuth	Rigidity Cutoff (GV)	Rate (Hz)
0°	0°	East/West	14.9	2-9
	30°	East	18.3	2.8
		West	12.0	3.0
30°	0°	East/West	8.4	3.2
	30°	East	9.5	3.1
		West	7.2	3.2

Table 6.5: *Electron raw rates expected in the east and the west directions for locations at geomagnetic latitudes* 0° *and* 30° *for MAGIC.*

a direction perpendicular to the solar wind front, but for simplicity we assume that it extends in a direction opposite to the Sun). This introduces an asymetry in the electron arrival direction, since electrons going through the tail are more likely to be deflected than electron coming from the direction of the Sun. In other words, we expect the rigidty cutoff to grow in the direction opposite to the Sun. For a given arrival direction this is a daily effect. As consequence we expect the minimum electron rate to be reached at midnight in the zenith direction. Since IACTs operate only at night, the electron rate will on the whole be further reduced by this effect.

A detailed study would necessitate taking into account the fast variations of the external field produced during periods of increased solar activity. In general these periods profoundly complicate the calculations of rigidity cutoffs and background electron rates. Careful planning of IACT observations for special studies of extended source or the diffuse gamma background will be necessary during these periods.

Conclusions

We have performed detailed Monte Carlo simulations of γ-iniated atmospheric showers and also of background showers (simulating proton and electron events). Besides, we have taken into account the light of the night sky background. In our simulation the innovative features of the MAGIC Telescope were implemeted.

Our Monte Carlo simulations show that the MAGIC Telescope, with its large mirror reflecting area and high efficiency PMTs, has the capability to trigger on 10 GeV cosmic γ-rays. And with a collection area which increases rapidly with increasing energy, MAGIC should be able to overlap with EGRET in the 10 - 30 GeV range and capture pulsed γ-rays. In this energy region MAGIC will be constrained to the non-imaging mode. The fine pixelization and pulse height information should allow some rejection of background events based on size- and distance cuts. But still detailed simulations are required to determine the best rejection factor against background.

Regarding with the power of MAGIC for the observations of γ-ray pulsars, we find that for a final background rate of 50 Hz or less, pulsed detections should be possible within a few hours for Crab and PSR B1951+32. As Crab and PSR B1951+32 have spectra extending possibly to at least 30 GeV, and since they transit near La Palma, the pulsed emission from these sources should prove that MAGIC can trigger in the 10 - 30 GeV range and this will be useful for further calibration and understanding the operation at threshold. Although for Geminga it seems to be impossible the detection of any pulsed radiation given the fast cutoff of its pulsed spectrum, however, the Geminga skymap above 10 GeV could imply, by analogy with the skymaps of Crab and PSR B1951+32, a detection within one night.

The MAGIC Telescope is the only IACT telescope under construction which will have for first time the capability to detect the seven known EGRET pulsars and to test the pulsar models in detail. In addition, due to its very high sensitivity, the MAGIC Telescope will not only be an unique instrument for the study of the known γ-ray pulsars, but it will probably be able to discover several additional radio-pulsars at GeV energies. In this context, some hard-spectrum unidentified EGRET sources may also be pulsars, and if their spectra extend to the 10 - 30 GeV range, searches for pulsations would be possible with MAGIC.

The constraint for this capability is the detection within a single night, with confirmation runs the following few nights.

The effect of the Earth's geomagnetic field on the cosmic electron background was studied, with the aim of looking for a possible reduction in the MAGIC electron trigger rate.

The electron rate expected for MAGIC is approximately 3.4 Hz in the zenith direction, but taking into account the geomagnetic field this rate drops to 3.2 Hz, which means a reduction of a 6% in the cosmic electron rate. It is expected a larger reduction in the MAGIC phase II, when its camera is made out of 45% QE photodetectors. The reduction in the the detection rate depend on the zenith an azimuth angles. It decreases for some azimuth angles, reaching a minimum when the telescope points to the west, and increases for other angles peaking in the east direction. The electron background is expected to be very much reduced in high zenith angle observations.

We also have estimated the effect of the Earth's magnetic field at different geomagnetic latitudes, obtaining for instance that at the magnetic equator the MAGIC electron rate would drop to 2.9 Hz at zenith. The reduction with decreasing magnetic latitude reflects the fact that the electron rigidity cutoff is minimal at high geomagnetic latitudes and maximal at the equator.

The conclusion is that observations at low energies with the next generation of low thereshold IACTs will have to take into account the geomagnetic location of the IACT as well as the specific direction in which the instrument is pointing, especially for observations in which the zenith angles are less than 30°.

Appendix A

Image Parameters

The differences in the images left in the camera by γ- and hadron-induced showers are exploted by means of a suitable parametrization of the shower images. This parametrization is based on either a second moments approach or on some form of semi-analytical fitting of the shower images. The parameters that are usually used are the Hillas parameters [1], which are based on a second moments analysis of the recorded pixel signal amplitudes. These parameters can be classified into two groups: *shape parameters* which characterize the size of the image, and *orientation parameters*. In figure A.1 is skecth a shower image to ilustrate the geometrical meaning of these parameters.

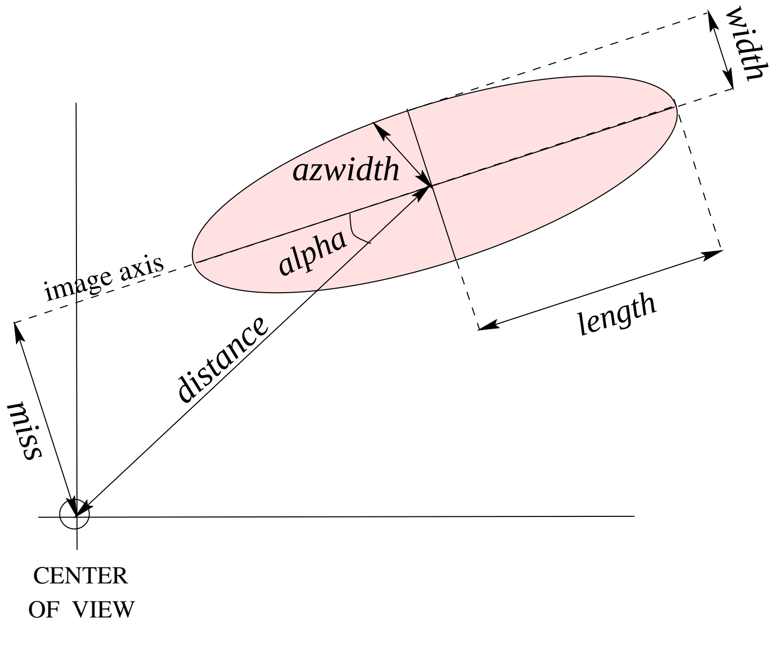

Figure A.1: *Image parameters.*

The parameters related with the orientation of the image are the following:

- *Alpha*: Is the angle between the major axis of the image and the radius drawn from the center of the camera to the center of the image. It is some how related to the angle between the shower axis and the axis of the telescope.

- *Distance*: The distance from the centroid of the image to the center of the field of view of the camera. It gives information of the impact parameter of the shower with respect to the CT. From another point of view if we take a line to join the shower maximum and the telescope is the angle between that line and the shower axis.

- *Miss*: The perpendicular distance between the major axis of the image and the center of the field of view of the camera. Its a measure of the shower orientation.

- *Azwidth*: The rms spread light perpendicular to the line connecting the centroid of the image to the center of the field of view. In other word is the projection of width along a line which is perpendicular to a line joining the center of the camera and the center of the image and which contains the centroid. This is a measure of both the shape and orientation of the image.

And the parameters related with the shape of the ellipse are:

- *Length*: Is the rms spread of light along the major axis of the image. Carries information of the longitudinal development of the shower.

- *Width*: The rms spread of light along the minor axis of the image. Carries with information of the lateral development of the shower.

- *Size*: The total integrated light content of the shower. Sometimes another parameter similar to size is used, and that is $conc_n$, that represents the degree of light concentration as determined from the ratio of the n largest pixel signals to the sum of all signals.

To calculate the image parameters for a given image we need the ADC counts in each pixel, together with the particular pixel coordinate. The image parameters are defined from the moments and from the image spreads. The *zero-order* moment define the size parameter, which is the sum of all the ADC signals in all the pixels which are non-zero after the cleaning of the image. It is calculated as:

$$Q = \sum q_i \tag{A.1}$$

where q_i represents the number of ADC signals or charge in the pixel i. The image centroid coordinates in the focal plane of the camera are given by te *first-order* moments:

$$\langle x \rangle = \frac{\sum q_i \cdot x_i}{Q} \qquad \langle y \rangle = \frac{\sum q_i \cdot y_i}{Q} \tag{A.2}$$

where x_i and y_i are the coordenates of the center of the pixel i. And the *second-order* moments describe the extent of the image:

$$\langle x^2 \rangle = \frac{\sum q_i \cdot x_i^2}{Q} \qquad \langle y^2 \rangle = \frac{\sum q_i \cdot y_i^2}{Q} \qquad \langle xy \rangle = \frac{\sum q_i \cdot x_i \cdot y_i}{Q} \tag{A.3}$$

Spreads of the images in different directions are then defined in terms of the moments as follows:

$$\sigma_{x^2} = \langle x^2 \rangle - \langle x \rangle^2, \qquad \sigma_{y^2} = \langle y^2 \rangle - \langle y \rangle^2, \qquad \sigma_{xy} = \langle xy \rangle - \langle x \rangle \langle y \rangle \tag{A.4}$$

Finally, the image parameters are calculated form the previously defined moments and the image spreads, as:

$$\text{length} = \sqrt{\frac{\sigma_{x^2} + \sigma_{y^2} + s}{2}} \tag{A.5}$$

$$\text{width} = \sqrt{\frac{\sigma_{x^2} + \sigma_{y^2} - s}{2}} \tag{A.6}$$

$$\text{distance} = \sqrt{\langle x \rangle^2 + \langle y \rangle^2} \tag{A.7}$$

$$\text{alpha} = \arcsin\left(\frac{miss}{distance}\right) \tag{A.8}$$

$$\text{miss} = \sqrt{\frac{u \cdot \langle x \rangle^2 + v \cdot \langle y \rangle^2}{2} - \frac{2\sigma_{xy} \langle x \rangle \langle y \rangle}{s}} \tag{A.9}$$

$$\text{azwidth} = \sqrt{\frac{\langle x \rangle^2 \langle y^2 \rangle - 2\langle x \rangle \langle y \rangle \langle xy \rangle + \langle x^2 \rangle \langle y \rangle^2}{\text{distance}^2}} \tag{A.10}$$

$$\text{conc}_\text{n} = \frac{\sum_i^n q_i}{Q} \tag{A.11}$$

where:

$$s = \sqrt{d^2 + 4(\sigma_{xy})^2}, \qquad d = \sigma_{y^2} - \sigma_{x^2}, \qquad u = 1 + d/s, \qquad v = 2 - u \tag{A.12}$$

Bibliography

[1] A.M. Hillas 1985, *Cherenkov Images of EAS Produced by Primary Gamma-Rays and by Nuclei*; Proc. 19^{th} ICRC (La Jolla) 3 445.

[2] D.J. Thompson et al., *ApJ S*, 107:277, 1996.

[3] P.A. Sturrock. *Ap. J.*, 164:529, 1971.

[4] M.A. Ruderman and P.G. Sutherland. *Ap. J.*, 196:51-72, 1975.

[5] K.S. Cheng and M.A. Ruderman. *Ap. J.*, 300:522, 1986.

[6] J. Chiang and R.W. Romani. *Ap. J.*, 400:629, 1992

[7] P. Goldreich and W.H. Julian. *Ap. J.*, 157:869, 1969.

[8] J.K. Daugherty and A.K. Harding *Ap. J.*, 458:278, 1996.

[9] R.K. Faul. *Astron. Astrophys.*, 317:99, 1997.

[10] M. Punch et al., Nature, 358:477, 1992.

[11] D. Petry et al., Astron. Astrophys., 311:L13-16, 1996.

[12] S.M. Bradbury et al., Astron. Astrophys., 320:L5-L8,1997.

[13] N. Magnussen, *Selected Results form Ground-Based Cosmic Ray and Gamma ray Experiments*, Proceedings M. Buball et al., Darmstadt, 1998.

[14] P.M. Chadwick et al., *Centaurus X-3, A source of High Energy Gamma Rays*. The Astroph. Journal 503 (1998), 391-395.

[15] W. Heitler 1944, *Quantum Theory of Radiation*, Oxford University Press, 2nd Edition.

[16] K. Greisen 1956, Prog. Cosmic Ray Phys. 3.

[17] R. Wiston, W.T. Weldford, *High Collection for Nonimaging Optics*, Academic Press, 1989.

[18] A. Ostankov, D. Paneque, E. Lorentz, M. Martinez and R. Mirzoyan, *A study of the new hemispherical 6-dynodes PMT from Electron Tubes*, preprint submitted to Elsevier Preprint, July 99.

[19] M. Martinez, A. Ostankov E. Lorentz, R. Mirzoyan and T. Schweizer, *Constraints in using APDs in Air Cherenkov Telescopes for Gamma-Astronomy*, preprint submitted to Elsevier Preprint, July 1999.

[20] D. Krainch et al. Astroparticle phys. 12 (1999) 65-74.

[21] K. Werner, *Phys. Rep.* 232 (1993) 87.

[22] N.N. Kalmykov, S.S. Ostapchenko, *Yad. Fiz. 56 (1993) 105; Phys. At. Nucle.* 56(3) (1993) 346; N.N. Kalmykov, S.S. Ostapchenko and A.I. Pavlov, *Bull. Russ. Aca. Sci. (Physics)* 58 (1994) 1966.

[23] J. Ranft, *Phys. Rev.* D51 (1995) 64.

[24] R.S. Fletcher, T.K. Gaisser, P. Lipari and T. Stanerv, *Phys. Rev.* D50 (1994) 5710.

[25] J. Engel, T.K. Gaisser, P. Lipari and T. Stanev, *Phys. Rev.* D46 (1992) 5013.

[26] J.N. Capdevielle, *J. Phys. G: Nucl. PArt. Phys.* 15 (1989) 909.

[27] H. Fesefeldt, Report PITHA-85/02 (1985), RWTH Achen.

[28] P.K.F. Grieder, Report INS-J125 (1970), Inst. for Nuclear Studies, Univ. of Tokyo; P.K.F. Grieder, *Proc.* 16^{th} *Int. Cosmic Ray Conf.*, Kyoto, 9 (1979) 161.

[29] W.R. Nelson et al. SLAC 265 (1985).

[30] K. Greisen, Prog. Cosmic Ray Physics Vol. III, J.G. Wilson ed. (North Holland Publishing Co., Amsterdam 1965) 1.

[31] F. Arqueros, S. Martinez and M. Rozanska, *Proc.* 23^{rd} *Int. Cosmic Ray Conf., Calgary*, 4 (1993) 738; S. Martinez et al., *Nucl. Instr. Meth.* A357 (1995) 567.

[32] R. Mirzoyan and E. Lorentz, 1994, *Measurement of the night sky background at La Palma*, Max-Planck-Institut für Physik report MPI-PhE/94- 35.

[33] B.Wiebe. *Chemical composition in high energy cosmic rays.* Wuppertal University preprint WUB 94-98, April 1994

[34] J. Cortina and J.C. Gonzalez. *The cosmic electron background in the low energy IACTs. Effect of the geomagnetic field.* Max-Planck-Institut für Physik report, 2000.

[35] Barrio J.A. et al., 1998, *The MAGIC proposal*, Max Planck Institut für Physik Munich report MPI-PhE/98-5.

[36] Thompson, D.J. 2001, *in Proc. International Symposium, Heidelberg 26-30 June 2000, Germany*, Eds. F.A. Aharonian, H.J. Völk American Institute of Physics 558, 103.

[37] J.M. Fierro, *Observation of Spin-Powered Pulsars with the EGRET Gamma Ray Telescope*, PhD. Thesis (Stanford University).

[38] de Jager, O.C., Konopelko, A., Raubenheimer B.C., & Visser, B. 2001, in Proc. *International Symposium, Heidelberg 26-30 June 2000, Germany*, Eds. F.A. Aharonian, H.J. Völk American Institute of Physics 558, 613.

[39] V. Fonseca, M. Lopez-Moya, O.C. de Jager, et al., *MAGIC as a detector for 10-30 GeV Pulsations from EGRET Pulsars*, International Cosmic Rays Conference, Heidelberg, Agust 2001.

[40] Nel, H.I. & de Jager, O.C. 1995, Astr. Space Science, 230, 299.

[41] R.C. Lamb & D.J. Macomb, 1997, ApJ. Suppl., 120, 355.

[42] O.C. de Jager, J.W.H. Swanepoel & B.C. Raubenheimer, 1989, *A Powerful Test for Weak Periodic Signals with Unknown Light Curve Shape in Sparse Data*, A&A, 170, 187.

[43] O.C. de Jager, *On Periodicity Tests and Flux Limit Calculation for Gamma-ray Pulsars*, 1994, ApJ, 436, 239.

[44] Stömer C., Astrophys. 1 (1930) 237.

[45] Wiebel-Sooth B., PhD Thesis, Wuppertal University (1998).

[46] Tsyganenko N. A., Planet. Space. Sci. 37 (1989) 5.

[47] Erikson G. M. et al., J. Geophys. Res. 96 (1991) 1663.

[48] Lambour R . L., PhD Thesis, Rice University (1994).

[49] Cooke D. J., Phys. Rev. Lett. 51 no. 4 (1983) 320.

[50] Shea M. A. and Smart D. F., J. Geophys. Res. 72 no. 7 (1967) 2021.

[51] Flückiger E. O. et al., Proc. 22nd ICRC Dublin 3 (1991) 648.

[52] Shea M. A. and Smart D. F., J. Geophys. Res. 70 no. 17 (1965) 4117.

[53] Lipari P. and Stanev T., Proc. 24th ICRC Rome 1 (1995) 516.

[54] Krennrich F. et al., Ap. J. 511 (1999) 149.

[55] Konopelko A. et al., 1999, Proc. Towards a Major Atmospheric Cherenkov Detector VI.

List of Figures

List of Tables